



**try on the latent.** The key is to distinguish between (i) the sampling dynamics in latent space and (ii) the many-to-one identification imposed by perception/semantics. Diffusion probability-flow maps are (almost everywhere) invertible under standard ODE conditions, hence cannot collapse dimension. But *semantics is not invertible*. We model the effective semantic outcome as a composition

$$\Phi = \pi \circ \Psi_{T \rightarrow 0} : \mathcal{Z} \cong \mathbb{R}^d \rightarrow \mathcal{M}, \quad (1)$$

where  $\Psi_{T \rightarrow 0}$  denotes the sampler (ODE/SDE solver) mapping and  $\pi$  is a differentiable proxy for semantic identification (e.g., CLIP/DINO features plus local chart projection, see Appendix B for  $\pi$ -sensitivity). On a dense regular set,  $\Phi$  behaves locally as a submersion:  $\text{rank}(D\Phi_z) = k \ll d$ . This implies a *fiber* structure:  $\mathcal{Z}$  foliates into level sets  $\Phi^{-1}(x)$  of dimension  $d - k$  representing semantic-invariant nuisance variation.

This immediately induces an *intrinsic* geometry on seeds. Pulling back the semantic metric  $g_{\mathcal{M}}$  yields a latent (semi-)metric

$$g_{\text{lat}} = \Phi^* g_{\mathcal{M}}, \quad (2)$$

which is necessarily *degenerate*: it assigns zero length to directions tangent to fibers and nonzero length only to a low-dimensional horizontal subspace. In other words, Euclidean proximity of seeds is not the right notion of proximity for semantic stability; the relevant local sensitivity is governed by the singular spectrum of  $D\Phi_z$  restricted to horizontal directions. This reframes the seed lottery as a geometric conditioning problem: seeds differ not merely by norm but by how they align with stiff horizontal directions versus redundant vertical directions.

**From geometry to an operational method without Jacobians.** The theory suggests a simple algorithmic principle: reduce idiosyncratic fiber information in the seed, and then bias the seed along prompt-aligned horizontal directions. However, explicitly computing  $D\Phi_z$  is intractable. We therefore leverage a crucial empirical fact consistent with the geometric picture: diffusion models expose tractable proxies of horizontal semantics through their own guided predictions (scores/velocities), especially when aggregated across timesteps. Early (low-SNR) stages largely commit global structure, while later stages refine details, implying that a time-aggregated direction can provide a robust semantic signal.

Concretely, we propose a training-free *Semantic Erasure and Horizontal Injection* procedure. (i) **Semantic erasure:** aggregate  $n$  i.i.d. Gaussian seeds into  $\bar{z}_T = \frac{1}{\sqrt{n}} \sum_i z^{(i)}$ , which preserves the  $\mathcal{N}(0, I)$  marginal while contracting idiosyncratic seed configurations (a variance/identifiability reduction on nuisance components). (ii) **Horizontal injection:** query the pretrained denoiser across a set of timesteps

using a time-consistent rescaling and aggregate prompt-conditioned predictions into a single direction  $v_{\text{agg}}$  that acts as a proxy for a horizontal semantic tangent. (iii) **Retraction:** inject along  $v_{\text{agg}}$  with strength  $\delta$  and retract onto the typical sphere to avoid distribution drift. This procedure targets the intrinsic anisotropy implied by  $g_{\text{lat}}$  while remaining compatible with pretrained samplers.

Our contributions are:

- **A unified geometric explanation of seed lottery.** We connect a series of seemingly disparate empirical observations about seed sensitivity to a single latent geometric object: a submersion-induced degenerate pullback (semi-)metric on seeds, clarifying why isotropic sampling is inefficient for semantic reliability.
- **A practical, training-free algorithm derived from the geometry.** We translate the horizontal/vertical splitting into an operational procedure that (a) preserves the Gaussian marginal via aggregation, (b) estimates a prompt-aligned horizontal direction via timestep-aggregated guidance, and (c) controls distribution shift via spherical retraction.
- **Consistent empirical gains and targeted ablations.** We validate improvements across multiple backbones and datasets using standard alignment/quality metrics, and ablate the role of temporal semantics and injection strength to match the geometric predictions.

## 2. Related Works

### 2.1. Seed Sensitivity and Initial-Condition Interventions

Beyond general alignment difficulty, diffusion models exhibit a persistent *Seed Lottery*: output quality and semantic faithfulness can vary dramatically with the random seed, motivating the practice of repeated sampling and cherry-picking (Qi et al., 2024; Podell et al., 2024b). This phenomenon has been linked to early denoising behavior and structure commitment, suggesting that the initial latent functions as a coarse scaffold rather than unstructured noise (Anjum, 2024; Blattmann et al., 2023). Motivated by this, multiple works directly optimize or refine the initial condition. Guo et al. propose attention-based refinement of initial noise (Guo et al., 2024); Zhou et al. formulate noise adjustment as a supervised learning problem using constructed datasets (Zhou et al., 2025). While effective, many such methods introduce architectural coupling, additional training, or costly per-model data construction. In contrast, we provide a *distribution-compatible* and *training-free* procedure: (i) semantic erasure via distribution-preserving noise aggregation and (ii) horizontal injection via timestep-aggregated, prompt-conditioned predictions, requiring no model retraining and no expensive per-prompt optimization.

## 2.2. Geometry of Latent Representations

Geometric perspectives emphasize that latent spaces of deep generative models are not operationally Euclidean: pullback metrics induced by decoders can be highly curved and anisotropic (Arvanitidis et al., 2018). Riemannian viewpoints have also been explored for diffusion/flow constructions on non-Euclidean domains (Lou et al., 2023; Chen & Lipman, 2024). At the representation level, manifold/fiber interpretations separate semantic factors from nuisance variation (Karras et al., 2019; Li, 2025), and recent analyses connect Jacobian spectra and dynamical phases to stability and anisotropy (Biroli et al., 2024; Ventura et al., 2025). Our work differs in the choice of the *geometric object*: we focus on the *semantic map*  $\Phi = \pi \circ \Psi$  (sampling dynamics composed with many-to-one semantic identification) and the induced pullback geometry. Under submersion regularity (O’Neill, 1966), this yields a *degenerate* pullback (semi-)metric with a natural horizontal/vertical decomposition, directly explaining seed anisotropy and motivating our training-free proxies for horizontal semantics.

## 3. Theory: Latent Space Degeneracy

### 3.1. Diffusion sampling as an invertible flow

We use a generic formulation that covers score/velocity/epsilon parameterizations. Let  $\{z_t\}_{t \in [0, T]}$  be the (latent) diffusion variable. The probability flow ODE (PF-ODE) is

$$\frac{dz_t}{dt} = v_\theta(z_t, t; y), \quad (3)$$

where  $y$  denotes conditioning (e.g., text prompt), and  $v_\theta$  is the learned drift/velocity field. Under standard regularity (locally Lipschitz in  $z$ ), the flow map

$$\Psi_{T \rightarrow 0} : \mathcal{Z} \rightarrow \mathcal{Z}, \quad z_0 = \Psi_{T \rightarrow 0}(z_T), \quad (4)$$

is a diffeomorphism on a dense set and preserves dimension. This is the source of the *diffeomorphism paradox*: PF-ODE alone cannot explain many-to-one semantic collapse.

### 3.2. Semantic identification as a differentiable projection

Let  $\mathcal{Z} \cong \mathbb{R}^d$  be the initialization space with isotropic prior  $Z_T \sim \mathcal{N}(0, I_d)$ . Let  $\mathcal{M}$  be a semantic manifold of intrinsic dimension  $k \ll d$  with metric  $g_{\mathcal{M}}$ . We model semantic identification using a differentiable proxy:

**Definition 3.1** (Differentiable semantic projection (operational model)). Let  $f : \mathcal{X} \rightarrow \mathbb{R}^D$  be a differentiable feature map (e.g., CLIP/DINO/Inception features), and let  $\text{Proj}_{\mathcal{M}}$  be a smooth local chart projection onto a  $k$ -dimensional semantic manifold (e.g., local PCA coordinates, learned atlas, or manifold autoencoder chart). Define

$$\pi(x) := \text{Proj}_{\mathcal{M}}(f(x)).$$

We then define the semantic map as the composition

$$\Phi := \pi \circ \Psi_{T \rightarrow 0} : \mathcal{Z} \rightarrow \mathcal{M}. \quad (5)$$

**Assumption 3.2** (Submersion regularity and negligible singular set).  $\Phi$  is  $C^2$  on a dense regular set  $\mathcal{Z}_{\text{reg}} := \{z : \text{rank}(D\Phi_z) = k\}$  and  $\mathbb{P}_{Z_T \sim \mathcal{N}(0, I)}(Z_T \notin \mathcal{Z}_{\text{reg}}) \approx 0$ .

### 3.3. Fibers and the horizontal–vertical decomposition

For a regular value  $x \in \mathcal{M}$ , the fiber  $\mathcal{F}_x := \Phi^{-1}(x)$  is a smooth submanifold of dimension  $d - k$ . At any  $z \in \mathcal{Z}_{\text{reg}}$ , define

$$\mathcal{V}_z := \text{Ker}(D\Phi_z), \quad \mathcal{H}_z := \mathcal{V}_z^\perp, \quad (6)$$

where  $\perp$  is with respect to the ambient Euclidean inner product on  $\mathbb{R}^d$ . Intuitively,  $\mathcal{V}_z$  captures semantically invariant (redundant) directions, and  $\mathcal{H}_z$  captures semantic degrees of freedom.

### 3.4. Pullback semi-metric and spectral conditioning

**Definition 3.3** (Pullback (semi-)metric). The pullback semi-metric induced by  $\Phi$  is

$$g_{\text{lat}}(z)(u, v) := \langle D\Phi_z(u), D\Phi_z(v) \rangle_{g_{\mathcal{M}}}. \quad (7)$$

In local coordinates on  $\mathcal{M}$  with metric matrix  $G_{\mathcal{M}}(\Phi(z))$  and Jacobian  $J_z \in \mathbb{R}^{k \times d}$ ,

$$G(z) = J_z^\top G_{\mathcal{M}}(\Phi(z)) J_z \in \mathbb{R}^{d \times d}. \quad (8)$$

**Theorem 3.4** (Degenerate geometry: vanishing directions on fibers). *Fix  $z \in \mathcal{Z}_{\text{reg}}$ . Then  $g_{\text{lat}}(z)$  vanishes on  $\mathcal{V}_z$  and is positive definite on  $\mathcal{H}_z$ :*

$$\|w\|_{g_{\text{lat}}} = 0 \quad \forall w \in \mathcal{V}_z, \quad \|u\|_{g_{\text{lat}}} > 0 \quad \forall u \in \mathcal{H}_z \setminus \{0\}.$$

*Equivalently,  $G(z)$  has rank  $k$  and  $\text{Ker}(G(z)) = \mathcal{V}_z$ .*

**Proof.** Appendix C.1.  $\square$

**Definition 3.5** (Effective horizontal condition number). Let  $\sigma_1(z) \geq \dots \geq \sigma_k(z) > 0$  be the nonzero singular values of  $D\Phi_z$  (in a local chart). Define the effective conditioning on  $\mathcal{H}_z$ :

$$\kappa_{\text{eff}}(z) := \frac{\sigma_1(z)^2}{\sigma_k(z)^2}. \quad (9)$$

**Lemma 3.6** (Local semantic sensitivity). *Let  $z \in \mathcal{Z}$  be a regular point of the semantic map  $\Phi : \mathcal{Z} \rightarrow \mathcal{M}$ , and let  $\mathcal{H}_z$  and  $\mathcal{V}_z$  denote the horizontal and vertical subspaces induced by the degenerate pullback metric. Assume  $\Phi$  is twice continuously differentiable in a neighborhood of  $z$  and its Jacobian  $J_z := D\Phi(z)$  is  $L$ -Lipschitz (equivalently,  $\|\nabla^2 \Phi\| \leq L$  locally).*

Then there exist constants  $c_1, c_2 > 0$ ,  $C > 0$ , and  $\delta > 0$  such that for any perturbation  $\Delta z$  with  $\|\Delta z\| \leq \delta$ ,

$$d_{\mathcal{M}}(\Phi(z + \Delta z), \Phi(z)) \leq c_2 \sigma_1(z) \|\text{Proj}_{\mathcal{H}_z} \Delta z\| + C \|\Delta z\|^2, \quad (10)$$

$$d_{\mathcal{M}}(\Phi(z + \Delta z), \Phi(z)) \geq c_1 \sigma_k(z) \|\text{Proj}_{\mathcal{H}_z} \Delta z\| - C \|\Delta z\|^2. \quad (11)$$

In particular, if  $\Delta z$  satisfies the (mild) cone condition  $\|\text{Proj}_{\mathcal{H}_z} \Delta z\| \geq \beta \|\Delta z\|$  for some  $\beta \in (0, 1]$ , then for sufficiently small  $\|\Delta z\|$  (e.g.,  $\|\Delta z\| \leq \beta \sigma_k(z)/(2L)$ ), the lower bound becomes linear:

$$d_{\mathcal{M}}(\Phi(z + \Delta z), \Phi(z)) \geq \frac{c_1}{2} \sigma_k(z) \|\text{Proj}_{\mathcal{H}_z} \Delta z\|. \quad (12)$$

**Proof.** Appendix C.2.  $\square$

### 3.5. Coarea transport and a geometric notion of “winning seeds”

To connect geometry with probability mass, define the  $k$ -Jacobian

$$J_k(\Phi, z) := \prod_{i=1}^k \sigma_i(z) = \sqrt{\det(J_z J_z^\top)}. \quad (13)$$

**Theorem 3.7** (Coarea density transport). *Assume  $\Phi$  is locally Lipschitz on  $\mathcal{Z}_{\text{reg}}$  and  $Z \sim p_Z$  has a density with respect to the Lebesgue measure on  $\mathcal{Z} \cong \mathbb{R}^d$ . Let  $X = \Phi(Z) \in \mathcal{M}$ . For regular values  $x \in \mathcal{M}$ ,*

$$p_{\mathcal{M}}(x) = \int_{\mathcal{F}_x} \frac{p_Z(z)}{J_k(\Phi, z)} d\mathcal{H}^{d-k}(z), \quad \mathcal{F}_x = \Phi^{-1}(x). \quad (14)$$

**Proof.** Appendix C.3.  $\square$

**Corollary 3.8** (A local “compression energy” surrogate). *Up to an additive constant, the local coarea weight satisfies*

$$-\log \left( \frac{p_Z(z)}{J_k(\Phi, z)} \right) = \underbrace{\frac{1}{2} \|z\|^2}_{\text{prior energy}} + \underbrace{\log J_k(\Phi, z)}_{\text{expansion / volume term}} + \text{const.}$$

Thus a convenient local diagnostic is

$$E_{\text{eff}}(z) := \frac{1}{2} \|z\|^2 + \frac{1}{2} \log \text{pdet}(J_z J_z^\top), \quad (15)$$

where  $\text{pdet}$  is the product of nonzero eigenvalues (pseudo-determinant).

**Proof.** Appendix C.4.  $\square$

**Interpretation.** The seed lottery corresponds to large variability of  $(\sigma_1, \sigma_k, J_k, \kappa_{\text{eff}})$  across  $\mathcal{Z}_{\text{reg}}$ : some seeds sit in well-conditioned regions that reliably move along  $\mathcal{H}$  under conditioning, while many seeds waste mass along near-vertical directions or fall near poorly conditioned regions.

**Remark 3.9** (Why we avoid explicit Jacobians). All quantities above depend on  $D\Phi$ , but  $\Phi$  is conceptual (it includes  $\pi$ ). Our methods in Section 4 use tractable *horizontal proxies* derived from the model’s own predictions, requiring only standard forward passes and no Jacobian materialization.

We provide geometric interpretation of the fiber bundle structure and its interaction with initialization in Appendix A.

## 4. Method: Horizontal Seed Shaping

As summarized in Figure 2, our method shapes only the *initial seed* via three stages: (i) distribution-preserving semantic erasure by noise aggregation (NLN), (ii) timestep-based Temporal Prediction Weighting (TPW) to estimate a prompt-aligned *horizontal* direction, and (iii) horizontal injection followed by spherical retraction to remain on the prior typical set.

### 4.1. Setup and design goal

Given a pre-trained diffusion backbone and a prompt  $y$ , standard sampling draws  $z_T \sim \mathcal{N}(0, I_d)$  and runs a sampler. Our goal is to modify only the initialization while staying close to the prior typical set (i.e.,  $\|z\| \approx \sqrt{d}$ ), so that sampling is biased toward directions that meaningfully change semantics (horizontal directions).

**Guiding principle.** By Theorems 3.4 and 3.6, vertical directions are semantically silent (fiber directions) while horizontal directions control first-order semantic change. Hence an effective seed-shaping method should: (i) reduce idiosyncratic vertical configurations (semantic erasure), (ii) inject prompt-relevant horizontal components in a stable manner (horizontal injection), (iii) keep  $\|z\|$  near  $\sqrt{d}$  to avoid distribution shift.

### 4.2. Stage I: Noise Latent Normalization (NLN)

Stage I targets the *seed-specific* instability induced by latent-space degeneracy (Theorems 3.4, 3.5 and 3.7). The key is to keep the initialization *prior-valid* while extracting a *replica-averaged* notion of “typical semantics” induced by the generator geometry. This resolves the common confusion between (i) preserving the *overall* latent distribution and (ii) averaging semantics *across samples*.

**Replica sampling and NLN.** We draw  $n$  i.i.d. seeds and form a single prior-matched macro-seed  $z_T^{(1)}, \dots, z_T^{(n)} \stackrel{\text{i.i.d.}}{\sim} \mathcal{N}(0, I_d)$ :

$$\bar{z}_T := \mathcal{P}_n(z_T^{(1:n)}) := \frac{1}{\sqrt{n}} \sum_{i=1}^n z_T^{(i)}. \quad (16)$$

**Proposition 4.1** (Distributional validity). *The NLN output*

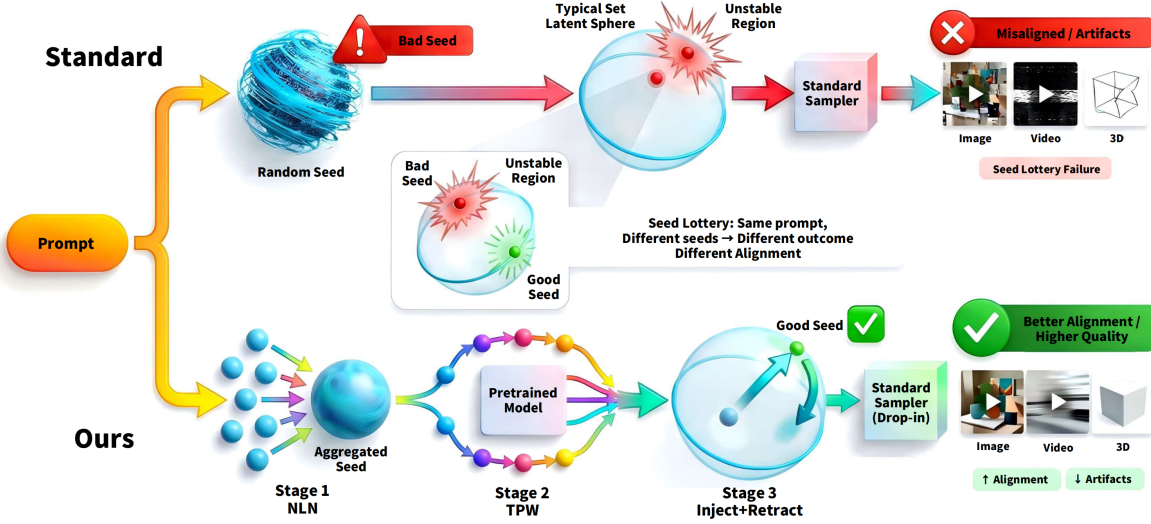


Figure 2. Overview of Horizontal Seed Shaping

preserves the initialization law:

$$\bar{z}_T \sim \mathcal{N}(0, I_d). \quad (17)$$

**Proof.** Appendix C.5.  $\square$

**Degeneracy-induced semantic averaging (what “averaging” actually means).** Let  $X = \Phi(Z_T) \in \mathcal{M}$  with  $Z_T \sim \mathcal{N}(0, I_d)$ , so the semantic law is  $\nu := \Phi_{\#} p_Z$  and admits the coarea density Theorem 3.7. Semantic “averaging” in NLN refers to *averaging over i.i.d. semantic outcomes*  $\{X^{(i)} = \Phi(z_T^{(i)})\}_{i=1}^n$ , not to changing the marginal law of a single draw. Because  $\Phi$  is many-to-one,  $\nu$  is shaped by the fiber geometry via  $J_k(\Phi, z)$  (Theorem 3.7), so the resulting semantic average is *generator-geometry-induced*.

**Lemma 4.2** (Semantic averaging induced by latent degeneracy geometry). *Let  $X = \Phi(Z_T)$  with  $Z_T \sim \mathcal{N}(0, I_d)$  and  $\nu = \Phi_{\#} p_Z$ . Assume the Fréchet functional*

$$\mathcal{F}(x) := \mathbb{E} \left[ d_{\mathcal{M}}(x, X)^2 \right], \quad x \in \mathcal{M}, \quad (18)$$

*has a unique minimizer  $x^* \in \mathcal{M}$  (the population Fréchet/Karcher mean), and is locally strongly geodesically convex in a neighborhood of  $x^*$ . Then:*

1. **(Geometry-induced mean via coarea)**  $\mathcal{F}$  admits the coarea representation

$$\begin{aligned} \mathcal{F}(x) &= \int_{\mathcal{M}} d_{\mathcal{M}}(x, u)^2 p_{\mathcal{M}}(u) d\mathcal{H}^k(u) = \\ &= \int_{\mathcal{M}} d_{\mathcal{M}}(x, u)^2 \left( \int_{\mathcal{F}_u} \frac{p_Z(z)}{J_k(\Phi, z)} d\mathcal{H}^{d-k}(z) \right) d\mathcal{H}^k(u), \end{aligned} \quad (19)$$

*hence  $x^*$  is determined by the degeneracy geometry through  $J_k(\Phi, z)$  and fiber measures.*

2. **(Replica semantic averaging)** Let  $X^{(i)} = \Phi(z_T^{(i)})$  be i.i.d. samples from  $\nu$  and

$$\hat{x}_n \in \arg \min_{x \in \mathcal{M}} \frac{1}{n} \sum_{i=1}^n d_{\mathcal{M}}(x, X^{(i)})^2 \quad (20)$$

*be the empirical Fréchet mean (assumed unique). Then  $d_{\mathcal{M}}(\hat{x}_n, x^*) = O_{\mathbb{P}}(n^{-1/2})$ .*

**Proof.** Appendix C.6.  $\square$

**How NLN is used in our pipeline.** Lemma 4.2 clarifies the only valid meaning of “semantic averaging”: it is an *estimator over multiple i.i.d. samples* under the generator-induced semantic law, with weights determined by the degeneracy geometry via Theorem 3.7. In our method, we do *not* invert  $\Phi$  to realize  $\hat{x}_n$  in latent space. Instead, Stage I produces a *prior-valid* macro-seed  $\bar{z}_T$  (Prop. 4.1) and a replica pool  $\{z_T^{(i)}\}$ . Stage II then probes locally around  $\bar{z}_T$  to estimate a robust, prompt-aligned horizontal direction, where variance reduction becomes effective.

**Remark 4.3** (No contradiction: distribution preservation vs. semantic averaging). Prop. 4.1 ensures  $\bar{z}_T$  is a valid prior draw, so Stage I alone cannot bias  $\nu = \Phi_{\#} p_Z$ . Lemma 4.2 does not claim otherwise: it concerns averaging *across* semantic replicas and shows how the generator-induced geometry (via  $J_k$  and fibers) sets the population semantic mean. Hence Stage II is essential: gains must come from model-dependent horizontal injection, not from altering the prior.

### 4.3. Stage II: Time-consistent probing and Temporal Prediction Weighting (TPW)

We construct a robust horizontal direction by aggregating the model’s *guided* predictions across timesteps. Let

$\epsilon_\theta(\cdot, t, y)$  denote the backbone prediction used by the sampler (noise/score/velocity depending on parameterization), and let  $\emptyset$  denote the unconditional prompt. When classifier-free guidance (CFG) is available, we use the *CFG residual* as a prompt-aligned direction:

$$g_\theta(z_t, t, y) := \epsilon_\theta(z_t, t, y) - \epsilon_\theta(z_t, t, \emptyset). \quad (21)$$

(For flow-matching backbones, replace  $\epsilon_\theta$  by the predicted velocity  $v_\theta$  and define  $g_\theta$  analogously.)

**Time-consistent probing inputs.** To probe  $\epsilon_\theta(\cdot, t, \cdot)$  at multiple times without running a full trajectory, we map a single aggregate seed  $\bar{z}_T$  to each probing time by a scheduler-consistent scaling:

$$\bar{z}_{t_k} := \rho(t_k) \bar{z}_T. \quad (22)$$

Here  $\rho(t)$  is chosen to match the backbone’s native scheduler so that  $\bar{z}_t$  lies on (or near) the typical set of the sampler input at time  $t$ . Concretely, for  $\sigma$ -parameterized diffusion schedulers we set  $\rho(t) = \sigma(t)$  (or  $\sigma(t)/\sigma(T)$  depending on convention for  $z_T$ ), while for backbones whose state is already expressed in the units of  $z_T$ , we use  $\rho(t) \equiv 1$  unless the scheduler specifies an additional scale.

**Weights.** Given probing times  $\{t_k\}_{k=1}^K$  and a nonnegative weighting function  $\omega(\cdot)$ , we define

$$w_k := \frac{\omega(t_k)}{\sum_{j=1}^K \omega(t_j)}, \quad \omega(t) \geq 0. \quad (23)$$

**Aggregated direction.** We define the weighted aggregate with a scale normalization that makes different  $K$  and weight spreads comparable:

$$v_{\text{agg}} := \frac{\sum_{k=1}^K w_k g_\theta(\bar{z}_{t_k}, t_k, y)}{\sqrt{\sum_{k=1}^K w_k^2}}. \quad (24)$$

**Lemma 4.4** (Horizontal proxy score). *Assume locally that the model predictions are (approximately) horizontal in the sense that  $\epsilon_\theta(z_t, t, y) = J_{z_t}^\top v_t(y)$  and  $\epsilon_\theta(z_t, t, \emptyset) = J_{z_t}^\top v_t(\emptyset)$  for some vectors  $v_t(\cdot)$ . Then the CFG residual  $g_\theta(z_t, t, y)$  in (21) lies in the horizontal complement:*

$$g_\theta(z_t, t, y) \in (\ker J_{z_t})^\perp \approx \mathcal{H}_{z_t}.$$

**Rationale.** When the semantic map is a submersion, first-order semantic changes occur along horizontal directions, while vertical (fiber) directions are locally semantic-invariant; hence prompt-dependent conditional gradients are expected to be orthogonal to fibers.

**Proposition 4.5** (Temporal aggregation improves directional concentration). *Assume probing predictions admit*

*a decomposition  $v_k = \mu_k + \xi_k$  with  $\mathbb{E}[\xi_k] = 0$  and  $\text{Cov}(\xi_k) = \Sigma$ , and  $\{\xi_k\}_{k=1}^K$  are independent across  $k$ . Let  $v_{\text{agg}}$  be defined by (24). Then  $\text{Cov}(v_{\text{agg}}) = \Sigma$ , i.e., the normalization stabilizes the covariance scale. Moreover, if the mean directions are aligned (e.g.,  $\mu_k \approx \mu$ ), then the mean magnitude scales with the effective sample size  $N_{\text{eff}} := \frac{(\sum_k w_k)^2}{\sum_k w_k^2}$ :*

$$\|\mathbb{E}[v_{\text{agg}}]\|^2 = N_{\text{eff}} \|\mu\|^2,$$

*so directional concentration around  $\mu$  strengthens as  $N_{\text{eff}}$  increases.*

**Proof.** Appendix C.8. □

**Choosing timesteps and weights.** In practice, we choose  $\{t_k\}$  to cover distinct semantic regimes (e.g., spanning low-SNR to high-SNR regions). Weights  $w_k$  can be uniform, log-SNR spaced, or shaped by a unimodal “phase-priority” function.

#### 4.4. Stage III: Horizontal injection with spherical retraction

**Orthogonalized injection.** Let  $\hat{z} := \bar{z}_T / \|\bar{z}_T\|$  and  $\hat{v} := v_{\text{agg}} / \|v_{\text{agg}}\|$ . To avoid injecting along the radial direction, we remove the component of  $\hat{v}$  parallel to  $\hat{z}$ :

$$\tilde{v}_\perp := \hat{v} - (\hat{v}^\top \hat{z}) \hat{z}, \quad \hat{v}_\perp := \frac{\tilde{v}_\perp}{\|\tilde{v}_\perp\|}. \quad (25)$$

(If  $\|\tilde{v}_\perp\|$  is numerically tiny, we skip orthogonalization or add a small  $\varepsilon$  in the denominator.)

**Spherical retraction.** We inject along  $\hat{v}_\perp$  and retract back to the typical sphere:

$$z^* := \|\bar{z}_T\| \cdot \frac{\bar{z}_T + \delta \hat{v}_\perp}{\|\bar{z}_T + \delta \hat{v}_\perp\|}, \quad (26)$$

where  $\delta > 0$  controls injection strength.

**Proposition 4.6** (Retraction is the Euclidean projection onto the radius constraint).  *$z^*$  is the solution to*

$$\min_{z: \|z\| = \|\bar{z}_T\|} \|z - (\bar{z}_T + \delta \hat{v}_\perp)\|^2,$$

*i.e., the Euclidean projection of the injected point onto the sphere of radius  $\|\bar{z}_T\|$ .*

**Proof.** Appendix C.9. □

**Lemma 4.7** (Small- $\delta$  regime: controlled perturbation without radial shift). *Let  $R = \|\bar{z}_T\|$ . For  $\delta \ll R$ ,*

$$\|z^* - \bar{z}_T\| = O(\delta), \quad \|z^*\| = \|\bar{z}_T\| \text{ (exact)}.$$

*Thus injection changes direction while preserving the typical radius exactly.*

**Proof.** Appendix C.10. □

**Why retraction matters.** Large  $\delta$  without retraction pushes  $z$  off the typical set and can trigger out-of-distribution behavior. Retraction keeps the seed on the same radius shell, making the intervention sampler-compatible.

## 5. Experiment and Analysis

### 5.1. Visualization of Latent Degeneracy

Our theory predicts a *degenerate* semantic pullback geometry: most latent directions are locally semantic-invariant, while semantic change concentrates in a low-dimensional horizontal subspace (Theorem 3.4, Lemma 3.6). We visualize these signatures with *typical-set*, *radius-preserving* probes; details and more figures are in Appendix E.

**Typical-radius shell probing.** For a prompt  $y$  and a baseline seed  $z_T$ , let  $R = \|z_T\|$  and  $\hat{z} = z_T/R$ . We perturb  $z_T$  along great-circle geodesics on the sphere  $\{z : \|z\| = R\}$ : sample a random direction  $u \sim \mathcal{N}(0, I)$ , project to the tangent space  $\hat{u} = \frac{u - \langle u, \hat{z} \rangle \hat{z}}{\|u - \langle u, \hat{z} \rangle \hat{z}\|}$ , and define

$$z_T(\theta) = R(\cos \theta \hat{z} + \sin \theta \hat{u}), \quad \|z_T(\theta)\| = R. \quad (27)$$

This isolates *directional* semantic sensitivity without distribution shift from radius drift (cf. our inject+retract operator in Sec. 4.4).

**Semantic displacement and alignment observables.** Let  $\phi(z_T)$  be a semantic representation of the generated output (we use normalized CLIP image embeddings in practice). For each  $\theta$ , we measure (i) semantic displacement

$$\|\Delta\phi\|(\theta) = \|\phi(z_T(\theta)) - \phi(z_T)\|_2, \quad (28)$$

and (ii) prompt alignment (e.g., CLIPsim between image and text embeddings); see Appendix E.1.

**Signature I: heavy-tailed directional sensitivity (anisotropy).** Fix a small probing angle  $\theta_0$  and measure  $\|\Delta\phi\|(\theta_0)$  over random tangent directions. Most directions yield near-zero change, but a small fraction produces large semantic shifts (Appendix Fig. 13), consistent with a rank- $k$  pullback semi-metric.

**Signature II: effective low-rank local spectrum.** We estimate directional derivatives via symmetric finite differences  $g_j = \frac{\phi(z_T(+\theta_0; \hat{u}_j)) - \phi(z_T(-\theta_0; \hat{u}_j))}{2\theta_0}$  and compute the Gram spectrum. The eigenvalues show a clear head/gap (Appendix Fig. 14), indicating sensitivity concentrated in few directions.

**Signature III: horizontal-proxy directions move semantics faster than controls.** Comparing geodesics along a prompt-conditioned horizontal proxy (Sec. 4.3) vs a random control, the proxy yields a larger initial slope of  $\|\Delta\phi\|(\theta)$  and often better alignment at moderate  $\theta$  (Appendix Fig. 15); too large  $\theta$  can overshoot, motivating controlled injection with spherical retraction (Sec. 4.4).

### 5.2. Method Results

Experiment settings are in Appendix G

Tables 3, 1, and 2 report quantitative results. **All intervals are 95% confidence intervals.** Across *all* evaluated backbones, our approach improves alignment-oriented metrics (e.g., CLIPScore/VQAScore) while maintaining competitive perceptual quality metrics.

The multi-modal consistency supports our geometric viewpoint: the seed lottery is not an artifact of a particular architecture, but a consequence of an intrinsic horizontal-vertical anisotropy in semantic sensitivity. Qualitative results are in Appendix L.

We also conducted a paired human-preference study across modalities. As summarized in Table 11, our method achieves preference rates over Standard. Details are in Appendix I.

Table 1. Experiments on WAN over VBench datasets. (AQ = Aesthetic Quality, AS = Appearance Style, BC = Background Consistency, DD = Dynamic Degree, IQ = Imaging Quality, MS = Motion Smoothness, OC = Overall Consistency, SC = Subject Consistency, TF = Temporal Flickering, VQA = VQAScore).

Method	AQ(↑)	AS(↑)	BC(↑)	DD(↑)	IQ(↑)	MS(↑)	OC(↑)	SC(↑)	TF(↑)	VQA(↑)
Standard	0.572	0.220	0.963	0.644	0.644	0.972	0.244	0.937	0.984	0.534
	[0.556, 0.588]	[0.206, 0.234]	[0.959, 0.967]	[0.632, 0.656]	[0.634, 0.654]	[0.969, 0.975]	[0.240, 0.255]	[0.931, 0.943]	[0.981, 0.987]	[0.520, 0.548]
Ours	0.651	0.341	0.985	0.701	0.664	0.997	0.303	0.994	0.997	0.600
	[0.636, 0.666]	[0.325, 0.357]	[0.982, 0.988]	[0.690, 0.712]	[0.655, 0.673]	[0.992, 0.998]	[0.291, 0.315]	[0.992, 0.996]	[0.990, 0.999]	[0.586, 0.614]

Table 2. Experiments on TRELIS over Toy4k datasets. (FD\* = Fréchet Inception/DINOv2 Distance, KD\* = Kernel Inception/DINOv2 Distance, VQA = VQAScore).

Method	FD <sub>incep</sub> (↓)	KD <sub>incep</sub> (↓)	FD <sub>DINOv2</sub> (↓)	KD <sub>DINOv2</sub> (↓)	VQA(↑)
Standard	29.5443	0.0106	340.5303	0.8023	0.8757
	[29.51, 29.78]	[0.0101, 0.0111]	[336.9, 344.2]	[0.789, 0.816]	[0.863, 0.889]
Ours	29.4028	0.0076	335.4251	0.7328	0.9114
	[29.34, 29.46]	[0.0072, 0.0080]	[332.0, 337.9]	[0.720, 0.746]	[0.899, 0.924]

### 5.3. Ablation I: Effect of Semantic Erasure (NLN)

NLN aggregates  $n$  i.i.d. Gaussian seeds while preserving the  $\mathcal{N}(0, I)$  marginal. Empirically, increasing  $n$  improves alignment up to a saturation point (Figure 3). This behavior matches the intended role of NLN: it reduces *seed-specific* idiosyncrasy, thereby stabilizing downstream prompt-aligned shaping, but cannot by itself guarantee that the seed lands near the target prompt semantics. Once the “vertical noise” is sufficiently suppressed, further

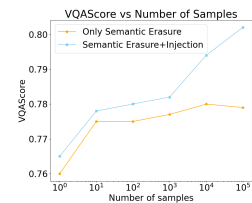


Figure 3. Impact of sample size in semantic erasure and injection.

Table 3. Experiments on SDXL and FLUX over various datasets. (Pick = PickScore, ImgR = ImageReward, CLIP = CLIPScore).  
<sup>†</sup>Only available for SDXL.

Model	Dataset	Method	Pick (†)	AES (†)	ImgR (†)	CLIP(%) (†)
SDXL	Pick-a-Pic	Standard	17.0490	5.5865	-1.9705	16.2233
		Initno <sup>†</sup> (Guo et al., 2024)	[16.9890, 17.1090]	[5.5615, 5.6115]	[-2.0005, -1.9405]	[16.1533, 16.2933]
		NPNet (Zhou et al., 2025)	17.0498	5.6032	-1.9692	16.2365
		Ours	17.0508	5.6200	-1.9680	16.2500
		Ours	[16.9808, 17.1108]	[5.5782, 5.6282]	[-1.9992, -1.9392]	[16.1665, 16.3065]
		Ours	17.1927	5.7052	-1.8928	16.4257
	DrawBench	Standard	17.4159	5.2427	-2.0842	16.6177
		Initno <sup>†</sup> (Guo et al., 2024)	[17.3459, 17.4859]	[5.2177, 5.2677]	[-2.1142, -2.0542]	[16.5477, 16.6877]
		NPNet (Zhou et al., 2025)	17.4188	5.2460	-2.0848	16.6320
		Ours	17.3488, 17.4888]	[5.2210, 5.2710]	[-2.1148, -2.0548]	[16.5620, 16.7020]
		Ours	17.4200	5.2485	-2.0841	16.6400
		Ours	[17.3500, 17.4900]	[5.2235, 5.2735]	[-2.1141, -2.0541]	[16.5700, 16.7100]
HPD	Standard	16.7476	5.5804	-1.9545	14.9859	
	Initno <sup>†</sup> (Guo et al., 2024)	[16.6676, 16.8276]	[5.5554, 5.6054]	[-1.9845, -1.9245]	[14.9056, 15.0659]	
	NPNet (Zhou et al., 2025)	16.7650	5.5900	-1.9520	15.0100	
	Ours	16.6850, 16.8450]	[5.5650, 5.6150]	[-1.9820, -1.9220]	[14.9300, 15.0900]	
	Ours	16.7800	5.6000	-1.9480	15.0400	
	Ours	[16.7000, 16.8600]	[5.5750, 5.6250]	[-1.9780, -1.9180]	[14.9600, 15.1200]	
Pick-a-Pic	Standard	17.1336	6.0469	-1.9415	16.2951	
	Initno <sup>†</sup> (Guo et al., 2024)	[17.0536, 17.2136]	[6.0219, 6.0719]	[-1.9715, -1.9115]	[16.2251, 16.3651]	
	NPNet (Zhou et al., 2025)	17.1400	6.0580	-1.9360	16.3050	
	Ours	17.0600, 17.2200]	[6.0330, 6.0830]	[-1.9660, -1.9060]	[16.2350, 16.3750]	
	Ours	17.5612	6.2013	-1.9201	16.3413	
	Ours	[17.5012, 17.6212]	[6.1763, 6.2263]	[-1.9501, -1.8901]	[16.2713, 16.4113]	
FLUX.1-Dev	Standard	17.2748	5.6527	-2.0509	16.6422	
	Initno <sup>†</sup> (Guo et al., 2024)	[17.1948, 17.3548]	[5.6277, 5.6777]	[-2.0809, -2.0209]	[16.5722, 16.7122]	
	NPNet (Zhou et al., 2025)	17.2820	5.6680	-2.0440	16.6550	
	Ours	17.2020, 17.3620]	[5.6430, 5.6930]	[-2.0740, -2.0140]	[16.5850, 16.7250]	
	Ours	17.3804	5.7115	-2.0091	16.6974	
	Ours	[17.3204, 17.4404]	[5.6865, 5.7365]	[-2.0391, -1.9791]	[16.6274, 16.7674]	
HPD	Standard	16.7300	5.8808	-1.9506	15.0207	
	Initno <sup>†</sup> (Guo et al., 2024)	[16.6500, 16.8100]	[5.8558, 5.9058]	[-1.9806, -1.9206]	[14.9407, 15.1007]	
	NPNet (Zhou et al., 2025)	16.7500	5.8950	-1.9440	15.9000	
	Ours	16.6700, 16.8300]	[5.8700, 5.9200]	[-1.9740, -1.9140]	[15.8200, 15.9800]	
	Ours	16.8015	5.9517	-1.8881	16.6501	
	Ours	[16.7415, 16.8615]	[5.9267, 5.9767]	[-1.9181, -1.8581]	[16.5801, 16.7201]	

increasing  $n$  yields diminishing returns. More discussion see Appendix C.11.

### 5.4. Ablation II: Necessity of Horizontal Injection

Figure 5 isolates the contribution of injection. Erasure-only improves overall stability but often plateaus on prompts whose target semantics lie far from the “averaged” seed. Adding horizontal injection consistently improves text adherence and resolves residual inconsistencies, demonstrating that *explicitly biasing the seed in a prompt-aligned horizontal direction is essential*.

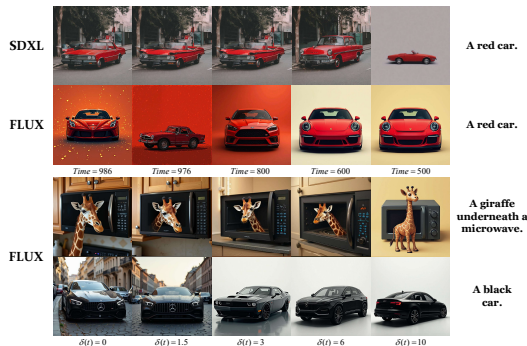


Figure 4. Impact of injection stage selection and injection strength  $\delta(t)$  on generation.

### 5.5. Ablation III: Stage Selection and Injection Strength

We study *when* and *how strongly* to inject semantics, using a unimodal timestep weight  $f(t_k) = -\left(\frac{t_k - t_*}{5}\right)^2 + 1000$ , where  $t_*$  sets the preferred stage. As Fig. 4 shows, earlier emphasis improves global layout/context, later emphasis sharpens details but can hurt coherence. Varying  $\delta(t)$ , moderate injection boosts prompt purity. More in Appendix K.

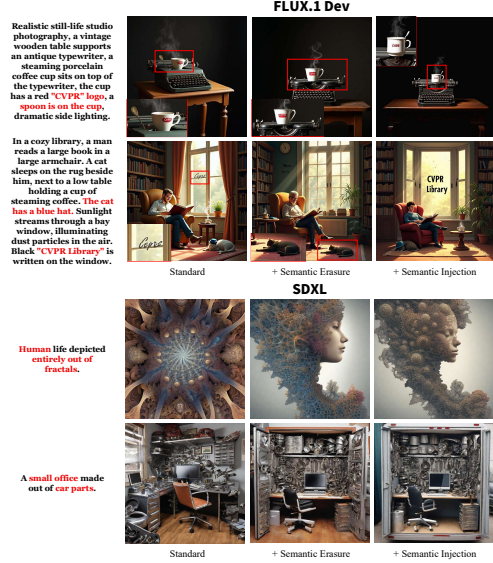


Figure 5. Impact of semantic injection. We compare Standard, erasure-only, and erasure+injection. Injection breaks the erasure plateau and improves alignment.

We also study a *horizontal step correction* that keeps the native sampler unchanged and only perturbs the per-step predicted update direction. Details are in Appendix A.2.

## 6. Conclusion

We studied the persistent *Seed Lottery* in diffusion/flow generation, where an isotropic Gaussian prior yields sharply anisotropic semantic outcomes. Our core explanation is geometric: the effective semantic map  $\Phi = \pi \circ \Psi$  induces a *degenerate pullback* semi-metric on the latent, vanishing along semantic-invariant fiber directions and remaining informative only on a low-dimensional horizontal subspace. Guided by this structure, we proposed a training-free, plug-and-play inference procedure for *horizontal seed shaping*: (i) **semantic erasure** via distribution-preserving noise aggregation (NLN), (ii) **horizontal injection** via timestep-aggregated prompt-conditioned predictions (TPW), and (iii) **spherical retraction** to stay close to the prior typical set. Across multiple backbones and modalities, our method consistently improves alignment and quality metrics and is preferred by human evaluators, while requiring no retraining and only minimal inference overhead.

## Impact Statement

This paper presents work whose goal is to advance the field of Machine Learning by improving the controllability and reliability of diffusion models. This work advances understanding and optimization of diffusion models and may enable more reliable and controllable generation, as well as inspire training-based geometry-aware improvements. The ethical and societal risks are largely those common to generative modeling—misinformation, abuse, bias, privacy, and provenance—and should be managed through responsible deployment practices and continued evaluation of downstream impacts.

## References

- Anjum, M. F. Advancing diffusion models: Alias-free resampling and enhanced rotational equivariance, 2024.
- Arvanitidis, G., Hansen, L. K., and Hauberg, S. Latent space oddity: On the curvature of deep generative models. In *International Conference on Learning Representations (ICLR)*, 2018.
- Bai, S., Chen, K., Liu, X., Wang, J., Ge, W., Song, S., Dang, K., Wang, P., Wang, S., Tang, J., Zhong, H., Zhu, Y., Yang, M., Li, Z., Wan, J., Wang, P., Ding, W., Fu, Z., Xu, Y., Ye, J., Zhang, X., Xie, T., Cheng, Z., Zhang, H., Yang, Z., Xu, H., and Lin, J. Qwen2.5-vl technical report, 2025.
- Biroli, G., Bonnaire, T., de Bortoli, V., and Mézard, M. Dynamical regimes of diffusion models. *arXiv preprint arXiv:2402.18491*, 2024.
- Blattmann, A., Dockhorn, T., Kulal, S., Mendeleevitch, D., Kilian, M., Lorenz, D., Levi, Y., English, Z., Voleti, V., Letts, A., Jampani, V., and Rombach, R. Stable video diffusion: Scaling latent video diffusion models to large datasets. *arXiv preprint arXiv:2311.15127*, 2023.
- Chen, R. T. Q. and Lipman, Y. Flow matching on general geometries. In Kim, B., Yue, Y., Chaudhuri, S., Fragkiadaki, K., Khan, M., and Sun, Y. (eds.), *International Conference on Representation Learning*, volume 2024, pp. 47922–47945, 2024.
- Collins, J., Goel, S., Deng, K., Luthra, A., Xu, L., Gundogdu, E., Zhang, X., Vicente, T. F. Y., Dideriksen, T., Arora, H., Guillaumin, M., and Malik, J. ABO: dataset and benchmarks for real-world 3d object understanding. In *IEEE/CVF Conference on Computer Vision and Pattern Recognition, CVPR 2022, New Orleans, LA, USA, June 18-24, 2022*, pp. 21094–21104. IEEE, 2022. doi: 10.1109/CVPR52688.2022.02045.
- Deitke, M., Schwenk, D., Salvador, J., Weihs, L., Michel, O., VanderBilt, E., Schmidt, L., Ehsani, K., Kembhavi, A., and Farhadi, A. Objaverse: A universe of annotated 3d objects. In *IEEE/CVF Conference on Computer Vision and Pattern Recognition, CVPR 2023, Vancouver, BC, Canada, June 17-24, 2023*, pp. 13142–13153. IEEE, 2023. doi: 10.1109/CVPR52729.2023.01263.
- Esser, P., Kulal, S., Blattmann, A., Entezari, R., Müller, J., Saini, H., Levi, Y., Lorenz, D., Sauer, A., Boesel, F., Podell, D., Dockhorn, T., English, Z., and Rombach, R. Scaling rectified flow transformers for high-resolution image synthesis. In *Forty-first International Conference on Machine Learning, ICML 2024, Vienna, Austria, July 21-27, 2024*. OpenReview.net, 2024.
- Guo, X., Liu, J., Cui, M., Li, J., Yang, H., and Huang, D. Initno: Boosting text-to-image diffusion models via initial noise optimization. In *IEEE/CVF Conference on Computer Vision and Pattern Recognition, CVPR 2024, Seattle, WA, USA, June 16-22, 2024*, pp. 9380–9389. IEEE, 2024. doi: 10.1109/CVPR52733.2024.00896.
- Hessel, J., Holtzman, A., Forbes, M., Bras, R. L., and Choi, Y. Clipscore: A reference-free evaluation metric for image captioning. In Moens, M., Huang, X., Specia, L., and Yih, S. W. (eds.), *Proceedings of the 2021 Conference on Empirical Methods in Natural Language Processing, EMNLP 2021, Virtual Event / Punta Cana, Dominican Republic, 7-11 November, 2021*, pp. 7514–7528. Association for Computational Linguistics, 2021. doi: 10.18653/V1/2021.EMNLP-MAIN.595.
- Heusel, M., Ramsauer, H., Unterthiner, T., Nessler, B., and Hochreiter, S. Gans trained by a two time-scale update rule converge to a local nash equilibrium. In Guyon, I., von Luxburg, U., Bengio, S., Wallach, H. M., Fergus, R., Vishwanathan, S. V. N., and Garnett, R. (eds.), *Advances in Neural Information Processing Systems 30: Annual Conference on Neural Information Processing Systems 2017, December 4-9, 2017, Long Beach, CA, USA*, pp. 6626–6637, 2017.
- Hu, E. J., Shen, Y., Wallis, P., Allen-Zhu, Z., Li, Y., Wang, S., Wang, L., and Chen, W. Lora: Low-rank adaptation of large language models. In *The Tenth International Conference on Learning Representations, ICLR 2022, Virtual Event, April 25-29, 2022*. OpenReview.net, 2022.
- Huang, H., Jin, X., Liu, Y., Lou, H., Xiao, C., Cui, S., Li, X., and Zou, D. Predicting scores of various aesthetic attribute sets by learning from overall score labels. In Jin, C., He, L., Song, M., and Wang, R. (eds.), *Proceedings of the 2nd International Workshop on Multimedia Content Generation and Evaluation: New Methods and Practice, McGE 2024, Melbourne, VIC, Australia, 28 October 2024 - 1 November 2024*, pp. 63–71. ACM, 2024a. doi: 10.1145/3688867.3690174.

- Huang, Z., He, Y., Yu, J., Zhang, F., Si, C., Jiang, Y., Zhang, Y., Wu, T., Jin, Q., Chanpaisit, N., Wang, Y., Chen, X., Wang, L., Lin, D., Qiao, Y., and Liu, Z. VBench: Comprehensive benchmark suite for video generative models. In *Proceedings of the IEEE/CVF Conference on Computer Vision and Pattern Recognition*, 2024b.
- Ilharco, G., Wortsman, M., Wightman, R., Gordon, C., Carlini, N., Taori, R., Dave, A., Shankar, V., Namkoong, H., Miller, J., Hajishirzi, H., Farhadi, A., and Schmidt, L. Openclip, July 2021. If you use this software, please cite it as below.
- Karras, T., Laine, S., and Aila, T. A style-based generator architecture for generative adversarial networks. In *Proceedings of the IEEE/CVF Conference on Computer Vision and Pattern Recognition (CVPR)*, 2019.
- Khanna, M., Mao, Y., Jiang, H., Haresh, S., Shacklett, B., Batra, D., Clegg, A., Undersander, E., Chang, A. X., and Savva, M. Habitat synthetic scenes dataset (HSSD-200): an analysis of 3d scene scale and realism tradeoffs for objectgoal navigation. In *IEEE/CVF Conference on Computer Vision and Pattern Recognition, CVPR 2024, Seattle, WA, USA, June 16-22, 2024*, pp. 16384–16393. IEEE, 2024. doi: 10.1109/CVPR52733.2024.01550.
- Kirstain, Y., Polyak, A., Singer, U., Matiana, S., Penna, J., and Levy, O. Pick-a-pic: an open dataset of user preferences for text-to-image generation. In *Proceedings of the 37th International Conference on Neural Information Processing Systems, NIPS '23, Red Hook, NY, USA, 2023*. Curran Associates Inc.
- Labs, B. F. Flux. <https://github.com/black-forest-labs/flux>, 2024.
- Li, X. Visual language hypothesis. *arXiv preprint arXiv:2512.23335*, 2025. arXiv version may appear as early 2026 depending on revision.
- Lin, Z., Pathak, D., Li, B., Li, J., Xia, X., Neubig, G., Zhang, P., and Ramanan, D. Evaluating text-to-visual generation with image-to-text generation. *arXiv preprint arXiv:2404.01291*, 2024.
- Lou, A., Xu, M., and Ermon, S. Scaling riemannian diffusion models. In *Advances in Neural Information Processing Systems (NeurIPS)*, 2023.
- Ma, X., Liu, W., Zhang, P., and Xu, N. 3d-rpe: Enhancing long-context modeling through 3d rotary position encoding. In Walsh, T., Shah, J., and Kolter, Z. (eds.), *AAAI-25, Sponsored by the Association for the Advancement of Artificial Intelligence, February 25 - March 4, 2025, Philadelphia, PA, USA*, pp. 24804–24811. AAAI Press, 2025. doi: 10.1609/AAAI.V39I23.34662.
- O’Neill, B. The fundamental equations of a submersion. *Michigan Mathematical Journal*, 13(4):459–469, 1966.
- Oquab, M., Darcet, T., Moutakanni, T., Vo, H. V., Szafraniec, M., Khalidov, V., Fernandez, P., Haziza, D., Massa, F., El-Nouby, A., Assran, M., Ballas, N., Galuba, W., Howes, R., Huang, P., Li, S., Misra, I., Rabbat, M., Sharma, V., Synnaeve, G., Xu, H., Jégou, H., Mairal, J., Labatut, P., Joulin, A., and Bojanowski, P. Dinov2: Learning robust visual features without supervision. *Trans. Mach. Learn. Res.*, 2024, 2024.
- Pernias, P., Rampas, D., Richter, M. L., Pal, C., and Aubreville, M. Würstchen: An efficient architecture for large-scale text-to-image diffusion models. In *The Twelfth International Conference on Learning Representations, ICLR 2024, Vienna, Austria, May 7-11, 2024*. OpenReview.net, 2024.
- Phillips, J. M. and Venkatasubramanian, S. A gentle introduction to the kernel distance. *CoRR*, abs/1103.1625, 2011.
- Podell, D., English, Z., Lacey, K., Blattmann, A., Dockhorn, T., Müller, J., Penna, J., and Rombach, R. SDXL: improving latent diffusion models for high-resolution image synthesis. In *The Twelfth International Conference on Learning Representations, ICLR 2024, Vienna, Austria, May 7-11, 2024*. OpenReview.net, 2024a.
- Podell, D., English, Z., Lacey, K., Blattmann, A., Dockhorn, T., Müller, J., Penna, J., and Rombach, R. SDXL: Improving latent diffusion models for high-resolution image synthesis. In *International Conference on Learning Representations (ICLR)*, 2024b.
- Qi, Z., Bai, L., Xiong, H., and Xie, Z. Not all noises are created equally: diffusion noise selection and optimization. *ArXiv*, abs/2407.14041, 2024. doi: 10.48550/arxiv.2407.14041.
- Raffel, C., Shazeer, N., Roberts, A., Lee, K., Narang, S., Matena, M., Zhou, Y., Li, W., and Liu, P. J. Exploring the limits of transfer learning with a unified text-to-text transformer. *J. Mach. Learn. Res.*, 21:140:1–140:67, 2020.
- Rombach, R., Blattmann, A., Lorenz, D., Esser, P., and Ommer, B. High-resolution image synthesis with latent diffusion models. In *IEEE/CVF Conference on Computer Vision and Pattern Recognition, CVPR 2022, New Orleans, LA, USA, June 18-24, 2022*, pp. 10674–10685. IEEE, 2022. doi: 10.1109/CVPR52688.2022.01042.
- Ronneberger, O., Fischer, P., and Brox, T. U-net: Convolutional networks for biomedical image segmentation. In Navab, N., Hornegger, J., III, W. M. W., and Frangi, A. F. (eds.), *Medical Image Computing and Computer-Assisted Intervention - MICCAI 2015 - 18th International*

- Conference Munich, Germany, October 5 - 9, 2015, Proceedings, Part III*, volume 9351 of *Lecture Notes in Computer Science*, pp. 234–241. Springer, 2015. doi: 10.1007/978-3-319-24574-4\\_28.
- Saharia, C., Chan, W., Saxena, S., Li, L., Whang, J., Denton, E. L., Ghasemipour, K., Gontijo Lopes, R., Karagol Ayan, B., Salimans, T., Ho, J., Fleet, D. J., and Norouzi, M. Photorealistic text-to-image diffusion models with deep language understanding. In Koyejo, S., Mohamed, S., Agarwal, A., Belgrave, D., Cho, K., and Oh, A. (eds.), *Advances in Neural Information Processing Systems 35*, pp. 36479–36494. Curran Associates, Inc., 2022.
- Stojanov, S., Thai, A., and Rehg, J. M. Using shape to categorize: Low-shot learning with an explicit shape bias. 2021.
- Szegedy, C., Vanhoucke, V., Ioffe, S., Shlens, J., and Wojna, Z. Rethinking the inception architecture for computer vision. In *2016 IEEE Conference on Computer Vision and Pattern Recognition, CVPR 2016, Las Vegas, NV, USA, June 27-30, 2016*, pp. 2818–2826. IEEE Computer Society, 2016. doi: 10.1109/CVPR.2016.308.
- Team, Z.-I. Z-image: An efficient image generation foundation model with single-stream diffusion transformer. *arXiv preprint arXiv:2511.22699*, 2025.
- Ventura, E., Achilli, B., Silvestri, G., Lucibello, C., and Ambrogioni, L. Manifolds, random matrices and spectral gaps: The geometric phases of generative diffusion. In Yue, Y., Garg, A., Peng, N., Sha, F., and Yu, R. (eds.), *International Conference on Representation Learning*, volume 2025, pp. 88317–88338, 2025.
- Wang, A., Ai, B., Wen, B., Mao, C., Xie, C., Chen, D., Yu, F., Zhao, H., Yang, J., Zeng, J., Wang, J., Zhang, J., Zhou, J., Wang, J., Chen, J., Zhu, K., Zhao, K., Yan, K., Huang, L., Meng, X., Zhang, N., Li, P., Wu, P., Chu, R., Feng, R., Zhang, S., Sun, S., Fang, T., Wang, T., Gui, T., Weng, T., Shen, T., Lin, W., Wang, W., Wang, W., Zhou, W., Wang, W., Shen, W., Yu, W., Shi, X., Huang, X., Xu, X., Kou, Y., Lv, Y., Li, Y., Liu, Y., Wang, Y., Zhang, Y., Huang, Y., Li, Y., Wu, Y., Liu, Y., Pan, Y., Zheng, Y., Hong, Y., Shi, Y., Feng, Y., Jiang, Z., Han, Z., Wu, Z., and Liu, Z. Wan: Open and advanced large-scale video generative models. *CoRR*, abs/2503.20314, 2025. doi: 10.48550/ARXIV.2503.20314.
- Wu, X., Hao, Y., Sun, K., Chen, Y., Zhu, F., Zhao, R., and Li, H. Human preference score v2: A solid benchmark for evaluating human preferences of text-to-image synthesis. *arXiv preprint arXiv:2306.09341*, 2023.
- Xiang, J., Lv, Z., Xu, S., Deng, Y., Wang, R., Zhang, B., Chen, D., Tong, X., and Yang, J. Structured 3d latents for scalable and versatile 3d generation. In *IEEE/CVF Conference on Computer Vision and Pattern Recognition, CVPR 2025, Nashville, TN, USA, June 11-15, 2025*, pp. 21469–21480. Computer Vision Foundation / IEEE, 2025. doi: 10.1109/CVPR52734.2025.02000.
- Xu, J., Liu, X., Wu, Y., Tong, Y., Li, Q., Ding, M., Tang, J., and Dong, Y. Imagereward: Learning and evaluating human preferences for text-to-image generation. In Oh, A., Naumann, T., Globerson, A., Saenko, K., Hardt, M., and Levine, S. (eds.), *Advances in Neural Information Processing Systems 36: Annual Conference on Neural Information Processing Systems 2023, NeurIPS 2023, New Orleans, LA, USA, December 10 - 16, 2023*, 2023.
- Zhang, R., Isola, P., Efros, A. A., Shechtman, E., and Wang, O. The unreasonable effectiveness of deep features as a perceptual metric. In *2018 IEEE Conference on Computer Vision and Pattern Recognition, CVPR 2018, Salt Lake City, UT, USA, June 18-22, 2018*, pp. 586–595. Computer Vision Foundation / IEEE Computer Society, 2018. doi: 10.1109/CVPR.2018.00068.
- Zhou, Z., Shao, S., Bai, L., Zhang, S., Xu, Z., Han, B., and Xie, Z. Golden noise for diffusion models: A learning framework. In *International Conference on Computer Vision*, 2025.
- Zou, Z., Cheng, W., Cao, Y., Huang, S., Shan, Y., and Zhang, S. Sparse3d: Distilling multiview-consistent diffusion for object reconstruction from sparse views. In Wooldridge, M. J., Dy, J. G., and Natarajan, S. (eds.), *Thirty-Eighth AAAI Conference on Artificial Intelligence, AAAI 2024, Thirty-Sixth Conference on Innovative Applications of Artificial Intelligence, IAAI 2024, Fourteenth Symposium on Educational Advances in Artificial Intelligence, EAAI 2014, February 20-27, 2024, Vancouver, Canada*, pp. 7900–7908. AAAI Press, 2024. doi: 10.1609/AAAI.V38I7.28626.

# Appendix: Latent Space Degeneracy in Diffusion Model

## A. Global Overview of Latent Space Degeneracy

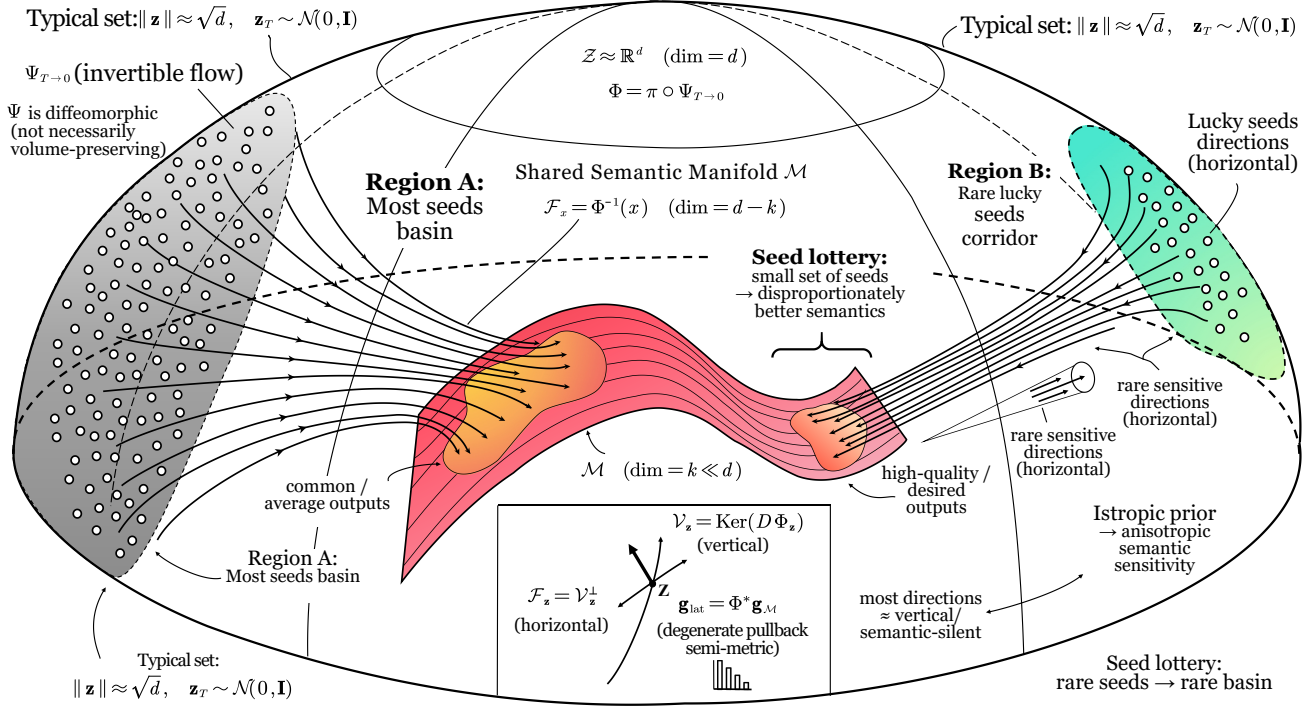


Figure 6. Geometric Overview of Latent Space Degeneracy

### A.1. Reading Guide for Figure 6

This section details the geometric intuition visualized in Figure 6, decomposing the generative process into semantic basins, fiber bundles, and the seed lottery phenomenon.

#### A.1.1. OUTPUT SIDE: SEMANTIC BASINS ON $\mathcal{M}$

The partitioned regions on the central manifold  $\mathcal{M}$  (center of Figure 6) represent *semantic basins*: neighborhoods where generated samples share high semantic similarity under the projection  $\pi(\cdot)$ . These basins visualize the empirical concentration of probability mass. Under fixed conditioning, the reverse dynamics  $\Psi_{T \rightarrow 0}$  tends to collapse vast latent regions into discrete, stable semantic modes, distinguished in the diagram as the broad “common/average” patch (left) versus the distinct “high-quality/desired” patch (right).

#### A.1.2. INTERMEDIATE GEOMETRY: FIBER BUNDLES AND COLLAPSE

A core structural element in Figure 6 is the **fiber bundle** geometry, depicted as black filaments converging into specific basins. This illustrates the many-to-one nature of the generative flow. Formally, a fiber  $\mathcal{F}_x$  leading to semantics  $x$  can be defined as:

$$\mathcal{F}_x = \{z_t \in \mathcal{Z} \mid \pi(D(\Psi_{t \rightarrow 0}(z_t))) \approx x\}. \quad (29)$$

Visually, these sets form sparse “channels.” The inset highlights the local anisotropy of these fibers:

- **Vertical perturbations**  $\mathcal{V}_z$  (tangent to the fiber, marked by thin arrows in the inset) are absorbed by the collapse, affecting only high-frequency details.
- **Horizontal perturbations**  $\mathcal{H}_z$  (transverse to the fiber, marked by the thicker arrow in the inset) induce semantic shifts, forcing the trajectory to jump to a different bundle.

*Note:* This fiber structure characterizes the *intermediate* flow geometry ( $0 < t < T$ ), explaining why semantic changes require specific, anisotropic directions of movement.

### A.1.3. INPUT SIDE: THE SEED LOTTERY

The **Seed Lottery module** (outer shell) visualizes the entrance-level variability. Even under identical conditioning, the initial noise  $z_T$  determines the *entry point* into the flow field, significantly biasing the final outcome:

- **Region A: Most Seeds (Left Basin):** The vast majority of typical seeds (represented by the dense cluster of dots) land in regions where the flow  $\Psi$  leads inevitably into the generic basin.
- **Region B: Lucky Seeds (Right Corridor):** A small measure of seeds falls into a specific “sensitivity corridor” (the narrow wedge on the right), allowing the trajectory to access high-quality semantic basins.

This geometric separation clarifies why “trying multiple seeds” is practically effective: it serves as a Monte Carlo search for a favorable initialization that lies within the basin of attraction of a desirable fiber bundle.

### A.1.4. SUMMARY: INTERACTION OF GEOMETRY AND SAMPLING

Figure 6 thus unifies two distinct sources of variation:

1. **Entrance Selection (Seed Lottery):** The choice of  $z_T$  determines *which route* (Region A vs. Region B) is entered.
2. **Process Collapse (Fibers):** Once inside a bundle, the anisotropic geometry dictates that most deviations are suppressed (vertical), while only specific directions (horizontal) alter the semantics.

## A.2. Horizontal Step-Corrected Sampler

To demonstrate the generality of our theory, we have designed a new sampler, which is included here only as an extended discussion and is not the focus of this paper.

### A.2.1. MOTIVATION

Under the geometric view of latent-space degeneracy, the latent space contains directions that weakly affect semantics (“vertical” directions) and directions that strongly affect semantic alignment (“horizontal” directions). Random seeds can induce large variations by perturbing trajectories along vertical directions. A sampler that mildly biases the update toward a more stable horizontal component can therefore reduce seed lottery effects while preserving the base sampler behavior.

### A.2.2. METHOD: PER-STEP HORIZONTAL CORRECTION OF THE PREDICTED UPDATE

Let  $x_i$  denote the latent state at sampling step  $i$ , and let  $v_i$  denote the model-predicted update direction at that step (the `noise_pred/vector-field` output in our implementation). The base sampler produces

$$x_{i+1} = \text{Step}(x_i, v_i, t_i), \tag{30}$$

where  $\text{Step}(\cdot)$  is the native step function of the sampler/scheduler.

We define a cheap horizontal proxy by removing from  $v_i$  the component that is colinear with the current latent  $x_i$ :

$$h_i = v_i - \text{Proj}_{x_i}(v_i), \quad \text{Proj}_{x_i}(v_i) = \frac{\langle v_i, x_i \rangle}{\langle x_i, x_i \rangle + \varepsilon} x_i, \tag{31}$$

where  $\langle \cdot, \cdot \rangle$  is the inner product over all latent dimensions (per sample), and  $\varepsilon$  is a small constant for numerical stability. Intuitively,  $h_i$  is the tangential component of the predicted update relative to the current latent direction.

We then apply a step correction by adding a scaled horizontal component to the original update:

$$\tilde{v}_i = v_i + \alpha_i h_i, \tag{32}$$

and feed  $\tilde{v}_i$  into the base sampler step:

$$x_{i+1} = \text{Step}(x_i, \tilde{v}_i, t_i). \tag{33}$$

### A.2.3. SCHEDULING AND STABILITY CONTROLS

To avoid over-correction (which may reduce high-frequency details), we apply three practical stabilizers.

**(i) Time-gated application.** We only apply correction during an early-to-mid portion of the trajectory:

$$\alpha_i = 0 \quad \text{if} \quad \text{prog}_i \notin [\rho_s, \rho_e], \quad \text{prog}_i = \frac{i}{N-1}, \tag{34}$$

where  $N$  is the number of sampling steps. In our experiments, we set  $\rho_s = 0$  and  $\rho_e = 0.5$  (i.e., apply correction only in the first half).

**(ii) Decaying correction strength.** Within the active interval, the correction strength decays toward later steps:

$$\alpha_i = \alpha_0 \cdot (1 - \text{prog}_i)^p, \tag{35}$$

with  $p > 0$ . We use  $p = 2$  unless otherwise noted.

**(iii) Relative-magnitude clamp.** We bound the correction magnitude relative to the base update to prevent instability:

$$\|\alpha_i h_i\| \leq \tau \|v_i\|, \tag{36}$$

implemented by scaling  $\alpha_i$  if the inequality is violated. We use  $\tau = 0.5$  in our default setting.

### A.2.4. DISCUSSION

The proposed step correction is intentionally minimal: it preserves the base sampler’s step operator `Step` while introducing a controlled bias toward a tangential (horizontal) component of the predicted update. Empirically, restricting correction to early steps and decaying its strength are crucial for maintaining sharpness while improving seed robustness and semantic consistency.

### A.2.5. QUALITATIVE COMPARISON AND PRACTICAL IMPACT

Figure 7 qualitatively compares the *native sampler* (baseline) against our *horizontal step-corrected* variant under the same prompts, resolution, and inference budget. The corrected sampler consistently reduces seed-induced failures and improves prompt compliance in scenarios that are known to be brittle for text-to-image generators (e.g., text rendering and global composition).

**Text rendering and structured attributes.** In the stylized illustration example (“drink tea, eat cake”) and the poster-like scene (“Welcome to ICML ICML 2026 Seoul Korea”), the corrected sampler produces noticeably more legible and less deformed text. This is a common failure mode for diffusion/flow samplers and is often amplified by seed lottery effects; our results indicate that the correction improves robustness specifically on these high-level, structure-sensitive attributes.

**Global composition stability.** In the realistic still-life example (typewriter with an oversized cup and a logo), the corrected sampler better preserves the intended size relationship (the cup being larger than the typewriter) and yields a more coherent arrangement. This supports our interpretation that the correction stabilizes the sampling trajectory during the *early structural formation phase*, reducing abrupt global rearrangements across seeds.

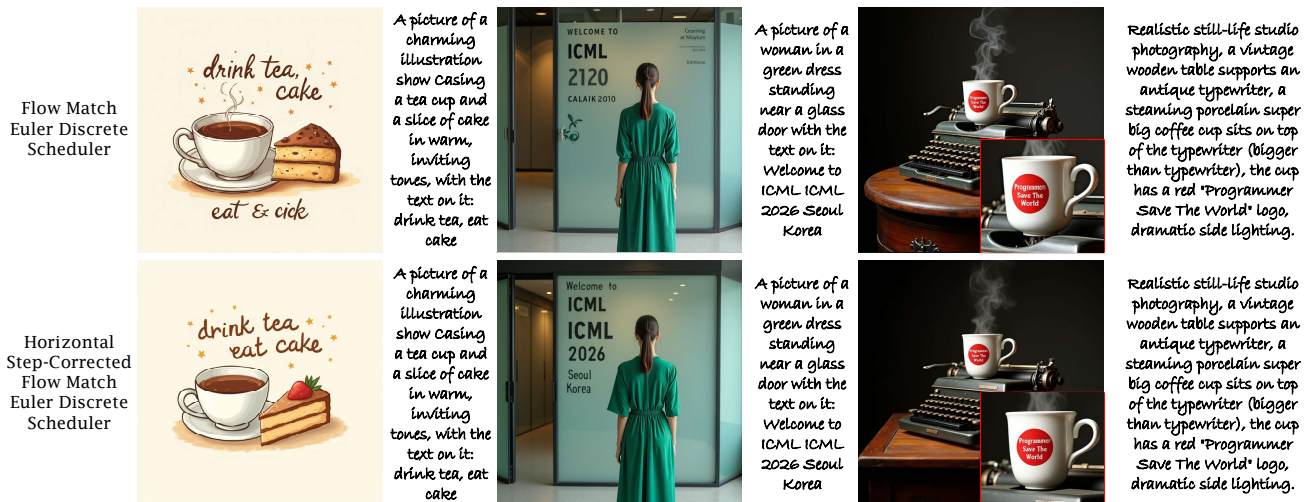


Figure 7. Qualitative comparison under matched inference budgets. Baseline (native sampler) vs. our horizontal step-corrected sampler on three prompts. The corrected sampler improves robustness to seed lottery effects, yielding more coherent text and more stable global composition while preserving detail through time-gated, decayed correction.

**Mechanistic link to the sampler design.** Our correction is intentionally *time-gated* and *decayed*: it is applied only in the early-to-mid portion of the trajectory and gradually turned off toward later steps. This design reflects a practical division of labor in modern samplers: earlier steps largely determine coarse semantics and layout, while later steps refine high-frequency details. By focusing correction on the early phase, we obtain improved semantic and compositional consistency; by turning it off later, we avoid over-regularizing the refinement stage, which can otherwise lead to mild blurring. All qualitative results in Figure 7 use this default schedule.

## B. Sensitivity of the geometric diagnostics to the choice of semantic map $\pi$

This appendix isolates a single question: *do our **geometry-only** diagnostics meaningfully depend on the particular choice of semantic map  $\pi$  used to define  $\Phi = \pi \circ \Psi$ ?* The goal here is **not** to claim that any downstream performance relationship (e.g., geometry- $\Delta$  correlations) must remain invariant across evaluators or representations. Rather, the goal is to show that the *diagnostic procedure itself*—prompt stratification via local Jacobian-spectrum statistics—is stable under a reasonable range of frozen, widely used learned semantic maps.

**Notation.** Throughout this appendix,  $\Psi$  (a.k.a.  $G$  in the main text) denotes the generator mapping from base noise  $z$  to an output image  $x = \Psi(z)$ ; in all experiments, we instantiate  $\Psi$  with the Z-Image generator (Team, 2025), and we study the composed semantic map  $\Phi = \pi \circ \Psi$ .

**Semantic maps  $\pi$  considered (six vector-valued instantiations).** We evaluate six frozen choices of  $\pi$  spanning (i) CLIP<sup>1</sup>, (ii) OpenCLIP/VLM-style embeddings<sup>2</sup>, and (iii) DINOv2 image embeddings fused with CLIP-text<sup>3</sup>. For each backbone family, we consider two fusion rules: elementwise image-text product (`itprod`) and concatenation (`concat`). The embedding dimension  $D$  can depend on the concrete implementation and is reported *as realized in this run* (from the script outputs / logs).

- CLIP: `clip_ViT-L-14_openai_itprod`, `clip_ViT-L-14_openai_concat`.
- VLM: `vlm_ViT-H-14_laion2b_s32b_b79k_itprod`, `vlm_ViT-H-14_laion2b_s32b_b79k_concat`.
- DINOv2 + CLIP-text: `dinov2_vitb14_cliptext_itprod`, `dinov2_vitb14_cliptext_concat`.

**Jacobian estimator and spectrum statistics.** For each prompt, we estimate the local Jacobian of  $\Phi = \pi \circ \Psi$  at a fixed base noise using symmetric finite differences along random directions. We probe  $r = 6$  random directions; hence the maximum observable rank (and thus the maximum possible effective-rank / participation ratio) is upper-bounded by 6. We report four spectrum statistics (computed from the singular values of the probed Jacobian): (i) smallest singular value  $s_{\min}$  (larger suggests less local collapse), (ii) effective rank (entropy-based), (iii) participation ratio, and (iv) condition number  $\kappa$  (here reported as `cond`).

**How to read the plots in this appendix.** The evaluator script produces three families of plots:

- **Violin plots** (`fig_spectrum_stats_violin_*`): distribution across prompts of the *prompt-level mean* of each metric (each prompt aggregated over seeds).
- **Heatmaps** (`fig_pi_spearman_heatmap_*`): pairwise Spearman correlation between prompt-level means across different  $\pi$  (agreement in prompt ranking).
- **Seed-stability boxplots** (`fig_seed_stability_box_*`): distribution across prompts of the within-prompt seed variability (e.g., per-prompt std across seeds).

The takeaways below directly correspond to these three plot types.

**Main observation (geometry-only robustness).** Changing  $\pi$  can shift the *numerical scale* of some spectrum proxies (most visibly  $s_{\min}$  and `cond`), but the diagnostics remain usable for prompt stratification: across all six  $\pi$ , the measured spectrum statistics concentrate near a consistent low-dimensional regime (effective-rank and participation ratio close to the probe ceiling  $r = 6$ ), and prompt-level distributions remain well-behaved rather than degenerating.

<sup>1</sup><https://github.com/openai/CLIP>

<sup>2</sup>[https://github.com/mlfoundations/open\\_clip](https://github.com/mlfoundations/open_clip)

<sup>3</sup><https://github.com/facebookresearch/dinov2>

**Scale sensitivity vs. structural invariance across  $\pi$ .** Table 4 summarizes prompt-averaged metrics (mean across prompts with 95% bootstrap CIs computed on prompt-level means, 211 prompts from HPD dataset). A clear pattern is:

- $s_{\min}$  **is scale-sensitive across  $\pi$ .** The prompt-averaged  $s_{\min}$  varies substantially across representations (e.g., from  $\approx 0.040$  to  $\approx 0.066$ ), consistent with  $\pi$  changing the local sensitivity units.
- **Effective-rank / participation ratio are comparatively stable.** Across  $\pi$ , effective-rank stays in a narrow band around  $\approx 5.37$ – $5.44$  (out of a maximum of 6), and participation ratio stays around  $\approx 4.82$ – $4.98$ . This is the core “local anisotropy” signal: dependence concentrates into a small number of dominant directions, and this qualitative shape is not tied to any single embedding choice.

In other words, the *absolute* scale of “how sensitive”  $\pi \circ \Psi$  is can vary, but the *relative structure* implied by the spectrum statistics remains consistent enough to support prompt stratification.

**Seed stability: turning a qualitative claim into a quantitative one.** To avoid purely qualitative statements, we report (Table 4) the *mean within-prompt standard deviation across seeds* for each metric under each  $\pi$  (the evaluator also plots the full distribution). In this run:

- The **largest seed-induced spread** appears in `cond` (within-prompt std means roughly  $\approx 1.16$ – $1.54$  depending on  $\pi$ ) and  $s_{\min}$  (roughly  $\approx 0.012$ – $0.023$ ).
- **Across  $\pi$ , seed-stability differences are modest for rank-type metrics** (effective-rank within-prompt std means differ by only  $\sim 0.04$  across all  $\pi$ ), while  $s_{\min}$  is more sensitive (up to about a  $2\times$  range in within-prompt std means between some  $\pi$  choices).

Practically, this means: if the main-text argument leans most heavily on *rank-type* conclusions (“few directions dominate”), it is especially robust to seed noise; if it leans on  $s_{\min}$  as an “approximate submersion” proxy, then averaging across multiple seeds (as we do) is important for reliable prompt-level stratification.

**Geometry– $\Delta$  correlations: why variability across  $\pi$  is expected.** We also compute prompt-level Spearman correlations between geometry metrics and  $\Delta$  (performance gain) under a *fixed evaluator*. These correlations are not the target of this appendix and are *not expected* to be invariant:  $\Delta$  is fundamentally a property of an evaluator and its alignment with the semantic representation. Accordingly, in this run the geometry– $\Delta$  correlations are *small-to-moderate* and can vary in magnitude (and occasionally sign) across  $\pi$ . This does not weaken the geometry-only claim (prompt stratification / local anisotropy); it simply reflects that *linking geometry to a particular downstream score requires evaluator alignment*, which is an orthogonal issue.

**Failure modes / boundary conditions (what this does *not* guarantee).** While the diagnostics are stable in aggregate, there are realistic regimes where we expect weaker stability or lower  $\pi$ – $\pi$  agreement:

- **Prompts with brittle semantics** (e.g., fine-grained counting, exact attribute conjunctions, text-heavy scenes) can amplify seed sensitivity because small pixel-level changes may flip discrete semantic judgments in embeddings.
- **Weaker or misaligned  $\pi$  choices** (smaller backbones, poorer vision–language alignment, or embeddings trained on mismatched domains) can reduce promptwise agreement across  $\pi$  (lower Spearman heatmap coherence), making cross- $\pi$  conclusions less sharp.

Empirically, these show up as prompts with unusually large within-prompt IQR/std (seed instability) or as outliers that move substantially across  $\pi$  in the heatmaps. We treat these as expected boundary cases rather than contradictions: the diagnostics are intended as *local, approximate* geometric summaries, not as globally uniform guarantees.

**Takeaway.** Across six strong and diverse semantic maps  $\pi$ , the geometry-only diagnostics remain well-defined and practically usable: they consistently reveal a low-dimensional, anisotropic dependence of semantics on the latent (relative to the probe ceiling  $r = 6$ ), enabling prompt stratification without committing to any single embedding choice. Downstream geometry– $\Delta$  correlations vary with  $\pi$  as expected (evaluator alignment), but this does not affect the core geometry-only conclusion.

Table 4. **Prompt-averaged geometry diagnostics across  $\pi$  (this run).** Mean and 95% bootstrap CI are computed across prompts using prompt-level means (seeds aggregated per prompt). Seed stability is summarized by the mean within-prompt standard deviation across seeds. Embedding dimensions  $D$  should be taken from the script outputs/logs for this run.

$\pi$ (name)	$s_{\min}$ mean [95% CI]	erank mean [95% CI]	PR mean [95% CI]	cond mean [95% CI]
clip_ViT-L-14_itprod	0.03965 [0.03703, 0.04239]	5.3866 [5.3674, 5.4051]	4.8914 [4.8619, 4.9202]	3.8715 [3.7811, 3.9691]
clip_ViT-L-14_concat	0.04267 [0.04020, 0.04530]	5.4439 [5.4269, 5.4600]	4.9820 [4.9550, 5.0080]	3.5917 [3.5167, 3.6722]
vlm_ViT-H-14_itprod	0.04799 [0.04547, 0.05066]	5.3393 [5.3217, 5.3559]	4.8153 [4.7881, 4.8411]	4.0897 [4.0105, 4.1768]
vlm_ViT-H-14_concat	0.04917 [0.04682, 0.05160]	5.4338 [5.4206, 5.4462]	4.9647 [4.9433, 4.9846]	3.6332 [3.5763, 3.6945]
dinov2_vitb14_itprod	0.06581 [0.06177, 0.06997]	5.3703 [5.3519, 5.3889]	4.8652 [4.8362, 4.8941]	3.9588 [3.8689, 4.0507]
dinov2_vitb14_concat	0.04712 [0.04416, 0.05012]	5.3813 [5.3628, 5.3998]	4.8816 [4.8520, 4.9107]	3.8933 [3.8036, 3.9844]

**Seed stability (mean within-prompt std across seeds).**  $s_{\min}$ : {0.0116, 0.0128, 0.0134, 0.0135, 0.0163, 0.0228}; erank: {0.2818–0.3195}; PR: {0.4465–0.5166}; cond: {1.1624–1.5354}.

## The Determinism of Randomness: Latent Space Degeneracy in Diffusion Model

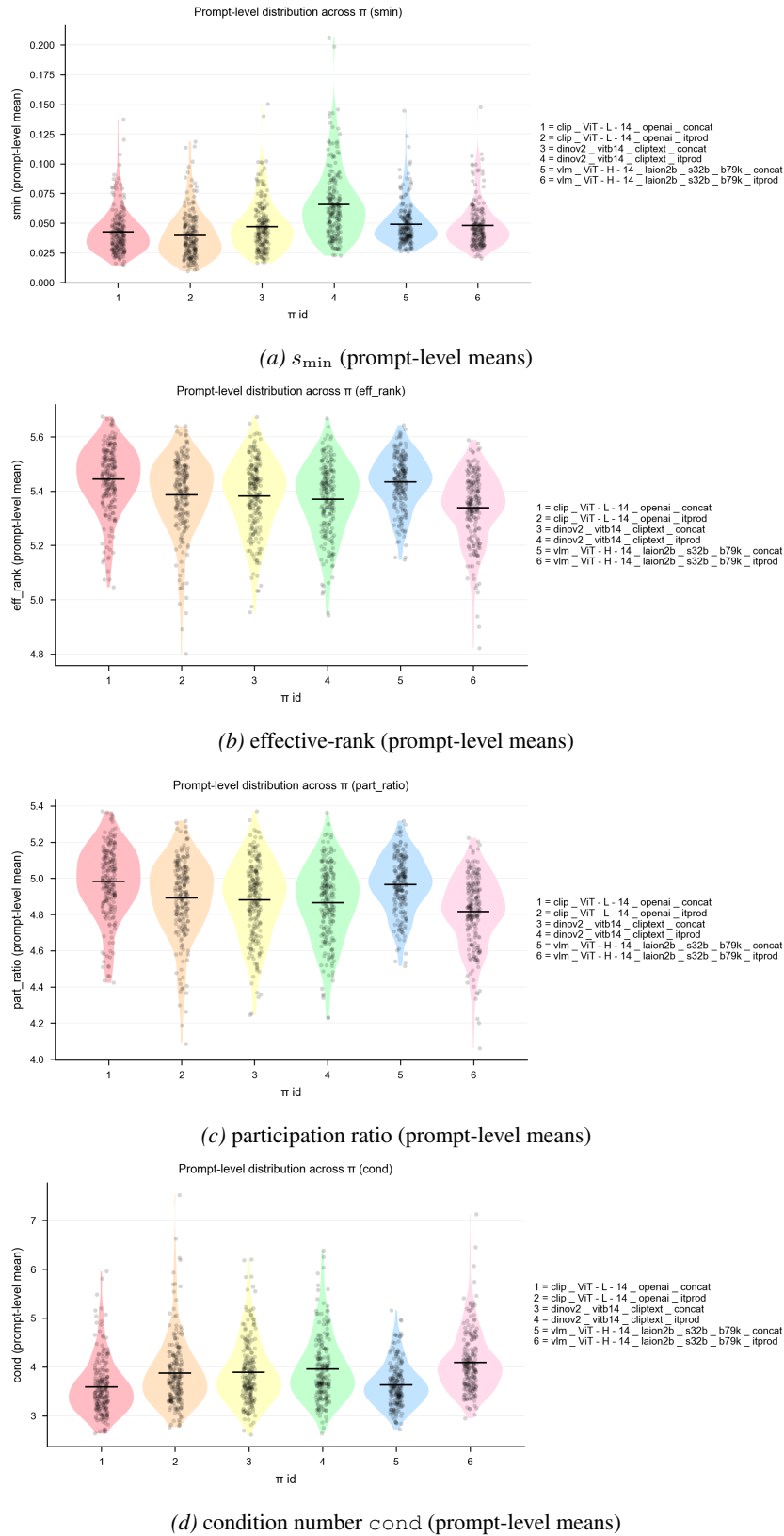


Figure 8. Prompt-level distributions of Jacobian-spectrum statistics across  $\pi$ . Each panel shows the distribution across prompts of the prompt-level mean (aggregated over seeds) for a given metric, separately for each  $\pi$ . These plots diagnose how much the *scale* and *spread* of each metric changes with  $\pi$ .

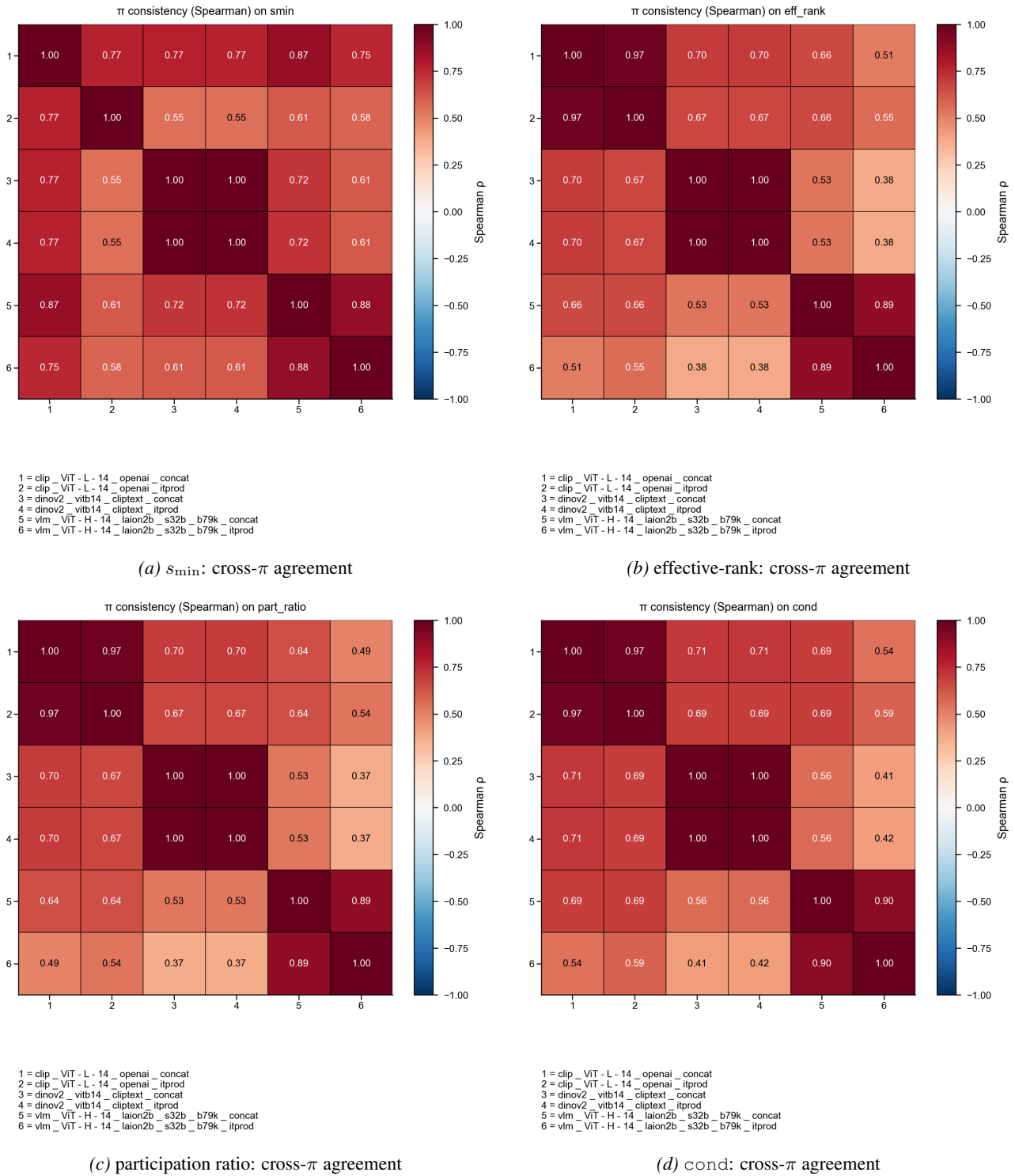


Figure 9. Pairwise Spearman agreement across  $\pi$  (prompt-level means). Each heatmap reports promptwise rank correlation between two  $\pi$  choices for the same metric. High agreement supports the claim that prompt stratification does not hinge on a single semantic map.

## The Determinism of Randomness: Latent Space Degeneracy in Diffusion Model

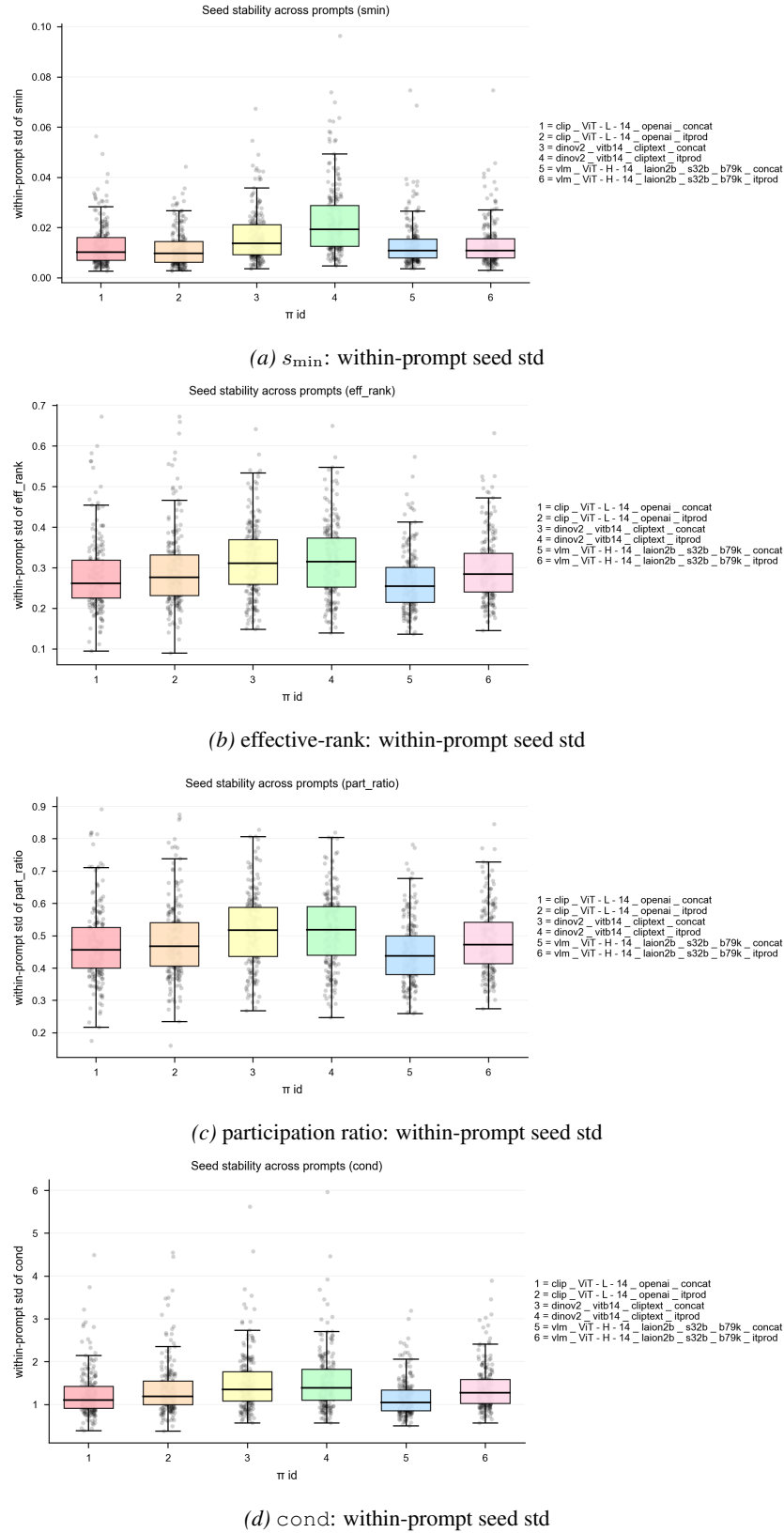


Figure 10. Seed stability of geometry diagnostics across  $\pi$ . Each panel shows the distribution across prompts of the within-prompt standard deviation over seeds for the indicated metric. This quantifies how much seed noise affects the diagnostic at the prompt level, and how that sensitivity varies with  $\pi$ .

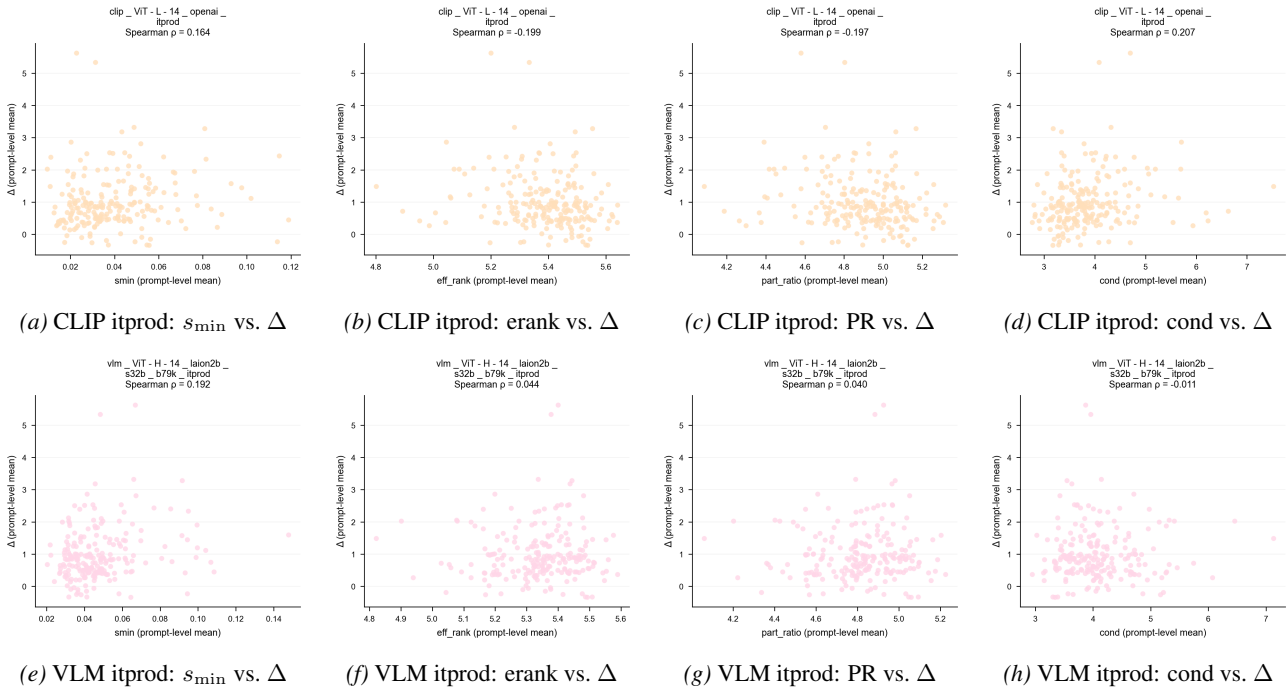


Figure 11. **Geometry- $\Delta$  correlations depend on evaluator alignment (illustrative).** Each scatter uses prompt-level means and reports Spearman correlation in the title. Variability across  $\pi$  is expected because  $\Delta$  is evaluator-dependent; the geometry-only conclusions rely instead on prompt stratification and spectrum shape, which remain stable across  $\pi$ .

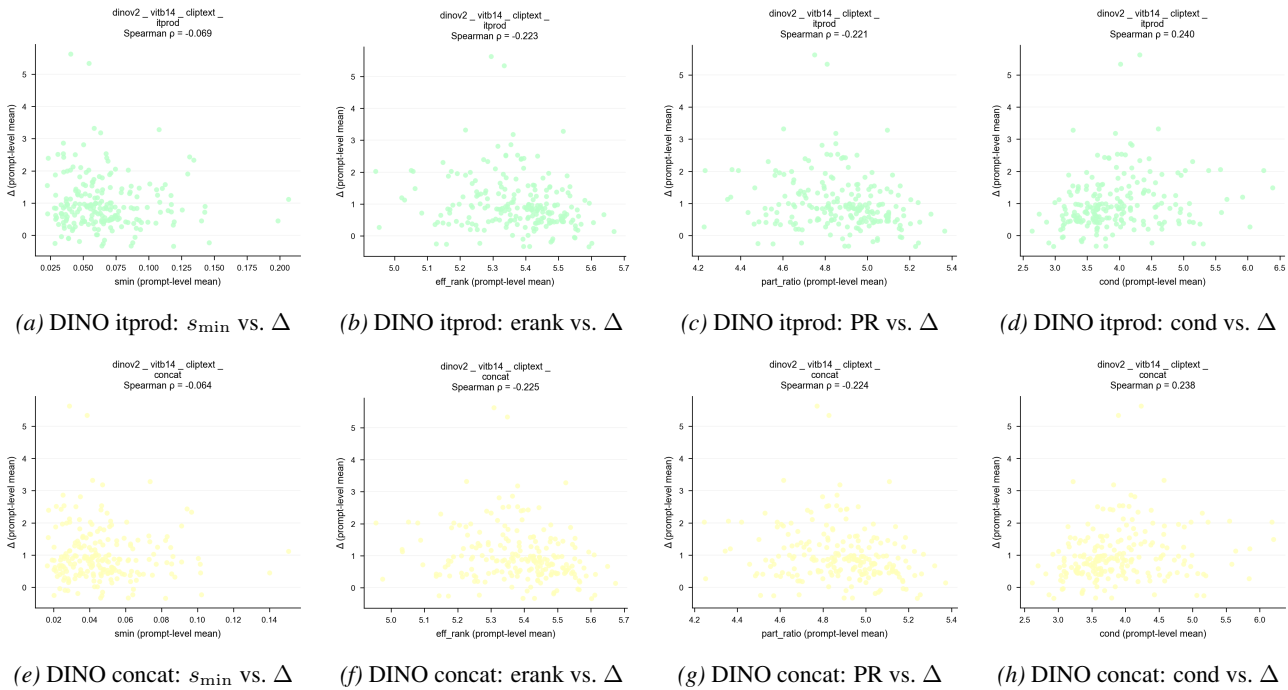


Figure 12. **Geometry- $\Delta$  correlations for DINO-based  $\pi$  (illustrative).** Same as Fig. 11, but for DINOv2 image features fused with CLIP-text (itprod/concat). These plots are included for completeness; variability across  $\pi$  is expected because  $\Delta$  is evaluator-dependent.

Table 5. Notation summary. Bold symbols denote vectors; calligraphic symbols denote sets/manifolds.

Symbol	Type	Description
$\mathcal{Z} \cong \mathbb{R}^d$	space	Seed/latent initialization space.
$d$	integer	Latent dimension.
$t \in [0, T]$	scalar	Continuous diffusion/flow time (from noise time $T$ to data time 0).
$T$	scalar	Terminal time / initial-noise time.
$\{z_t\}_{t \in [0, T]}$	trajectory	Latent state along the sampling dynamics.
$z_T, z_0$	vector	Initial seed at time $T$ ; final latent at time 0.
$Z_T$	r.v.	Random initial seed, $Z_T \sim \mathcal{N}(0, I_d)$ .
$\mathcal{N}(0, I_d)$	distribution	Isotropic Gaussian prior in $\mathbb{R}^d$ .
$I_d$	matrix	$d \times d$ identity matrix.
$\mathcal{M}$	manifold	Semantic manifold (intrinsic dimension $k \ll d$ ).
$k$	integer	Intrinsic semantic dimension.
$\mathcal{X}$	space	Output/data space (e.g., images/videos/3D assets).
$D$	integer	Feature/embedding dimension (e.g., CLIP/DINO).
$v_\theta(z_t, t; y)$	vector field	Learned drift/velocity field (parameter $\theta$ ), conditioned on prompt $y$ .
$\theta$	parameters	Trainable parameters of the backbone model.
$y$ (or $\mathbf{y}$ )	condition	Conditioning signal (e.g., text prompt / prompt embedding).
$\Psi_{T \rightarrow 0}$	map	Flow/sampling map, $z_0 = \Psi_{T \rightarrow 0}(z_T)$ .
$\pi$	map	Differentiable semantic projection (proxy).
$f: \mathcal{X} \rightarrow \mathbb{R}^D$	map	Differentiable feature extractor (e.g., CLIP/DINO/Inception).
$\text{Proj}_{\mathcal{M}}$	operator	Smooth local chart projection onto $\mathcal{M}$ (e.g., PCA/atlas chart).
$\pi(x) = \text{Proj}_{\mathcal{M}}(f(x))$	definition	Operational semantic identification model.
$\Phi = \pi \circ \Psi_{T \rightarrow 0}$	map	Semantic map from seeds to semantic manifold.
$\mathcal{Z}_{\text{reg}}$	set	Regular set where $\text{rank}(D\Phi_z) = k$ .
$\mathcal{F}_x = \Phi^{-1}(x)$	submanifold	Fiber (level set) of seeds mapping to the same semantics $x \in \mathcal{M}$ .
$d - k$	integer	Fiber dimension (semantic-invariant degrees of freedom).
$D\Phi_z$	linear map	Jacobian/derivative of $\Phi$ at seed $z$ .
$J_z$	matrix	Jacobian matrix of $\Phi$ in local coordinates, $J_z \in \mathbb{R}^{k \times d}$ .
$\text{rank}(\cdot)$	operator	Matrix rank.
$\text{Ker}(\cdot)$	operator	Kernel/null space.
$\text{Img}(\cdot)$	operator	Image/column space.
$\mathcal{V}_z = \text{Ker}(D\Phi_z)$	subspace	Vertical subspace (fiber tangent; semantically invariant directions).
$\mathcal{H}_z = \mathcal{V}_z^\perp$	subspace	Horizontal complement (semantically effective directions).
$g_{\mathcal{M}}$	metric	Riemannian metric on semantic manifold $\mathcal{M}$ .
$g_{\text{lat}} = \Phi^* g_{\mathcal{M}}$	(semi-)metric	Pullback semi-metric on $\mathcal{Z}$ induced by semantics.
$G_{\mathcal{M}}(\Phi(z))$	matrix	Local metric matrix of $g_{\mathcal{M}}$ at $\Phi(z)$ .
$G(z) = J_z^\top G_{\mathcal{M}}(\Phi(z)) J_z$	matrix	Pullback matrix representation of $g_{\text{lat}}$ at $z$ .
$\sigma_1(z) \geq \dots \geq \sigma_k(z) > 0$	scalars	Nonzero singular values of $D\Phi_z$ (restricted to horizontal directions).
$\kappa_{\text{eff}}(z) = \sigma_1(z)^2 / \sigma_k(z)^2$	scalar	Effective horizontal condition number.
$\ \cdot\ $	norm	Ambient Euclidean norm in $\mathbb{R}^d$ .
$\ \cdot\ _{g_{\text{lat}}}$	seminorm	(Semi-)norm induced by the pullback geometry.
$d_{\mathcal{M}}(\cdot, \cdot)$	distance	Geodesic (or chart-induced) distance on $\mathcal{M}$ .
$J_k(\Phi, z) = \prod_{i=1}^k \sigma_i(z)$	scalar	$k$ -Jacobian (volume expansion) of $\Phi$ at $z$ .
$\mathcal{H}^{d-k}$	measure	$(d - k)$ -dimensional Hausdorff measure on fibers.
$p_{\mathcal{Z}}(z)$	density	Density on $\mathcal{Z}$ (e.g., Gaussian prior).
$p_{\mathcal{M}}(x)$	density	Pushforward density on $\mathcal{M}$ via $x = \Phi(z)$ .
$\text{pdet}(\cdot)$	operator	Pseudodeterminant (product of nonzero eigenvalues).
$E_{\text{lat}}(z) = \frac{1}{2} \ z\ ^2 + \frac{1}{2} \log \text{pdet}(J_z J_z^\top)$	scalar	Local "compression energy" surrogate.
$n$	integer	NLN sample count for semantic erasure (noise aggregation).
$z^{(i)}$	vector	i.i.d. Gaussian seeds, $z^{(i)} \sim \mathcal{N}(0, I_d)$ .
$\bar{z}_T = \frac{1}{\sqrt{n}} \sum_{i=1}^n z^{(i)}$	vector	Aggregated seed (distribution-preserving), $\bar{z}_T \sim \mathcal{N}(0, I_d)$ .
$K$	integer	Number of probing timesteps for temporal aggregation (TPW).
$\{t_k\}_{k=1}^K$	scalars	Selected probing timesteps.
$\omega(t)$	function	Nonnegative weighting function over timesteps (design choice).
$w_k = \frac{\omega(t_k)}{\sum_{j=1}^K \omega(t_j)}$	scalars	Normalized timestep weights.
$\rho(t)$	function	Time-consistent rescaling mapping $\bar{z}_T$ to probe input at time $t$ .
$\sigma(t)$	function	Scheduler noise standard deviation (a typical choice for $\rho(t)$ in diffusion).
$\epsilon_\theta(z_t, t, \mathbf{y})$	vector	Model prediction (noise/score/velocity depending on backbone).
$\emptyset$	condition	Unconditional / negative prompt used in CFG.
$g_\theta(z_t, t, \mathbf{y}) = \epsilon_\theta(z_t, t, \mathbf{y}) - \epsilon_\theta(z_t, t, \emptyset)$	vector	CFG residual (prompt-induced direction).
$\mathbf{v}_{\text{agg}} = \frac{\sum_{k=1}^K w_k g_\theta(z_{t_k}, t_k, \mathbf{y})}{\sqrt{\sum_{k=1}^K w_k^2}}$	vector	Timestep-aggregated direction (TPW).
$\delta$	scalar	Injection strength (horizontal bias magnitude).
$\hat{z} = \bar{z}_T / \ \bar{z}_T\ $	vector	Unit-normalized seed direction.
$\hat{v} = \mathbf{v}_{\text{agg}} / \ \mathbf{v}_{\text{agg}}\ $	vector	Unit-normalized aggregated direction.
$\hat{v}_\perp = \hat{v} - (\hat{v}^\top \hat{z}) \hat{z}$	vector	Orthogonalized (tangent) injection direction before normalization.
$R = \ \bar{z}_T\ $	scalar	Seed radius (typical-set scale).
$z^* = R \cdot \frac{\bar{z}_T + \delta \hat{v}_\perp}{\ \bar{z}_T + \delta \hat{v}_\perp\ }$	vector	Injected seed with spherical retraction (radius preserved).
$M$	model	Pretrained diffusion/flow backbone used at inference.
$x_0$ (or $\mathbf{x}_0$ )	output	Final generated output/sample.
$\mathbb{E}[\cdot]$	operator	Expectation.

## C. Additional Proofs for Preliminaries and Method

### C.1. Proof of Theorem 3.4: Degenerate geometry

*Proof.* We expand every step carefully.

**Step 0: Set up the objects and identify tangent spaces.** Recall  $\mathcal{Z} \cong \mathbb{R}^d$  is an open subset of Euclidean space (the seed/latent space). Hence for any  $z \in \mathcal{Z}$ ,

$$T_z \mathcal{Z} \cong \mathbb{R}^d$$

canonically. The semantic manifold  $\mathcal{M}$  is a  $k$ -dimensional Riemannian manifold with metric  $g_{\mathcal{M}}$ , so for  $x = \Phi(z) \in \mathcal{M}$ , the metric  $g_{\mathcal{M}}(x)$  is a positive definite inner product on  $T_x \mathcal{M}$ .

The pullback (semi-)metric  $g_{\text{lat}} = \Phi^* g_{\mathcal{M}}$  is, by definition, the bilinear form on  $T_z \mathcal{Z}$ :

$$g_{\text{lat}}(z)(u, v) = g_{\mathcal{M}}(\Phi(z))(D\Phi_z(u), D\Phi_z(v)). \quad (37)$$

In particular,

$$\|u\|_{g_{\text{lat}}}^2 := g_{\text{lat}}(z)(u, u) = g_{\mathcal{M}}(\Phi(z))(D\Phi_z(u), D\Phi_z(u)) \geq 0,$$

so  $g_{\text{lat}}(z)$  is always positive semidefinite (never negative).

**Step 1: Vanishing on vertical directions.** By definition,

$$\mathcal{V}_z := \text{Ker}(D\Phi_z) = \{w \in T_z \mathcal{Z} : D\Phi_z(w) = 0\}.$$

For any  $w \in \mathcal{V}_z$ , we have  $D\Phi_z(w) = 0$ , and thus

$$\|w\|_{g_{\text{lat}}}^2 = g_{\mathcal{M}}(\Phi(z))(0, 0) = 0.$$

So  $g_{\text{lat}}(z)$  vanishes on  $\mathcal{V}_z$ .

**Step 2: The horizontal complement and injectivity of  $D\Phi_z$  on it.** Define the Euclidean-horizontal subspace

$$\mathcal{H}_z := \mathcal{V}_z^\perp,$$

where  $\perp$  is taken with respect to the standard Euclidean inner product  $\langle \cdot, \cdot \rangle$  on  $\mathbb{R}^d$ . We claim that the restriction  $D\Phi_z|_{\mathcal{H}_z}$  is injective when  $z \in \mathcal{Z}_{\text{reg}}$ .

Indeed, take any  $u \in \mathcal{H}_z$  and suppose  $D\Phi_z(u) = 0$ . Then  $u \in \text{Ker}(D\Phi_z) = \mathcal{V}_z$ . But also  $u \in \mathcal{H}_z = \mathcal{V}_z^\perp$ . Therefore

$$u \in \mathcal{V}_z \cap \mathcal{V}_z^\perp = \{0\},$$

so  $u = 0$ . This proves injectivity:

$$u \in \mathcal{H}_z, u \neq 0 \implies D\Phi_z(u) \neq 0.$$

**Step 3: Positive definiteness on  $\mathcal{H}_z$ .** Fix  $z \in \mathcal{Z}_{\text{reg}}$  and let  $u \in \mathcal{H}_z \setminus \{0\}$ . By Step 2,  $D\Phi_z(u) \neq 0 \in T_{\Phi(z)} \mathcal{M}$ . Since  $g_{\mathcal{M}}(\Phi(z))$  is a positive definite inner product on  $T_{\Phi(z)} \mathcal{M}$ , it follows that

$$\|u\|_{g_{\text{lat}}}^2 = g_{\mathcal{M}}(\Phi(z))(D\Phi_z(u), D\Phi_z(u)) > 0.$$

Hence  $g_{\text{lat}}(z)$  is positive definite on  $\mathcal{H}_z$ .

**Step 4: Coordinate/matrix characterization and  $\text{Ker}(G(z)) = \mathcal{V}_z$ .** Work in a local chart around  $x = \Phi(z)$ , identifying  $T_x \mathcal{M} \simeq \mathbb{R}^k$ . Let  $J_z \in \mathbb{R}^{k \times d}$  denote the Jacobian matrix of  $\Phi$  at  $z$  in this chart, and let  $G_{\mathcal{M}}(x) \in \mathbb{R}^{k \times k}$  be the symmetric positive definite matrix representing  $g_{\mathcal{M}}(x)$ . Then Definition 3.3 gives

$$G(z) = J_z^\top G_{\mathcal{M}}(x) J_z.$$

We show  $\text{Ker}(G(z)) = \text{Ker}(J_z)$ , which equals  $\text{Ker}(D\Phi_z) = \mathcal{V}_z$ .

Because  $G_{\mathcal{M}}(x) \succ 0$ , it has a (unique) symmetric square root  $G_{\mathcal{M}}(x)^{1/2} \succ 0$ . Define  $\tilde{J} := G_{\mathcal{M}}(x)^{1/2} J_z \in \mathbb{R}^{k \times d}$ . Then

$$G(z) = J_z^\top G_{\mathcal{M}}(x) J_z = J_z^\top G_{\mathcal{M}}(x)^{1/2} G_{\mathcal{M}}(x)^{1/2} J_z = \tilde{J}^\top \tilde{J}.$$

Now for any  $v \in \mathbb{R}^d$ ,

$$v^\top G(z) v = v^\top \tilde{J}^\top \tilde{J} v = \|\tilde{J} v\|^2 \geq 0.$$

Moreover,

$$G(z)v = 0 \implies v^\top G(z)v = 0 \implies \|\tilde{J}v\|^2 = 0 \implies \tilde{J}v = 0.$$

Since  $G_{\mathcal{M}}(x)^{1/2}$  is invertible,  $\tilde{J}v = 0$  is equivalent to  $J_z v = 0$ . Conversely,  $J_z v = 0$  clearly implies  $G(z)v = J_z^\top G_{\mathcal{M}}(x) J_z v = 0$ . Therefore

$$\text{Ker}(G(z)) = \text{Ker}(J_z) = \text{Ker}(D\Phi_z) = \mathcal{V}_z.$$

**Step 5: Rank statement.** Because  $G_{\mathcal{M}}(x)$  is invertible, multiplication by  $G_{\mathcal{M}}(x)^{1/2}$  does not change rank, so

$$\text{rank}(G(z)) = \text{rank}(\tilde{J}^\top \tilde{J}) = \text{rank}(\tilde{J}) = \text{rank}(J_z).$$

For  $z \in \mathcal{Z}_{\text{reg}}$ ,  $\text{rank}(D\Phi_z) = k$ , hence  $\text{rank}(J_z) = k$  and thus  $\text{rank}(G(z)) = k$ .

Combining Steps 1–5 yields exactly the statements in Theorem 3.4. □

## C.2. Proof of Lemma 3.6: Local semantic sensitivity

*Proof.* We work at a regular point  $z \in \mathcal{Z}$  of the semantic map  $\Phi : \mathcal{Z} \rightarrow \mathcal{M}$ . Let  $J_z := D\Phi(z)$  denote the Jacobian, and assume  $J$  is  $L$ -Lipschitz in a neighborhood of  $z$  (equivalently  $\|\nabla^2 \Phi\| \leq L$  locally). Let  $\mathcal{H}_z$  and  $\mathcal{V}_z$  be the horizontal and vertical subspaces induced by the degenerate pullback metric, so that  $\mathcal{V}_z = \ker(J_z)$  at a regular point. Write the perturbation as

$$\Delta z = \Delta z_{\mathcal{H}} + \Delta z_{\mathcal{V}}, \quad \Delta z_{\mathcal{H}} := \text{Proj}_{\mathcal{H}_z} \Delta z, \quad \Delta z_{\mathcal{V}} := \text{Proj}_{\mathcal{V}_z} \Delta z.$$

Denote by  $\sigma_1(z) \geq \dots \geq \sigma_k(z) > 0$  the nonzero singular values of  $J_z$  on  $\mathcal{H}_z$ .

**Step 1: Second-order Taylor expansion.** By twice differentiability and the Lipschitz Jacobian assumption, there exists a remainder term  $R(\Delta z)$  such that

$$\Phi(z + \Delta z) = \Phi(z) + J_z \Delta z + R(\Delta z), \quad \|R(\Delta z)\| \leq \frac{L}{2} \|\Delta z\|^2,$$

for all sufficiently small  $\|\Delta z\|$ .

**Step 2: Reduce  $J_z \Delta z$  to the horizontal component.** Since  $\Delta z_{\mathcal{V}} \in \ker(J_z)$ , we have

$$J_z \Delta z = J_z (\Delta z_{\mathcal{H}} + \Delta z_{\mathcal{V}}) = J_z \Delta z_{\mathcal{H}}.$$

**Step 3: Upper bound.** Using triangle inequality and Step 1–2,

$$\|\Phi(z + \Delta z) - \Phi(z)\| \leq \|J_z \Delta z_{\mathcal{H}}\| + \|R(\Delta z)\| \leq \sigma_1(z) \|\Delta z_{\mathcal{H}}\| + \frac{L}{2} \|\Delta z\|^2.$$

Up to chart constants converting ambient norm to  $d_{\mathcal{M}}(\cdot, \cdot)$  (absorbed into  $c_2, C$ ), this yields Eq. (10).

**Step 4: Refined lower bound (linear term minus quadratic remainder).** Again from Step 1–2,

$$\|\Phi(z + \Delta z) - \Phi(z)\| \geq \|J_z \Delta z_{\mathcal{H}}\| - \|R(\Delta z)\| \geq \sigma_k(z) \|\Delta z_{\mathcal{H}}\| - \frac{L}{2} \|\Delta z\|^2,$$

which gives Eq. (11) up to the same chart constants (absorbed into  $c_1, C$ ).

**Step 5: Cone condition implies a linear lower bound.** Assume the cone condition  $\|\Delta z_{\mathcal{H}}\| \geq \beta \|\Delta z\|$  for some  $\beta \in (0, 1]$ . If additionally  $\|\Delta z\| \leq \beta \sigma_k(z)/(2L)$ , then

$$\frac{L}{2} \|\Delta z\|^2 \leq \frac{L}{2} \|\Delta z\| \cdot \frac{1}{\beta} \|\Delta z_{\mathcal{H}}\| \leq \frac{1}{2} \sigma_k(z) \|\Delta z_{\mathcal{H}}\|.$$

Plugging this into Step 4 yields

$$\|\Phi(z + \Delta z) - \Phi(z)\| \geq \frac{1}{2} \sigma_k(z) \|\Delta z_{\mathcal{H}}\|.$$

Converting back to  $d_{\mathcal{M}}(\cdot, \cdot)$  (absorbing constants) gives Eq. (12). □

### C.3. Proof of Theorem 3.7: Coarea density transport

*Proof.* We derive the stated density formula directly from the coarea formula.

**Step 1: Coarea formula (statement).** Let  $\Phi : \mathbb{R}^d \rightarrow \mathbb{R}^k$  be locally Lipschitz with  $k \leq d$ . Denote by  $J_k(\Phi, z)$  the  $k$ -dimensional Jacobian (the product of the top  $k$  singular values of  $D\Phi_z$  on the regular set). The coarea formula states that for any nonnegative measurable function  $h$ ,

$$\int_{\mathbb{R}^d} h(z) J_k(\Phi, z) dz = \int_{\mathbb{R}^k} \left( \int_{\Phi^{-1}(x)} h(z) d\mathcal{H}^{d-k}(z) \right) dx, \quad (38)$$

where  $\mathcal{H}^{d-k}$  is  $(d - k)$ -dimensional Hausdorff measure on the level set  $\Phi^{-1}(x)$ .

In our setting  $\Phi : \mathcal{Z} \rightarrow \mathcal{M}$  maps into a manifold, but locally in a chart  $\varphi$  we can apply (38) to  $\tilde{\Phi} = \varphi \circ \Phi$ ; this yields the same expression up to chart Jacobian factors, which are absorbed into the density on  $\mathcal{M}$ . The theorem statement is the intrinsic version of this local expression.

**Step 1: Express the pushforward probability using an indicator.** Let  $Z \sim p_{\mathcal{Z}}$  with density w.r.t. Lebesgue measure on  $\mathcal{Z} \subset \mathbb{R}^d$ . Let  $X = \Phi(Z)$ . For any measurable set  $A \subset \mathcal{M}$ ,

$$\mathbb{P}(X \in A) = \mathbb{P}(\Phi(Z) \in A) = \int_{\mathcal{Z}} \mathbf{1}_A(\Phi(z)) p_{\mathcal{Z}}(z) dz. \quad (39)$$

**Step 2: Insert  $J_k(\Phi, z)$  and apply coarea.** Rewrite the integrand as

$$\mathbf{1}_A(\Phi(z)) p_{\mathcal{Z}}(z) = \left( \mathbf{1}_A(\Phi(z)) \frac{p_{\mathcal{Z}}(z)}{J_k(\Phi, z)} \right) J_k(\Phi, z),$$

on the regular set where  $J_k(\Phi, z) > 0$  (the singular set is negligible by Assumption 3.2). Define

$$h(z) := \mathbf{1}_A(\Phi(z)) \frac{p_{\mathcal{Z}}(z)}{J_k(\Phi, z)}.$$

Then (39) becomes

$$\mathbb{P}(X \in A) = \int_{\mathcal{Z}} h(z) J_k(\Phi, z) dz.$$

Applying the coarea formula (38) (in local coordinates) gives

$$\begin{aligned} \mathbb{P}(X \in A) &= \int_{\mathcal{M}} \left( \int_{\Phi^{-1}(x)} h(z) d\mathcal{H}^{d-k}(z) \right) d\mathcal{H}^k(x) \\ &= \int_{\mathcal{M}} \mathbf{1}_A(x) \left( \int_{\Phi^{-1}(x)} \frac{p_{\mathcal{Z}}(z)}{J_k(\Phi, z)} d\mathcal{H}^{d-k}(z) \right) d\mathcal{H}^k(x). \end{aligned} \quad (40)$$

**Step 3: Read off the density.** Since (40) holds for all measurable  $A$ , the term in parentheses must be the density  $p_{\mathcal{M}}(x)$  (w.r.t.  $k$ -dimensional Hausdorff/Riemannian volume measure on  $\mathcal{M}$ ):

$$p_{\mathcal{M}}(x) = \int_{\Phi^{-1}(x)} \frac{p_{\mathcal{Z}}(z)}{J_k(\Phi, z)} d\mathcal{H}^{d-k}(z),$$

which is exactly (14). □

#### C.4. Proof of Corollary 3.8: Local “compression energy” surrogate

*Proof.* Start from Theorem 3.7, which implies that along a fiber point  $z$  contributes to  $p_{\mathcal{M}}(x)$  with weight

$$\frac{p_{\mathcal{Z}}(z)}{J_k(\Phi, z)}.$$

Taking negative log yields a local “energy”:

$$-\log\left(\frac{p_{\mathcal{Z}}(z)}{J_k(\Phi, z)}\right) = -\log p_{\mathcal{Z}}(z) + \log J_k(\Phi, z).$$

**Gaussian prior term.** For  $p_{\mathcal{Z}}(z) = \mathcal{N}(0, I_d)$ ,

$$p_{\mathcal{Z}}(z) = (2\pi)^{-d/2} \exp\left(-\frac{1}{2}\|z\|^2\right),$$

so

$$-\log p_{\mathcal{Z}}(z) = \frac{1}{2}\|z\|^2 + \text{const.}$$

**Jacobian term and pseudodeterminant.** On the regular set  $\text{rank}(J_z) = k$ , the  $k$ -Jacobian satisfies

$$J_k(\Phi, z) = \prod_{i=1}^k \sigma_i(z),$$

where  $\{\sigma_i(z)\}_{i=1}^k$  are the nonzero singular values of  $J_z$  in local coordinates. Equivalently,

$$J_k(\Phi, z)^2 = \det(J_z J_z^\top).$$

Since  $J_z J_z^\top \in \mathbb{R}^{k \times k}$  is positive definite at regular points, its determinant equals the product of its (nonzero) eigenvalues; in invariant notation this is the pseudodeterminant  $\text{pdet}(J_z J_z^\top)$ , and here  $\text{pdet} = \det$ . Hence

$$\log J_k(\Phi, z) = \frac{1}{2} \log(J_k(\Phi, z)^2) = \frac{1}{2} \log \det(J_z J_z^\top) = \frac{1}{2} \log \text{pdet}(J_z J_z^\top).$$

Putting the two terms together yields

$$-\log\left(\frac{p_{\mathcal{Z}}(z)}{J_k(\Phi, z)}\right) = \frac{1}{2}\|z\|^2 + \frac{1}{2} \log \text{pdet}(J_z J_z^\top) + \text{const.},$$

which is exactly (15). □

#### C.5. Proof of Proposition 4.1

*Proof.* The sum  $\sum_{i=1}^n z_T^{(i)}$  is Gaussian with mean 0 and covariance  $nI_d$ . Scaling by  $1/\sqrt{n}$  yields covariance  $I_d$ , hence  $\bar{z}_T \sim \mathcal{N}(0, I_d)$ . □

### C.6. Proof of Lemma 4.2

*Proof.* **(1) Coarea representation.** By definition of  $\nu = \Phi_{\#}p_Z$ , for any measurable  $\varphi : \mathcal{M} \rightarrow \mathbb{R}$ ,

$$\mathbb{E}[\varphi(X)] = \int_{\mathcal{M}} \varphi(u) p_{\mathcal{M}}(u) d\mathcal{H}^k(u), \quad p_{\mathcal{M}} \text{ given by Theorem 3.7.}$$

Take  $\varphi(u) = d_{\mathcal{M}}(x, u)^2$  to obtain the first equality in Equation (19), and substitute Equation (14) to obtain the fiber integral form.

**(2) Replica averaging and the  $n^{-1/2}$  rate.** Let  $\mathcal{F}_n(x) = \frac{1}{n} \sum_{i=1}^n d_{\mathcal{M}}(x, X^{(i)})^2$ . Under the assumed local strong geodesic convexity around  $x^*$  and the uniqueness of  $\hat{x}_n$ , standard manifold LLN/argmin stability implies  $\hat{x}_n \rightarrow x^*$  in probability. Moreover, the strong convexity implies a quadratic growth condition  $\mathcal{F}(x) - \mathcal{F}(x^*) \gtrsim d_{\mathcal{M}}(x, x^*)^2$  locally, and empirical process concentration yields  $\sup_{x \in B(x^*, r)} |\mathcal{F}_n(x) - \mathcal{F}(x)| = O_{\mathbb{P}}(n^{-1/2})$ . Combining these two ingredients gives  $d_{\mathcal{M}}(\hat{x}_n, x^*) = O_{\mathbb{P}}(n^{-1/2})$ .  $\square$

### C.7. Proof of Lemma 4.4: Horizontality of the score proxy

*Proof.* Fix a point  $z$  and write  $J := D\Phi_z \in \mathbb{R}^{k \times d}$  in local coordinates (any chart around  $\Phi(z)$ ). The assumption states that the (guided) prediction can be written as

$$\epsilon_{\theta}(z, t, y) = J^{\top} \mathbf{v}$$

for some vector  $\mathbf{v} \in \mathbb{R}^k$  (semantic-feature space).

**Step 1: Identify the subspace where  $\epsilon_{\theta}$  lives.** By construction,  $J^{\top} \mathbf{v} \in \text{Im}(J^{\top})$ , i.e.,

$$\epsilon_{\theta}(z, t, y) \in \text{Im}(J^{\top}).$$

**Step 2: Fundamental theorem of linear algebra (orthogonal complement identity).** For any real matrix  $J$ , we have

$$\text{Im}(J^{\top}) = \text{Ker}(J)^{\perp},$$

where  $\perp$  is with respect to the standard Euclidean inner product in  $\mathbb{R}^d$ . A quick proof: (i) if  $u = J^{\top}v$ , then for any  $w \in \text{Ker}(J)$ ,  $\langle u, w \rangle = \langle J^{\top}v, w \rangle = \langle v, Jw \rangle = 0$ , so  $u \in \text{Ker}(J)^{\perp}$ ; (ii) dimensions match because  $\dim \text{Im}(J^{\top}) = \text{rank}(J) = d - \dim \text{Ker}(J) = \dim \text{Ker}(J)^{\perp}$ .

**Step 3: Connect to  $\mathcal{H}_z$ .** By definition  $\mathcal{V}_z = \text{Ker}(D\Phi_z) = \text{Ker}(J)$  and  $\mathcal{H}_z = \mathcal{V}_z^{\perp} = \text{Ker}(J)^{\perp}$ . Hence

$$\epsilon_{\theta}(z, t, y) \in \text{Im}(J^{\top}) = \text{Ker}(J)^{\perp} = \mathcal{H}_z,$$

which proves the lemma.  $\square$

### C.8. Proof of Proposition 4.5: Temporal aggregation reduces directional variance

*Proof.* Let  $g_k := \epsilon_{\theta}(\bar{z}_{t_k}, t_k, y) \in \mathbb{R}^d$  and assume

$$g_k = \mu_k + \xi_k, \quad \mathbb{E}[\xi_k] = 0.$$

Define the (unnormalized) weighted sum  $\tilde{v} := \sum_{k=1}^K w_k g_k$  and the normalized aggregate

$$v_{\text{agg}} := \frac{\tilde{v}}{\sqrt{\sum_{k=1}^K w_k^2}}.$$

**Step 1: Mean.**

$$\mathbb{E}[\tilde{v}] = \sum_{k=1}^K w_k \mathbb{E}[g_k] = \sum_{k=1}^K w_k \mu_k, \quad \mathbb{E}[v_{\text{agg}}] = \frac{\sum_k w_k \mu_k}{\sqrt{\sum_k w_k^2}}.$$

**Step 2: Covariance (general correlated case).** Let  $\Xi := (\xi_1, \dots, \xi_K)$  and denote cross-covariances  $\Sigma_{ij} := \text{Cov}(\xi_i, \xi_j)$  (each  $\Sigma_{ij}$  is  $d \times d$ ). Then

$$\text{Cov}(\tilde{v}) = \text{Cov}\left(\sum_{k=1}^K w_k \xi_k\right) = \sum_{i=1}^K \sum_{j=1}^K w_i w_j \Sigma_{ij}.$$

If the noises are independent,  $\Sigma_{ij} = 0$  for  $i \neq j$  and this simplifies to

$$\text{Cov}(\tilde{v}) = \sum_{k=1}^K w_k^2 \text{Cov}(\xi_k).$$

More generally, if correlations are “weak” in the sense that  $\|\Sigma_{ij}\|$  is small for  $i \neq j$ , then the diagonal term still dominates and the same scaling intuition holds.

**Step 3: Effective sample size scaling.** Assume for simplicity that  $\text{Cov}(\xi_k) = \Sigma$  is approximately constant across  $k$  and cross-covariances are negligible. Then

$$\text{Cov}(\tilde{v}) \approx \left(\sum_{k=1}^K w_k^2\right) \Sigma, \quad \text{Cov}(v_{\text{agg}}) = \frac{\text{Cov}(\tilde{v})}{\sum_{k=1}^K w_k^2} \approx \Sigma.$$

In other words, the normalization removes the trivial scaling of weights; what improves is the *directional concentration* of  $\tilde{v}$  around its mean when  $\sum_k w_k^2$  is small relative to  $(\sum_k w_k)^2$  (many effectively averaged terms). A common summary is the effective sample size

$$N_{\text{eff}} := \frac{(\sum_{k=1}^K w_k)^2}{\sum_{k=1}^K w_k^2}.$$

For normalized weights with  $\sum_k w_k = 1$ , this becomes

$$N_{\text{eff}} = \frac{1}{\sum_k w_k^2}.$$

Thus, as the weights spread over more timesteps (larger  $N_{\text{eff}}$ ), the aggregate direction concentrates more tightly around the weighted mean direction, matching the proposition statement.  $\square$

### C.9. Proof of Proposition 4.6: Retraction as projection onto the sphere

*Proof.* Let  $R := \|\bar{z}_T\|$  and  $u := \bar{z}_T + \delta \hat{v}$ . We need to solve

$$\min_{z \in \mathbb{R}^d} \|z - u\|^2 \quad \text{s.t.} \quad \|z\| = R.$$

**Method 1: Geometry (maximize inner product).** Expand:

$$\|z - u\|^2 = \|z\|^2 + \|u\|^2 - 2\langle z, u \rangle = R^2 + \|u\|^2 - 2\langle z, u \rangle.$$

Since  $R^2 + \|u\|^2$  is constant under the constraint, minimizing  $\|z - u\|^2$  is equivalent to maximizing  $\langle z, u \rangle$  subject to  $\|z\| = R$ . By Cauchy–Schwarz,  $\langle z, u \rangle \leq \|z\| \|u\| = R \|u\|$ , with equality iff  $z$  is a positive scalar multiple of  $u$ . Thus the maximizer is

$$z^* = R \frac{u}{\|u\|} = \|\bar{z}_T\| \cdot \frac{\bar{z}_T + \delta \hat{v}}{\|\bar{z}_T + \delta \hat{v}\|},$$

which is exactly (26).

**Method 2: Lagrange multipliers (for completeness).** Consider  $\mathcal{L}(z, \lambda) = \|z - u\|^2 + \lambda(\|z\|^2 - R^2)$ . Stationarity in  $z$  gives  $2(z - u) + 2\lambda z = 0$ , i.e.  $(1 + \lambda)z = u$ . Thus  $z = \frac{1}{1+\lambda}u$ . Enforce  $\|z\| = R$  to get  $|1 + \lambda| = \|u\|/R$  and choose the sign giving the minimizer (same direction as  $u$ ), yielding  $z^* = Ru/\|u\|$ .  $\square$

### C.10. Proof of Lemma 4.7: Small- $\delta$ regime and controlled shift

*Proof.* Let  $R = \|\bar{z}_T\|$  and  $u = \bar{z}_T + \delta\hat{v}$ , so  $z^* = Ru/\|u\|$ .

(1) **Exact radius preservation.** By construction,

$$\|z^*\| = \left\| R \frac{u}{\|u\|} \right\| = R = \|\bar{z}_T\|.$$

So there is *zero* radius drift.

(2) **First-order change is  $O(\delta)$ .** We bound  $\|z^* - \bar{z}_T\|$ . Write

$$z^* - \bar{z}_T = R \frac{\bar{z}_T + \delta\hat{v}}{\|\bar{z}_T + \delta\hat{v}\|} - \bar{z}_T.$$

Use the identity

$$\frac{1}{\|\bar{z}_T + \delta\hat{v}\|} = \frac{1}{R} \cdot \frac{1}{\left\| \frac{\bar{z}_T}{R} + \frac{\delta}{R}\hat{v} \right\|}.$$

Since  $\left\| \frac{\bar{z}_T}{R} \right\| = 1$  and  $\delta/R \ll 1$ , we have

$$\left\| \frac{\bar{z}_T}{R} + \frac{\delta}{R}\hat{v} \right\| = 1 + O(\delta/R) \quad \Rightarrow \quad \frac{1}{\|\bar{z}_T + \delta\hat{v}\|} = \frac{1}{R} (1 + O(\delta/R)).$$

Therefore,

$$z^* = R(\bar{z}_T + \delta\hat{v}) \cdot \frac{1}{\|\bar{z}_T + \delta\hat{v}\|} = (\bar{z}_T + \delta\hat{v})(1 + O(\delta/R)) = \bar{z}_T + \delta\hat{v} + O(\delta^2/R).$$

Hence

$$\|z^* - \bar{z}_T\| \leq \delta\|\hat{v}\| + O(\delta^2/R) = O(\delta),$$

as claimed. □

**Remark on cross terms and orthogonalization.** If the injected direction  $\hat{v}$  has a nonzero component along  $\bar{z}_T$ , the norm  $\|\bar{z}_T + \delta\hat{v}\|$  contains a first-order cross term of size  $O(\delta)$ . In our implementation (Algorithm 1), we *recommend* orthogonalizing  $\hat{v}$  w.r.t.  $\bar{z}_T$ , in which case the cross term vanishes and the norm expansion becomes  $\|\bar{z}_T + \delta\hat{v}\| = \|\bar{z}_T\| \sqrt{1 + (\delta/\|\bar{z}_T\|)^2} = \|\bar{z}_T\| + O(\delta^2/\|\bar{z}_T\|)$ . This justifies the higher-order remainder used below under the recommended orthogonalization.

### C.11. Additional discussion for NLN

**NLN as an induced-marginal operation (what is preserved and what is not).** Equivalently, NLN is an orthogonal projection in an enlarged Gaussian space followed by marginalization: the ‘‘consensus coordinate’’  $\bar{z}_T$  is kept while  $(n-1)$  orthogonal ‘‘disagreement coordinates’’ are integrated out. Hence, for any *fixed* measurable set  $A \subset \mathcal{Z}$ ,  $\mathbb{P}(\bar{z}_T \in A) = \mathbb{P}(z_T \in A)$ , so NLN alone cannot increase the mass of any fixed region in  $\mathcal{Z}$ . The point is that practical pipelines rarely depend on  $z_T$  only through such fixed sets; they depend on  $z_T$  through *model-coupled functionals* (scores, velocities, prompt-conditional guidance, etc.), which implicitly define *new induced distributions* on  $\mathcal{Z}$ .

**Why NLN can help: changing the *model-induced* distribution rather than the prior.** Let  $S(z)$  denote any model-dependent stability/quality proxy used downstream (e.g., early-step score/velocity norms, small-step sensitivity estimates, or a reward signal). The actual seed utilized by a pipeline is often drawn from an induced distribution of the form

$$p_{\text{use}}(z) \propto p_{\mathcal{Z}}(z) W(S(z)),$$

where  $W$  is an acceptance rule (screening) or a soft tilt (reweighting). Although NLN preserves  $p_{\mathcal{Z}}$  at the marginal level, it changes how  $S(\cdot)$  behaves statistically by *averaging out nuisance microstates* before  $S$  is queried. In other words, NLN does not move probability mass in  $\mathcal{Z}$  *a priori*; it reshapes the *pushforward* of the prior through the model-coupled map  $z \mapsto S(z)$ , and therefore can change  $p_{\text{use}}$  once screening/tilting (explicit or implicit) is applied.

**Interpretation as marginalizing nuisance microstates on fibers.** Under the submersion viewpoint  $\Phi = \pi \circ \Psi$ , each seed  $z_T$  decomposes locally into a semantic (horizontal) component and a nuisance (vertical) microstate along fibers. NLN replaces one specific microstate with a consensus coordinate obtained by marginalizing  $n - 1$  independent microstates. Proposition quantifies this as a de-identification effect: for any particular constituent seed, the mutual information between its vertical block and the aggregate decays as  $O(1/n)$ . Geometrically, this reduces the chance that subsequent guidance/injection is dominated by an unlucky vertical configuration, making the downstream model-coupled functional  $S(z)$  (and thus the induced  $p_{\text{use}}$ ) less brittle.

**Caveat: screening vs. reweighting (two different induced distributions).** If NLN uses data-dependent weights  $\alpha_i = \alpha(z^{(i)})$  prior to aggregation, the resulting  $\bar{z}_T$  is no longer exactly  $\mathcal{N}(0, I_d)$ , corresponding to an explicit distribution tilt. This can be desirable but should be treated as an intentional distribution shift. A distribution-preserving alternative is *screening*: sample a pool of prior-valid candidates and select by a proxy. This keeps the final seed as an actual prior draw, while changing the induced *accepted* distribution through the acceptance rule. Both mechanisms are best understood as operating on the model-induced map  $z \mapsto S(z)$  rather than contradicting the marginal preservation  $\bar{z}_T \stackrel{d}{=} z_T$ .

## D. Overall Pipeline

The overall pipeline of our method is summarized in Algorithm 1.

---

### Algorithm 1 Semantic Erasure and Injection

---

**Require:** Text prompt  $\mathbf{y}$ , pretrained diffusion/flow model  $M$ , hyperparameters  $\{n, K, \delta, f(\cdot)\}$ , time-rescale  $\rho(\cdot)$

**Ensure:** Generated output  $x_0$

- 1: **Stage 1: Semantic Erasure (NLN)**
  - 2: Sample  $n$  independent noise:  $\{\mathbf{z}_1, \dots, \mathbf{z}_n\} \sim \mathcal{N}(0, I)$
  - 3: Compute purified noise:  $\mathbf{z}_T = \frac{1}{\sqrt{n}} \sum_{i=1}^n \mathbf{z}_i$
  - 4: **Stage 2: Semantic Residual Aggregation (TPW)**
  - 5: Select  $K$  key timesteps:  $\{t_1, t_2, \dots, t_K\}$
  - 6: Initialize  $g_{\text{sum}} \leftarrow 0, v_{\text{sum}} \leftarrow 0$
  - 7: **for**  $k = 1$  to  $K$  **do**
  - 8:   Compute weight:  $w_k = \frac{f(t_k)}{\sum_{j=1}^K f(t_j)}$
  - 9:   Time-consistent probe input:  $\mathbf{z}_{t_k} \leftarrow \rho(t_k) \mathbf{z}_T$
  - 10:   **if** is Diffusion model **then**
  - 11:     Predict conditional:  $\epsilon_k^c = M(\mathbf{z}_{t_k}, t_k, \mathbf{y})$
  - 12:     Predict unconditional:  $\epsilon_k^u = M(\mathbf{z}_{t_k}, t_k)$
  - 13:     Residual:  $g_k \leftarrow \epsilon_k^c - \epsilon_k^u$
  - 14:     Update  $g_{\text{sum}} \leftarrow g_{\text{sum}} + w_k \cdot g_k$
  - 15:   **else**
  - 16:     Predict conditional:  $v_k^c = M(\mathbf{z}_{t_k}, t_k, \mathbf{y})$
  - 17:     Predict unconditional:  $v_k^u = M(\mathbf{z}_{t_k}, t_k)$
  - 18:     Residual:  $r_k \leftarrow v_k^c - v_k^u$
  - 19:     Update  $v_{\text{sum}} \leftarrow v_{\text{sum}} + w_k \cdot r_k$
  - 20:   **end if**
  - 21: **end for**
  - 22: **Stage 3: Horizontal Injection + Retraction**
  - 23: **if** is Diffusion model **then**
  - 24:   Normalize:  $g_{\text{agg}} \leftarrow \frac{g_{\text{sum}}}{\sqrt{\sum_{k=1}^K w_k^2}}$
  - 25:   (Optional) Orthogonalize:  $g_{\text{agg}} \leftarrow g_{\text{agg}} - \frac{\langle g_{\text{agg}}, \mathbf{z}_T \rangle}{\|\mathbf{z}_T\|^2} \mathbf{z}_T$
  - 26:   Unit direction:  $\hat{\mathbf{v}} \leftarrow g_{\text{agg}} / \|g_{\text{agg}}\|$
  - 27:   Retract:  $\mathbf{z}^* \leftarrow \|\mathbf{z}_T\| \cdot \frac{\mathbf{z}_T + \delta \hat{\mathbf{v}}}{\|\mathbf{z}_T + \delta \hat{\mathbf{v}}\|}$
  - 28:   Set initial noise:  $\epsilon_{\text{adj}} \leftarrow \mathbf{z}^*$
  - 29: **else**
  - 30:   Unit direction:  $\hat{\mathbf{v}} \leftarrow v_{\text{sum}} / \|v_{\text{sum}}\|$
  - 31:   Retract:  $\mathbf{z}^* \leftarrow \|\mathbf{z}_T\| \cdot \frac{\mathbf{z}_T + \delta \hat{\mathbf{v}}}{\|\mathbf{z}_T + \delta \hat{\mathbf{v}}\|}$
  - 32:   Set initial noise:  $\epsilon_{\text{adj}} \leftarrow \mathbf{z}^*$
  - 33: **end if**
  - 34: **Stage 4: Final Generation**
  - 35: Run standard generation with  $\epsilon_{\text{adj}}$  as initial noise to get  $x_0$
  - 36: **return**
-

Table 6. Recommended hyperparameters for Algorithm 1.

Hyperparam	Rec.	Range	Notes / tuning tips
$n$ (NLN)	6400	1600 ~ 12800	Larger $n$ yields more stable $\mathbf{z}_T$ (stronger erasure) at higher compute.
$K$ $\{t_k\}$	1 ~ 4 task-dep.	1 ~ 8 diversified	More probes $\Rightarrow$ richer semantics. Smaller $t$ : cleaner subject. Larger $t$ : richer global composition.
$\delta$ $f(t)$	5 ~ 6 uniform/task-dep.	0 ~ 15 $\rho(t)^\alpha$	Stronger injection Match $\{t_k\}$ : smaller $t$ flatter; larger $t$ emphasize composition.
$\rho(t)$ Orthogonalize	model-native on	model-dep. on/off	Use native schedule for time-consistent probing. Decouple from $\mathbf{z}_T$ ; turn off if effect weakens.
Normalize	on	on/off	Stabilizes across $K$ and weighting.

## E. Additional Experiments: Visualizing Degenerate Latent Geometry

This appendix provides a detailed methodology and analysis for visualizing the *degenerate* pullback geometry induced by the semantic map  $\Phi = \pi \circ \Psi$  (Sec. 3). Our theory predicts that the pullback semi-metric  $g_{\text{lat}} = \Phi^* g_{\mathcal{M}}$  vanishes along semantic-invariant fiber (vertical) directions and concentrates on a low-dimensional horizontal subspace (Theorem 3.4). Empirically, this should manifest as: (i) strong anisotropy of semantic sensitivity across latent directions, (ii) an effectively low-rank local spectrum (spectral gap), and (iii) substantially faster semantic change along a horizontal-proxy direction than along a control direction.

### E.1. Experimental Setup and Notation

**Backbone and sampler.** We use FLUX.1-Dev with the official inference configuration described in Appendix G (resolution, steps, CFG/true-CFG, etc.). All probes below modify *only the initial seed* while keeping the sampler and prompt fixed.

**Prompts and seeds.** We evaluate on a set of complex prompts (multi-object, typography, spatial relations), and sample multiple random seeds per prompt. Unless noted otherwise, reported curves/distributions aggregate over prompts and seeds, while strip visualizations show representative examples.

**Semantic features and metrics.** Let  $x(z_T)$  denote the generated image/video-frame render from initial noise  $z_T$  under a fixed prompt  $y$ . We define:

- **Alignment score (CLIPSim).** Let  $e_I(x) \in \mathbb{R}^D$  and  $e_T(y) \in \mathbb{R}^D$  be CLIP image/text embeddings, and  $\hat{e}_I = e_I/\|e_I\|$ ,  $\hat{e}_T = e_T/\|e_T\|$ . Then

$$\text{CLIPSim}(x, y) = \langle \hat{e}_I(x), \hat{e}_T(y) \rangle. \quad (41)$$

- **Semantic displacement ( $\|\Delta\text{CLIP}\|$ ).** For a baseline seed  $z_T$  and a perturbed seed  $z'_T$ , define

$$\|\Delta\text{CLIP}\| := \|\hat{e}_I(x(z'_T)) - \hat{e}_I(x(z_T))\|_2. \quad (42)$$

This measures how much the *semantic representation* changes under seed perturbation, independent of prompt alignment.

### E.2. Typical-Radius Shell Probing via Spherical Geodesics

A central goal is to probe sensitivity *without leaving the prior typical set*. For high-dimensional Gaussian  $z_T \sim \mathcal{N}(0, I_d)$ , the norm concentrates near  $\|z_T\| \approx \sqrt{d}$ . Thus we restrict perturbations to the sphere of radius  $R = \|z_T\|$ .

**Tangent directions.** Let  $\hat{z} = z_T/\|z_T\|$ . We sample a direction  $u \sim \mathcal{N}(0, I_d)$  and project to the tangent space at  $z_T$ :

$$\tilde{u} := u - \langle u, \hat{z} \rangle \hat{z}, \quad \hat{u} := \tilde{u}/\|\tilde{u}\|. \quad (43)$$

Then  $\hat{u} \perp \hat{z}$  and  $\hat{u}$  is (approximately) uniform on the tangent unit sphere.

**Spherical geodesic (exact radius preservation).** For an angle  $\theta \in [0, \pi]$ , the great-circle geodesic perturbation is

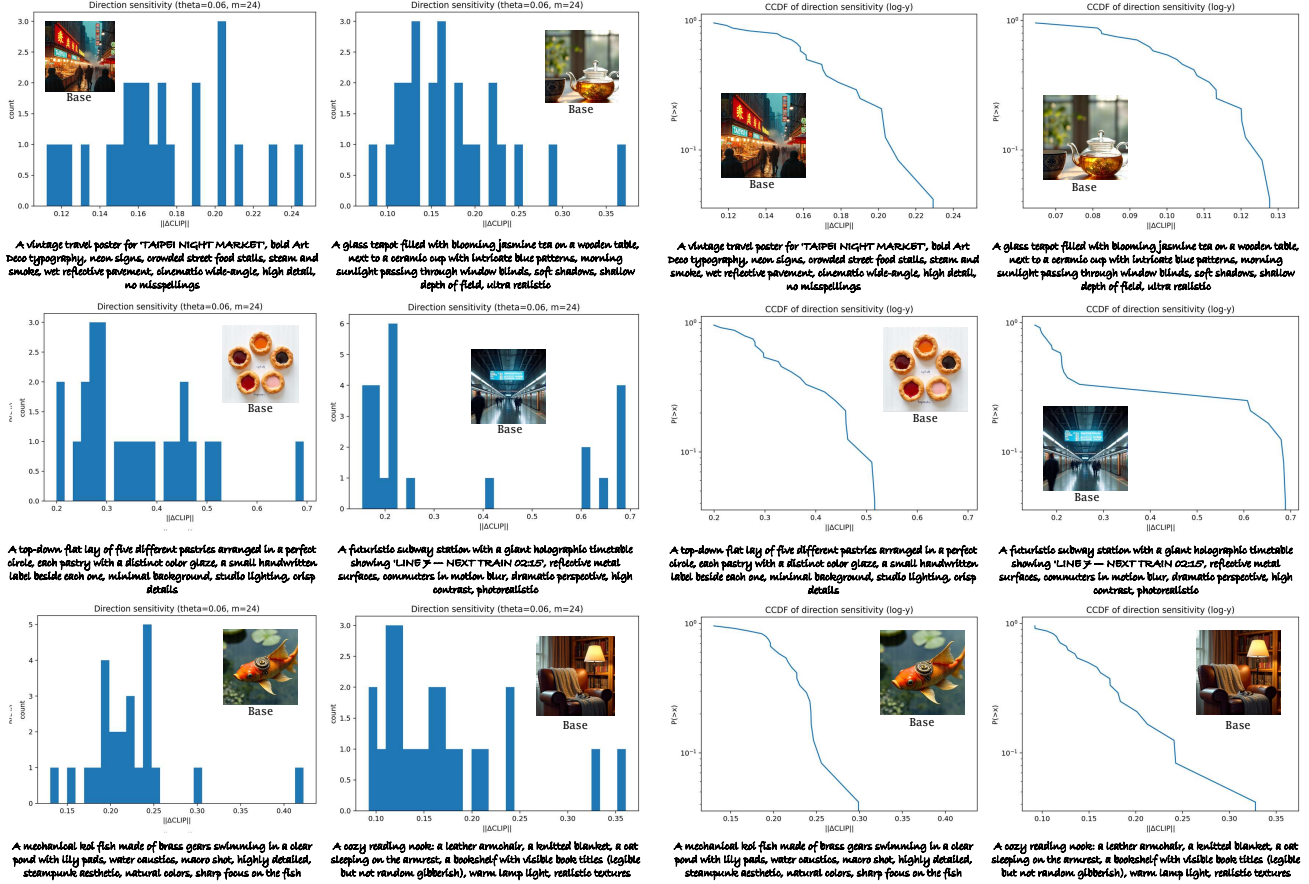
$$z_T(\theta) = R(\cos \theta \hat{z} + \sin \theta \hat{u}), \quad (44)$$

which satisfies  $\|z_T(\theta)\| = R$  *exactly* for all  $\theta$ .

**Connection to “inject + retract”.** Eq. (44) is equivalent (up to small-angle approximation) to taking a step in a tangent direction and retracting back onto the sphere:

$$z'_T = R \cdot \frac{z_T + \delta \hat{u}}{\|z_T + \delta \hat{u}\|}. \quad (45)$$

Indeed for small  $\delta/R$ , the geodesic angle obeys  $\theta \approx \delta/R$ . This mirrors the retraction used in our method (Proposition 4.6, Lemma 4.7) and ensures that measured effects are not artifacts of distribution shift.



(a) Histogram of  $\|\Delta\text{CLIP}\|$  over random tangent directions at a small angle  $\theta_0$ .

(b) CCDF  $\mathbb{P}(\|\Delta\text{CLIP}\| \geq t)$  emphasizing the tail probability of large semantic changes.

Figure 13. Anisotropic semantic sensitivity under an isotropic prior. Most tangent directions are semantically silent (near-zero displacement), while a small fraction produces large semantic changes, consistent with a degenerate pullback semi-metric that vanishes along fiber (vertical) directions and concentrates on a few horizontal modes.

### E.3. Direction Sensitivity Distribution: Histogram and CCDF

**Procedure.** For each prompt  $y$  and baseline seed  $z_T$ : (i) sample  $M$  random tangent directions  $\{\hat{u}_j\}_{j=1}^M$  using Eq. (43); (ii) choose a small probing angle  $\theta_0$  (e.g.,  $\theta_0 \in [0.02, 0.08]$  radians); (iii) generate  $x(z_T)$  and  $x(z_T(\theta_0; \hat{u}_j))$  for each  $j$ , and compute  $\|\Delta\text{CLIP}\|$  via Eq. (42). We then aggregate  $\|\Delta\text{CLIP}\|$  over seeds/prompts and visualize:

- **Histogram** of  $\|\Delta\text{CLIP}\|$  across random directions;
- **CCDF** (complementary CDF),  $\mathbb{P}(\|\Delta\text{CLIP}\| \geq t)$ , highlighting tail behavior.

**Why this diagnoses degeneracy.** For sufficiently small  $\theta_0$ , and assuming local regularity,  $\Phi$  admits a first-order approximation along tangent directions:

$$\Phi(z_T(\theta_0)) - \Phi(z_T) \approx D\Phi_{z_T}(R\theta_0 \hat{u}). \tag{46}$$

Thus the distribution of semantic displacement across random  $\hat{u}$  reflects the anisotropy of  $D\Phi_{z_T}$  restricted to horizontal directions (Lemma 3.6): most directions close to the (near-)vertical fiber yield small displacement, while directions aligned with strong horizontal modes yield large displacement.

**How to read Fig. 13.** The key signature is a *heavy-tailed* sensitivity distribution: a large mass near zero (many semantically-invariant directions), and a slowly decaying CCDF tail (rare but strong semantic directions). This directly supports the

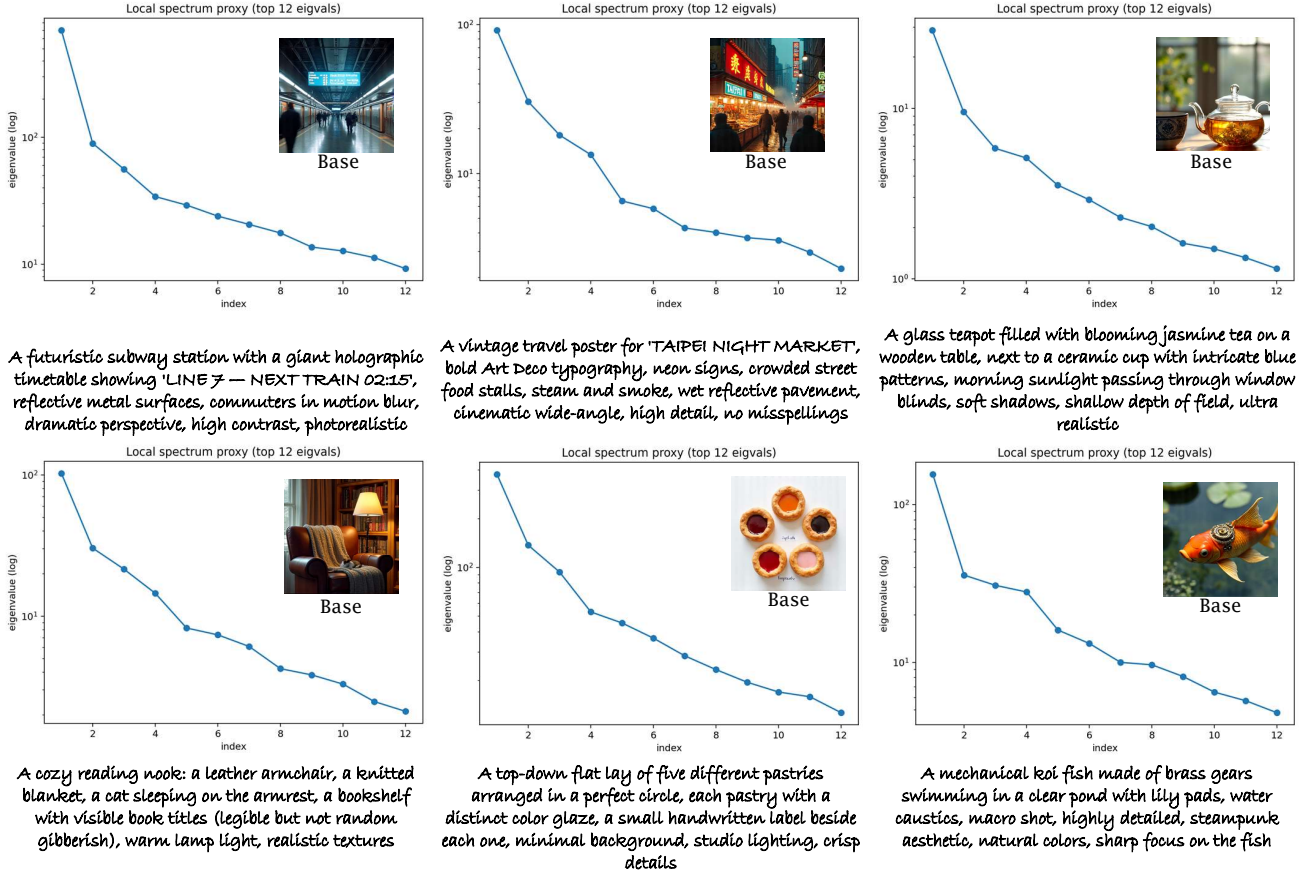


Figure 14. **Local spectrum proxy.** A pronounced spectral gap indicates that only a few directions dominate semantic sensitivity, consistent with effective low-rank horizontal structure.

“seed lottery” mechanism: even with  $\|z_T\|$  fixed (same prior energy), seeds differ by how much mass they place on strong horizontal directions.

#### E.4. Local Spectrum Estimation: Evidence of Effective Low Rank

We further estimate an *effective local spectrum* that summarizes how many horizontal degrees of freedom dominate semantic change.

**Finite-difference directional derivatives in feature space.** Let  $\phi(z_T) := \hat{e}_I(x(z_T)) \in \mathbb{R}^D$  be the normalized CLIP image embedding of the generated output. For each random tangent direction  $\hat{u}_j$ , we compute a feature-space directional derivative via a symmetric geodesic difference:

$$g_j := \frac{\phi(z_T(\theta_0; \hat{u}_j)) - \phi(z_T(-\theta_0; \hat{u}_j))}{2\theta_0} \in \mathbb{R}^D. \tag{47}$$

When  $\theta_0$  is small,  $g_j$  approximates the Jacobian action (chain rule through generation + CLIP features) restricted to the tangent direction  $\hat{u}_j$ .

**Randomized spectrum proxy.** Stack  $g_j$  as columns of  $G = [g_1, \dots, g_M] \in \mathbb{R}^{D \times M}$ . Then the Gram matrix  $G^T G \in \mathbb{R}^{M \times M}$  captures correlations of directional derivatives. The non-zero singular values of  $G$  (equivalently eigenvalues of  $G^T G$ ) provide a randomized estimate of dominant modes. We plot the sorted eigenvalues (or singular values) as an *effective local spectrum*.

**How to read Fig. 14.** A sharp drop after the first few components indicates that semantic changes concentrate on a low-dimensional subspace (consistent with  $\text{rank}(D\Phi) = k \ll d$  in Assumption 3.2). Moreover, different prompts can exhibit different spectral shapes: typography- and layout-heavy prompts typically display a more pronounced head (stronger dominant modes), suggesting that the horizontal sensitivity directions depend on conditioning.

### E.5. Horizontal-Proxy vs. Control Directions

The theory predicts that moving along horizontal directions changes semantics more efficiently than moving along vertical directions. Since  $D\Phi$  is intractable, we construct a *horizontal proxy* direction from the model itself.

**Horizontal-proxy direction (TPW residual).** Following Sec. 4.3, we compute a prompt-conditioned residual at a probing timestep  $t$ :

$$r := \epsilon_\theta(z_t, t, y) - \epsilon_\theta(z_t, t, \emptyset), \tag{48}$$

and normalize it to obtain  $\hat{r} = r/\|r\|$ . To ensure comparability on the typical-radius shell, we project  $\hat{r}$  to the tangent space at  $z_T$ :

$$\hat{u}_H := \frac{\hat{r} - \langle \hat{r}, \hat{z} \rangle \hat{z}}{\|\hat{r} - \langle \hat{r}, \hat{z} \rangle \hat{z}\|}. \tag{49}$$

By Lemma 4.4, such model-derived residuals lie in (or near) the horizontal complement of  $\text{Ker}(D\Phi)$ , making  $\hat{u}_H$  a practical horizontal proxy.

**Control direction.** We sample an independent random tangent direction  $\hat{u}_C$  using Eq. (43). This provides a baseline for typical (mostly semantically-silent) directions.

### E.6. Geodesic Curves: Semantic Displacement and Alignment vs. Angle

**Procedure.** For each  $(y, z_T)$ , we generate a grid of angles  $\theta \in \{\theta_1, \dots, \theta_L\}$  and evaluate  $x(z_T(\theta; \hat{u}_H))$  and  $x(z_T(\theta; \hat{u}_C))$ . We report: (i)  $\|\Delta\text{CLIP}\|(\theta)$  measuring semantic displacement from the baseline seed, and (ii)  $\text{CLIPSim}(\theta)$  measuring prompt alignment.

**How to read Fig. 15.** **Early-slope gap** is the main signature: if  $\|\Delta\text{CLIP}\|$  increases much faster along  $\hat{u}_H$  than  $\hat{u}_C$ , then the proxy direction aligns with strong horizontal sensitivity modes. Meanwhile,  $\text{CLIPSim}$  often exhibits a *sweet spot* at moderate  $\theta$ : alignment increases as we move along a prompt-relevant horizontal direction, but may decrease at larger angles due to crossing semantic basins or inducing artifacts (non-linear regime). This matches our empirical observation that overly strong injection  $\delta$  can degrade quality, and supports the need for retraction and moderate-strength shaping.

### E.7. Strip Visualizations: Qualitative Evidence on the Typical-Radius Shell

To provide an intuitive view, we visualize *strips* of generations along increasing  $\theta$ . Each column corresponds to one  $\theta$  on the geodesic (Eq. 44), with the baseline at  $\theta = 0$ .

**How to read Fig. 16.** Compare columns at the same  $\theta$  between control vs. horizontal: horizontal-proxy strips tend to exhibit earlier emergence of structured prompt attributes (e.g., typography/layout, object relations, salient attributes), while control strips often remain near a “plateau” of minor appearance drift before occasionally undergoing abrupt changes at larger  $\theta$ . This visual pattern matches the curve behavior in Fig. 15: control directions often stay near semantically-invariant fibers locally, while horizontal directions traverse semantically-sensitive modes.

### E.8. Summary: What These Visualizations Establish

Taken together: (i) the heavy-tailed direction sensitivity distribution (Fig. 13), (ii) the pronounced spectral gap in the local spectrum proxy (Fig. 14), and (iii) the strong early-slope advantage of horizontal-proxy geodesic curves plus strip evidence (Figs. 15–16) provide a consistent empirical picture: *under an isotropic Gaussian prior, semantic sensitivity is highly anisotropic and effectively low-rank*, supporting our degenerate pullback geometry viewpoint and motivating horizontal seed shaping in Sec. 4.

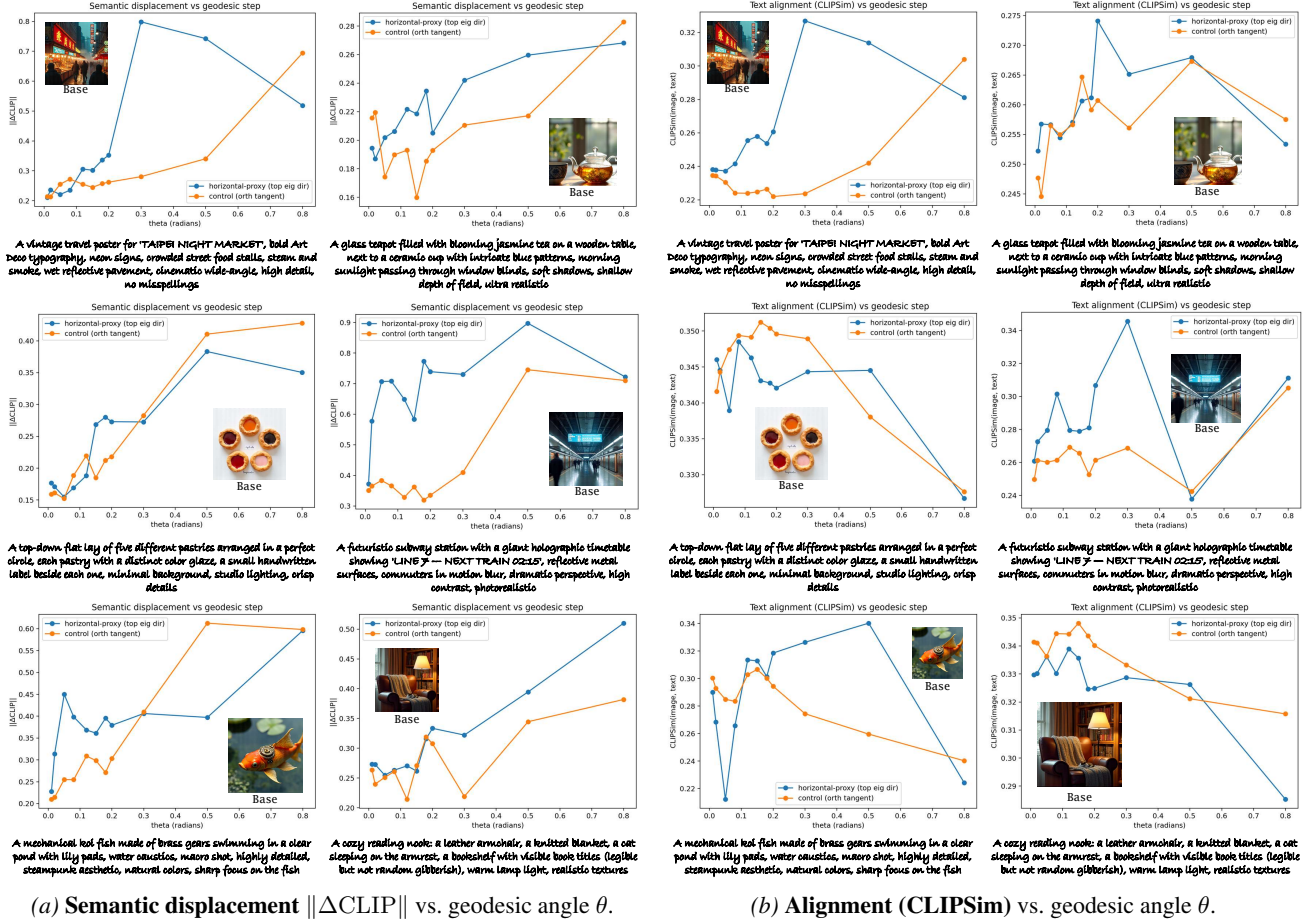


Figure 15. **Horizontal-proxy vs. control perturbations.** Horizontal-proxy directions typically yield faster semantic displacement and often higher alignment at moderate angles. At large angles, non-linear overshoot may reduce alignment, motivating controlled injection strength in Sec. 4.4.

### E.9. Diagnostic Evaluation of Geometric Assumptions

This appendix provides diagnostics that make the geometric assumptions in the main text empirically testable. We operationalize the semantics map  $\pi$  using an evaluator-defined representation (CLIP), and measure local non-degeneracy of  $\pi \circ G$  around the initial noise. We then relate these diagnostics to the prompt-level improvement of our method over a baseline.

#### E.9.1. SETUP

We evaluate on  $N = 200$  prompts. For each prompt, we generate one baseline image and one image with our method under matched settings. We measure text-image alignment using CLIPScore, and report the prompt-level improvement

$$\Delta = \text{CLIPScore(ours)} - \text{CLIPScore(baseline)}. \tag{50}$$

Unless stated otherwise, we report a bootstrap 95% confidence interval (2,000 resamples) over prompts. We also report the prompt-level win rate (fraction of prompts with  $\Delta > 0$ ) and Cohen’s  $d$  computed on paired prompt-level differences.

#### E.9.2. MEASURING “APPROXIMATE SUBMERSION” VIA LOCAL JACOBIAN SPECTRUM

The main text assumes  $\pi \circ G$  behaves like an approximate submersion on a dense regular set, which informally means the semantic mapping does not locally collapse. To test this, we approximate the Jacobian of  $\pi \circ G$  in a local neighborhood of



A vintage travel poster for TAIPEI NIGHT MARKET, bold Art Deco typography, neon signs, crowded street food stalls, steam and smoke, wet reflective pavement, cinematic wide-angle, high detail, no misspellings



A vintage travel poster for TAIPEI NIGHT MARKET, bold Art Deco typography, neon signs, crowded street food stalls, steam and smoke, wet reflective pavement, cinematic wide-angle, high detail, no misspellings



A glass teapot filled with blooming jasmine tea on a wooden table, next to a ceramic cup with intricate blue patterns, morning sunlight passing through window blinds, soft shadows, shallow depth of field, ultra realistic



A glass teapot filled with blooming jasmine tea on a wooden table, next to a ceramic cup with intricate blue patterns, morning sunlight passing through window blinds, soft shadows, shallow depth of field, ultra realistic



A top-down flat lay of five different pastries arranged in a perfect circle, each pastry with a distinct color glaze, a small handwritten label beside each one, minimal background, studio lighting, crisp details



A top-down flat lay of five different pastries arranged in a perfect circle, each pastry with a distinct color glaze, a small handwritten label beside each one, minimal background, studio lighting, crisp details



A futuristic subway station with a giant holographic timetable showing 'LINE 7 - NEXT TRAIN 02:15', reflective metal surfaces, commuters in motion blur, dramatic perspective, high contrast, photorealistic



A futuristic subway station with a giant holographic timetable showing 'LINE 7 - NEXT TRAIN 02:15', reflective metal surfaces, commuters in motion blur, dramatic perspective, high contrast, photorealistic



A cyclist in a bright yellow rain jacket riding through heavy rain at night, streetlights creating bokeh, water droplets frozen mid-air, dynamic motion, cinematic realism



A cyclist in a bright yellow rain jacket riding through heavy rain at night, streetlights creating bokeh, water droplets frozen mid-air, dynamic motion, cinematic realism



A product photo of a matte black perfume bottle labeled 'NOCTURNE' in silver foil, on a dark marble surface with soft reflections, controlled studio lighting, minimalist luxury aesthetic



A product photo of a matte black perfume bottle labeled 'NOCTURNE' in silver foil, on a dark marble surface with soft reflections, controlled studio lighting, minimalist luxury aesthetic

(a) **Control strip** along  $\hat{u}_C$ : mostly stylistic/noise drift, slower structured semantic change.

(b) **Horizontal-proxy strip** along  $\hat{u}_H$ : earlier, more structured, prompt-relevant semantic changes.

Figure 16. **Strip visualization along spherical geodesics.** Horizontal-proxy movement typically induces coherent semantic edits earlier than a random control direction, consistent with anisotropic sensitivity and low-rank local spectrum evidence.

Table 7. Prompt-level gains stratified by the geometry proxy  $s_{\min}$  (three quantile buckets).  $\Delta$  denotes CLIPScore(ours) – CLIPScore(baseline). Confidence intervals are bootstrap 95% over prompts within each bucket (2,000 resamples).

Bucket (by $s_{\min}$ )	# Prompts	$\mathbb{E}[\Delta]$	95% CI	Win rate
Low	67	0.424	[0.150, 0.699]	0.716
Mid	66	0.236	[-0.016, 0.484]	0.606
High	67	0.274	[-0.059, 0.573]	0.627

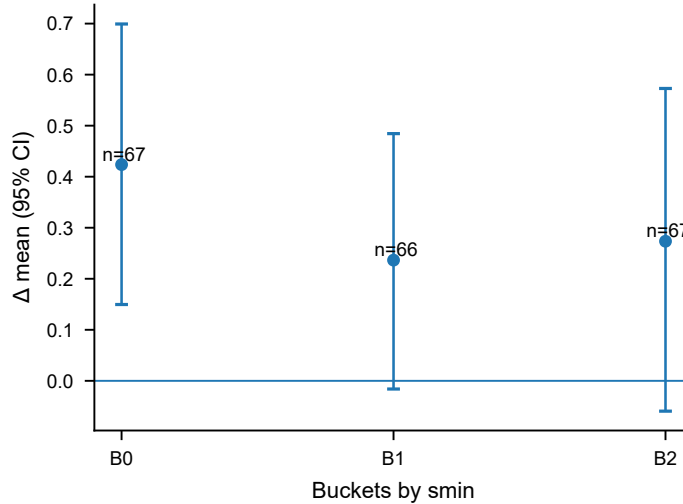


Figure 17. Bucketed analysis: mean  $\Delta$  with bootstrap 95% CI across three  $s_{\min}$  quantile buckets.

the baseline initial noise  $z_0$  using finite differences. For a set of random directions  $\{u_i\}_{i=1}^r$  and step size  $\varepsilon$ , we estimate

$$J_i \approx \frac{\pi(G(z_0 + \varepsilon u_i)) - \pi(G(z_0 - \varepsilon u_i))}{2\varepsilon}. \tag{51}$$

We compute the singular values of the stacked Jacobian and use the minimum singular value  $s_{\min}$  as a proxy for local non-degeneracy: larger  $s_{\min}$  suggests less collapse and a more submersion-like local behavior.

### E.9.3. OVERALL RESULTS

Across 200 prompts, our method yields a statistically significant improvement in CLIPScore:

- Mean improvement:  $\Delta = +0.312$ .
- Bootstrap 95% CI: [0.153, 0.466].
- Prompt-level win rate: 65.0%.
- Effect size: Cohen’s  $d = 0.266$ .

These results indicate a consistent, positive gain that is not driven by a small subset of prompts.

### E.9.4. REGIME ANALYSIS BY GEOMETRY PROXY ( $s_{\min}$ BUCKETS)

To study how improvements vary with local geometry, we bucket prompts into three quantiles by their prompt-level  $s_{\min}$  (low/mid/high). Table 7 reports the mean improvement and bootstrap confidence intervals per bucket.

We observe the strongest and most statistically reliable improvement in the low- $s_{\min}$  regime, consistent with the interpretation that our intervention is particularly helpful when  $\pi \circ G$  is locally closer to degeneracy. In the mid/high regimes, the mean improvement remains positive, but uncertainty increases.

## F. Diversity Analysis: Alignment Gains Without Diversity Sacrifice

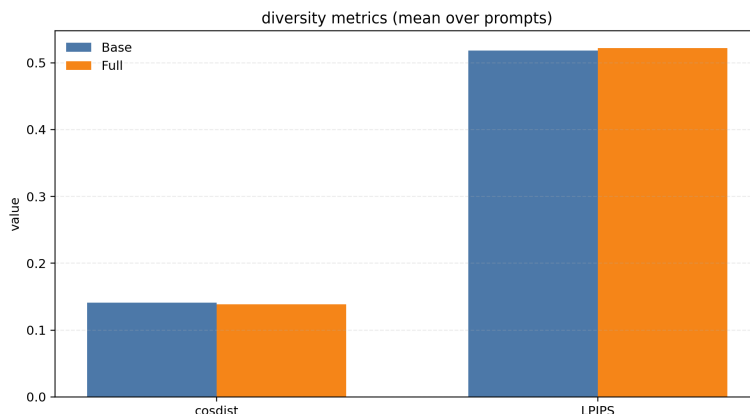


Figure 18. **Diversity metrics (mean over prompts) comparing Base vs. Full** improves alignment without reducing diversity: semantic diversity measured by embedding cosine distance remains essentially unchanged, while perceptual diversity measured by LPIPS is comparable or slightly higher.

A potential concern for inference-time alignment improvements is that they might arise from reduced output diversity (e.g., implicitly collapsing samples to fewer modes). To rule out this explanation, we compare seed-to-seed diversity between the **Base** sampler (standard generation) and the **Full** method (our inference-time procedure). As shown in Fig. 18, we observe no meaningful reduction in diversity under our method, suggesting that alignment gains are *not* obtained by sacrificing diversity.

### F.1. Evaluation Protocol

For each prompt, we generate  $n$  samples using  $n$  distinct random seeds under identical generation settings (model, resolution, guidance, sampler, and number of steps). For a diversity metric  $d(\cdot, \cdot)$ , we compute the average pairwise distance across the  $n$  samples:

$$D(\mathcal{S}) = \frac{2}{n(n-1)} \sum_{1 \leq i < j \leq n} d(x_i, x_j), \quad (52)$$

where  $\mathcal{S} = \{x_1, \dots, x_n\}$  denotes the set of samples for a fixed prompt. We then report the mean of  $D(\mathcal{S})$  over all prompts.

### F.2. Diversity Metrics

We use complementary metrics capturing semantic and perceptual diversity:

- **Embedding cosine distance (cosdist).** The average cosine distance in a semantic embedding space (e.g., CLIP), capturing *semantic diversity* such as changes in composition and scene semantics.
- **LPIPS.** A perceptual similarity metric; higher values indicate larger perceptual differences and thus greater *appearance-level diversity*.

### F.3. Results and Discussion

Figure 18 shows that diversity is preserved when switching from Base to Full:

- **Semantic diversity is unchanged.** The mean embedding cosine distance is nearly identical for Base and Full (cosdist\_base vs. cosdist\_full), indicating that our method does not compress variation in semantic space.
- **Perceptual diversity is maintained (or slightly increased).** LPIPS under Full is comparable to, and marginally higher than, Base (lpips\_full vs. lpips\_base), suggesting that outputs do not become more similar in appearance across seeds.

Overall, these results support that the alignment improvements of Full are not explained by reduced randomness or mode collapse, but rather by structured inference-time manipulation that improves alignment while preserving seed-to-seed diversity.

## G. Implementation Details

### G.1. Backbones.

We evaluate our method on: (i) text-to-image (T2I): SDXL (Podell et al., 2024a) and FLUX.1-Dev (Labs, 2024); (ii) text-to-video (T2V): Wan2.1 1.3B (Wang et al., 2025); (iii) text-to-3D: TRELIS Text XLarge (Xiang et al., 2025).

### G.2. Benchmarks.

For T2I we use Pick-a-Pic (Kirstain et al., 2023), DrawBench (Saharia et al., 2022), and HPD (Wu et al., 2023). For T2V we use VBench (Huang et al., 2024b). For text-to-3D we use Toy4K (Stojanov et al., 2021).

### G.3. Baselines.

Our baseline is **Standard** pipeline and a representative **noise refinement** baseline NpNet (Zhou et al., 2025) and Initno (Guo et al., 2024).

### G.4. Metrics.

For T2I, we report PickScore (Kirstain et al., 2023), AES (Huang et al., 2024a), ImageReward (Xu et al., 2023), and CLIPScore (Hessel et al., 2021). For T2V and text-to-3D, we use VQAScore (Lin et al., 2024; Bai et al., 2025) to quantify text alignment, and follow VBench (Huang et al., 2024b) / TRELIS (Xiang et al., 2025).

### G.5. Model Details

**FLUX.1 dev** (Labs, 2024) is an open-weight rectified-flow transformer for high-resolution text-to-image synthesis. The network stacks 19 MMDiT (Esser et al., 2024) blocks that jointly attend to 4096 T5-XXL (Raffel et al., 2020) text embeddings and a  $1024 \times 1024$  pixel latent grid. Training follows the straight-path rectified-flow objective: noise and data are connected by a linear interpolation, and the model learns the velocity field that transports pure noise to clean latents in a single continuous trajectory. Positional timestep encoding is removed; instead, a learnable “time” token is injected into every self-attention layer, allowing arbitrarily large sampling steps with minimal drift. FLUX-dev is distilled from the 23 B-parameter FLUX-pro teacher via logit-matching and adversarial ranking, yielding a 12 B-parameter student that runs in 16–20 steps on consumer GPUs while maintaining  $FID_{50K} \leq 17$  on COCO-30K (Pernias et al., 2024). The released checkpoint supports commercial use and can be fine-tuned with LoRA (Hu et al., 2022) in <10 GB VRAM.

**SDXL** (Podell et al., 2024a) is a cascaded latent diffusion model that generates  $1024 \times 1024$  images through a base+refiner ensemble. The base UNet (Ronneberger et al., 2015) grows to 3.5 B parameters ( $3 \times$  SD-1.5 (Rombach et al., 2022)) and is conditioned by a concatenated embedding from OpenCLIP (Ilharco et al., 2021) ViT-G/14 and CLIP ViT-L/14, giving dual-text awareness. Training uses a multi-aspect-ratio mixture (64% 1:1, 20% 2:3, 16% 3:2) with resolution-aware noise scheduling. After 1.3 M GPU-hours on 13 M high-resolution image-text pairs, the base model yields  $64 \times 64 \rightarrow 96 \times 96$  latents. An optional 2.3 B-parameter refiner UNet, trained on the same data but with high-frequency augmentation, upsamples the latent to  $96 \times 96 \rightarrow 128 \times 128$  and denoises again for 200 steps, reducing artifacts and improving text legibility. SDXL supports fine-grained style control via cross-attention prompt weighting and can be distilled to a 4-step adversarial model (SDXL-Turbo) without retraining the full pipeline.

**Wan 2.1 1.3B** (Wang et al., 2025) is a bilingual diffusion transformer optimized for Chinese-English text-to-image generation. The architecture replaces the UNet with a 24-layer unified transformer that operates on  $16 \times 16 \times 16$  spatiotemporal patches, enabling native 2K-resolution synthesis without multi-stage upsampling. Positional encoding is factorized into 3-D RoPE (Ma et al., 2025) for spatial axes and learned 1-D embeddings for the time axis, giving equivariance to arbitrary aspect ratios. Training adopts a three-stage curriculum: (i) 800 M Chinese-English alt-text pairs at  $512 \times 512$ , (ii) 200 M aesthetic-filtered 2K images with caption enrichment via an internal LLM, and (iii) 50 M human-feedback pairs ranked by a vision-language reward model. The final 1.3 B-parameter checkpoint achieves a 7.8 Chinese-FID on the WanBench-2K benchmark and supports fine-grained regional prompting through a masked cross-attention mechanism.

Table 8. Applicability and comparability of initial-noise optimization methods. “Training-free” indicates no additional optimization of model weights and no extra training dataset. “Arch.-agnostic” means not tied to UNet-only design choices and can be instantiated across different backbones/formulations given the standard inference interface.

Method	Training-free	Requires training	Custom dataset	Optimizes init noise	UNet diffusion	DiT Flow	Multimodal
ours	✓	×	×	✓	✓	✓	✓
InitNO	✓	×	×	✓	✓	×	×
NPNet	×	✓	✓	✓/-	✓/-	×	×

**Trellis text Xlarge** (Xiang et al., 2025) is a sparse-voxel rectified-flow transformer that maps natural-language prompts directly to 3-D assets without 2-D distillation. The network encodes text via frozen T5-XXL and injects the pooled embedding into a 24-block sparse 3-D UDiT (Zou et al., 2024); each block performs factorized self-attention on a  $128^3$  voxel grid that is dynamically pruned to  $\leq 20k$  surface cells, yielding  $\mathcal{O}(N)$  complexity. Training follows the straight-path rectified-flow objective on the 500 K-object TRELLIS-500K corpus (Objaverse (Deitke et al., 2023), ABO (Collins et al., 2022), HSSD (Khanna et al., 2024), Toys4K): noise and clean voxels are linearly interpolated, and the model regresses the voxel-wise velocity for 400k steps with batch 256 on 64 A100s. A multi-view render loss (LPIPS (Zhang et al., 2018) + MSE) on 8 random  $512^2$  views is back-propagated through a differentiable rasterizer to enforce visual fidelity. Inference runs in 12 s on an RTX-4090 and outputs three synchronized representations: (i)  $512^2$  triplane NeRF, (ii) 1 M-Gaussian 3-D splat, and (iii) watertight GLB mesh with 4 K UV atlas. The released 2 B-parameter checkpoint supports localized editing by voxel masking and can be distilled to 8-step turbo sampling with  $<3\%$  FID (Heusel et al., 2017) increase.

## G.6. Baseline Clarification and Applicability

### G.6.1. WHY THESE BASELINES?

**What we claim.** Our contribution targets *training-free* optimization of the *initial noise/latent* that is *architecture-agnostic* (i.e., it does not rely on a specific backbone such as UNet, nor a specific formulation beyond the standard model inference interface and sampler). To the best of our knowledge, we are the first such optimization scheme demonstrated across heterogeneous generative architectures and formulations.

**Why only two baselines in this niche?** The set of methods that explicitly focus on *initial-noise optimization* is relatively small, and most are not simultaneously (i) training-free, (ii) architecture-agnostic, and (iii) applicable beyond image-only pipelines. We therefore select two representative methods that are closest in spirit to our setting, while being explicit about their scope:

**InitNO** is a *training-free* initial-noise optimization approach, but it is *designed specifically for UNet-based diffusion pipelines* and is *image-only*. It serves as the closest training-free baseline when comparing within UNet diffusion settings.

**NPNet** requires *additional training* with a *separately customized dataset* and is *image-only*. Thus, NPNet is *not a strictly comparable training-free baseline*. We include it as a representative reference point for the line of work that improves generation via *learned, data-dependent optimization modules*, and we report/interpret it separately from training-free comparisons.

**Fairness and reporting.** In our main comparisons, we emphasize *training-free* methods under matched inference budgets (e.g., same sampler family, step count, resolution, and guidance configuration). Methods requiring additional training and dataset customization (e.g., NPNet) are treated as a different regime and are not used to substantiate training-free claims.

### G.6.2. SUMMARY TABLE OF APPLICABILITY

## G.7. Benchmarks

### G.7.1. T2I BENCHMARKS

**Pick-a-Pic** (Kirstain et al., 2023) benchmark is a large-scale, open dataset designed to evaluate text-to-image generation models based on real user preferences. Unlike traditional datasets that rely on crowdsourced annotations, Pick-a-Pic was created by logging user interactions with a web application, allowing users to generate images and specify their preferences.

This approach ensures that the dataset reflects authentic user interests and provides a more accurate assessment of model performance in real-world scenarios.

**DrawBench** (Saharia et al., 2022) benchmark is a comprehensive evaluation suite designed to assess the performance of text-to-image generation models in rendering complex spatial relationships and compositional scenes. Developed to challenge models’ understanding of explicit spatial directions, DrawBench provides a structured set of prompts that test the ability to position objects relative to each other based on textual descriptions.

**HPD** (Wu et al., 2023) benchmark is a large-scale, human-annotated dataset designed to evaluate the alignment of text-to-image generative models with human aesthetic preferences. It comprises 798,090 pairwise human preference choices across 433,760 images, generated from 107,000 diverse textual prompts. These images were produced by nine different generative models, ensuring a broad representation of model outputs.

### G.7.2. T2V BENCHMARK

**Vbench** (Huang et al., 2024b) is a comprehensive evaluation suite designed to assess the performance of video generative models across a multitude of dimensions. Recognizing the limitations of existing metrics that often fail to align with human perception, VBench introduces a hierarchical framework that dissects ”video generation quality” into 16 specific, disentangled dimensions. This approach facilitates fine-grained and objective evaluations, providing deeper insights into model performance.

### G.7.3. TEXT TO 3D BENCHMARK

**Toy4K** (Huang et al., 2024b) benchmark is a synthetic 3D object dataset designed to facilitate the evaluation of 3D object recognition and generation models. It comprises 4,000 3D object instances across 105 categories of developmentally plausible objects, making it a valuable resource for training and testing configurations in computer vision tasks.

## G.8. Metrics

### G.8.1. T2I METRICS

**Pickscore** (Kirstain et al., 2023) is a human preference prediction model designed to evaluate the alignment of images generated from textual prompts with human aesthetic judgments. Developed through a collaborative effort between Stability AI and Tel Aviv University, PickScore leverages a large-scale dataset of user preferences to train a scoring function that predicts which of two generated images a human would prefer. This metric addresses the limitations of traditional evaluation methods, such as Fréchet Inception Distance (FID), by providing a more direct alignment with human preferences.

**AES** (Huang et al., 2024a) is an automatic evaluation metric designed to assess the aesthetic quality of images generated by text-to-image models. It is particularly valuable in scenarios where human evaluation is impractical due to time constraints or scalability issues. AES aims to provide a reliable, reference-free measure of image aesthetics, aligning closely with human judgments.

**ImageReward** (Xu et al., 2023) is a human preference reward model designed to evaluate and improve text-to-image generation models by aligning their outputs with human aesthetic judgments. Developed by the THUDM group at Tsinghua University, ImageReward is trained on a large-scale dataset of 137,000 expert comparisons, making it the first general-purpose reward model for text-to-image synthesis.

**CLIPScore** (Hessel et al., 2021) is a reference-free evaluation tool designed to assess the alignment between generated captions and their corresponding images. Developed by Hessel et al., CLIPScore leverages the CLIP (Contrastive Language–Image Pretraining) model, a vision-language model pretrained on 400 million image-caption pairs, to compute the cosine similarity between the embeddings of an image and its caption. This approach enables the evaluation of image-caption alignment without the need for human-written reference captions.

### G.8.2. T2V METRICS

**VQAScore with Qwen-2.5-VL** (Lin et al., 2024; Bai et al., 2025) To assess the semantic alignment between video content and textual descriptions, we employ VQAScore. This facilitates the computation of similarity between video frames and their corresponding textual prompts.

**Frame Extraction:** We uniformly sample 200 frames from each video to ensure representative coverage. If a video contains fewer than 200 frames, we duplicate the last frame to meet the required number.

**Similarity Computation:** The VQAScore between each frame and the prompt is calculated. These individual similarities are then averaged to produce an overall similarity score for the video-text pair.

**Statistical Analysis:** We compute the mean and standard deviation of the similarity scores across all evaluated pairs to quantify the overall alignment and variability.

This methodology provides a quantitative measure of how well video content aligns with its textual description, facilitating the evaluation of generative models and aiding in the development of more coherent video-text representations.

**VBench (Huang et al., 2024b)** is a comprehensive and versatile benchmark suite designed to address the critical challenge of evaluating video generative models by decomposing “video generation quality” into 16 specific, hierarchical, and disentangled dimensions, including subject consistency, motion smoothness, spatial relationship, and aesthetic quality. It provides a standardized framework with tailored prompts and evaluation methods for each dimension, enabling fine-grained analysis of model strengths and weaknesses across diverse scenarios such as human actions, dynamic scenes, and object interactions. A key innovation of VBench is its emphasis on alignment with human perception, validated through extensive human preference annotations to ensure its automated evaluations reflect genuine perceptual quality. The framework is fully open-source, supporting reproducible evaluations for text-to-video and image-to-video generation, and includes a leaderboard to foster community-wide benchmarking and drive advancements in the field. By offering multi-perspective insights beyond monolithic scores, VBench serves as an essential tool for guiding the development of next-generation video generative models.

### G.8.3. TEXT TO 3D METRICS

**VQAScore with Qwen-2.5-VL (Lin et al., 2024; Bai et al., 2025)** computes the VQAScore of rendered images and input prompts. It is averaged over multiple views to ensure consistency. Higher scores indicate better alignment, reflecting the model’s ability to adhere to prompts.

**Fréchet Distance (Heusel et al., 2017) (FD) with Inception-v3 (Szegedy et al., 2016)** measures the similarity between feature distributions of generated and real images using Inception-v3. Lower FD values indicate that generated assets are closer to the real data distribution in feature space, reflecting higher visual quality.

**Kernel Distance (Phillips & Venkatasubramanian, 2011) (KD) with Inception-v3 (Szegedy et al., 2016)** uses kernel methods (e.g., MMD) to compare feature distributions from Inception-v3. It assesses distribution alignment, with lower scores suggesting that generated outputs are realistic and diverse.

**Fréchet Distance (Heusel et al., 2017) (FD) with DINOv2 (Oquab et al., 2024)** This variant employs DINOv2 features, which capture rich semantic information. Lower FD values indicate better semantic consistency with real-world objects, leveraging the model’s strong representation power.

**Kernel Distance (Phillips & Venkatasubramanian, 2011) (KD) with DINOv2 (Oquab et al., 2024)** By applying kernel distance to DINOv2 features, this metric emphasizes structural and semantic similarities. Lower scores denote that generated assets align well with expected visual characteristics.

## G.9. Model Setting

For the standard method, we adopted the hyperparameters presented in Table 9, we increased the number of inference steps for the standard pipeline so that its total inference time matches ours, which incurs additional computational cost due to our design.

### G.9.1. HYPERPARAMETER

This section analyzes key hyperparameters in our method, including the TPW probe setting  $(K, \{t_k\})$  and the injection strength  $\delta$ , and justifies the default configuration used in the main experiments.

**TPW Probe Steps  $K$  and Timestep Choice  $\{t_k\}$**  In the TPW (Temporal Probe Weighting) stage, a natural design is to probe multiple key timesteps  $\{t_k\}_{k=1}^K$  and aggregate their residual signals with weights. While multi-timestep probing

Table 9. Inference Settings for SDXL, FLUX.1 Dev, Wan2.1 T2V 1.3B, and TRELIS Text XLarge

Parameter	SDXL	FLUX.1 Dev
Number of Inference Steps	51 (Before: 50)	29 (Before: 28)
Guidance Scale	7.5	3.5
Eta (for DDIM Scheduler)	0.0	-
Output Image Size	1024 × 1024	1024 × 1024
True CFG Scale	-	1
Parameter	Wan2.1 T2V 1.3B	TRELIS Text XLarge
Resolution	832×480 (480p)	-
Sample Guide Scale	6	-
Sample Shift	10	-
Sparse Sampler Steps	-	26 (Before: 25)
Sparse Sampler CFG Strength	-	7.5
SLAT Sampler Steps	-	26 (Before: 25)
SLAT Sampler CFG Strength	-	7.5

can improve robustness in principle, in our empirical study we found that **using only  $K = 1$  already yields a strong and reliable semantic direction** for subsequent injection and retraction, while substantially reducing computation.

Therefore, to maximize efficiency, all main experiments use  $K = 1$  and extract semantics at a fixed probing timestep  $t = 990$ . This single-step probe provides stable semantic signals across both simple prompts (clear single subject) and complex prompts (rich constraints and compositions), without the additional cost of multiple model evaluations.

**Injection Strength  $\delta$**  The injection strength  $\delta$  controls the magnitude of horizontal semantic injection before retraction, and thus directly trades off semantic enhancement and visual quality. We sweep  $\delta$  over a wide range and evaluate performance on both simple prompts and complex prompts.

Overall, we observe that small  $\delta$  leads to limited semantic gain, while overly large  $\delta$  may introduce artifacts and degrade aesthetic quality. Across our tests,  $\delta = 6$  **consistently provides strong improvements for both simple and complex prompts while maintaining aesthetic metrics without degradation**. We therefore adopt  $\delta = 6$  as the default setting.

### H. Visualization Method in Figure 1

The overall visualization method in Figure 1 is summarized in Fig. 19.

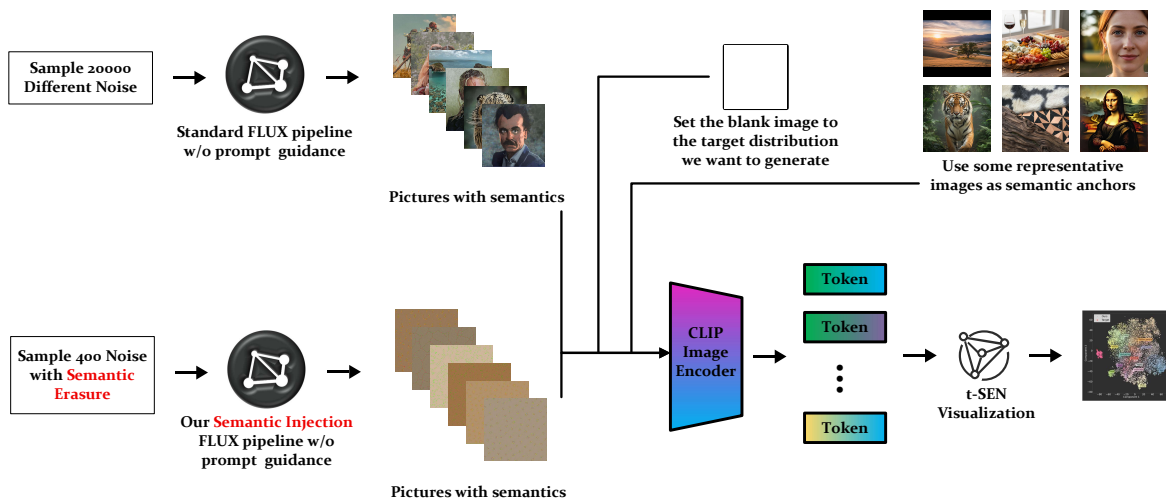


Figure 19. Visualization Method in Fig. 1.

## I. Details about User Study

### I.1. Surveyed Population Demographics

To evaluate the performance of our model across diverse demographic groups, we conducted surveys involving a total of 488 participants across different studies. The combined demographic distribution is as follows:

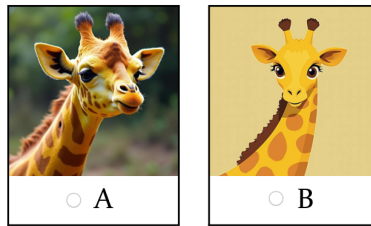
Table 10. Combined Gender Distribution Across Age Groups with Percentages

Age Group	Male	Female	Percentage
Under 18	32	24	11.48%
18–25	64	42	21.72%
26–30	62	46	22.13%
31–40	32	22	11.06%
41–50	30	24	11.06%
51–60	38	32	14.34%
Over 60	26	12	7.78%
<b>Total</b>	<b>286</b>	<b>202</b>	<b>100.00%</b>

### I.2. Survey Methodology

As shown in Fig. 20, participants were presented with pairs of images, videos or 3D models and corresponding descriptions. They were tasked with selecting the image, video or 3D model that best matched the provided description. The descriptions used were designed to test various aspects of alignment, including object presence, color accuracy, and spatial relationships.

1. Which of the following images better matches the description: 'a yellow giraffe'?



2. Which of the following images better matches the description: 'White lines depict topography on a black background.'?

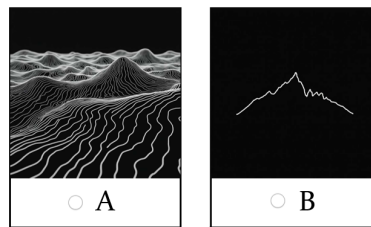


Figure 20. Schematic Diagram of Questionnaire Design

## I.3. Results

### I.3.1. T2I

Our method was preferred over the standard in the majority of cases, with preferences ranging from 54.29% to 74.29%. Notably, captions describing specific objects or unique combinations, such as “Cat wearing Pikachu hat” and “Birthday card with text,” showed higher preference percentages, indicating our model’s strength in handling detailed and complex prompts.

However, captions involving abstract or less common concepts, like “SDO sun image with low activity,” received lower preference scores. This suggests that while our method performs well with standard and detailed prompts, there is room for

Table 11. User Study Across Different Generation Modalities

Category	Ours (%)	Standard (%)
<b>T2I</b> Basic Objects & Colors	92.5	7.5
<b>T2I</b> Counterfactual Concepts	85.0	15.0
<b>T2I</b> Spatial & Textual Relations	55.0	45.0
<b>T2I</b> Stylistic & Artistic Rendering	81.4	18.6
<b>T2I</b> Complex & Specific Concepts	72.9	27.1
<b>T2V</b> Dynamic Scenes	66.4	33.6
<b>T2V</b> Static Scenes	53.8	46.2
<b>Text to 3D</b> Detailed Objects	58.6	41.4
<b>Text to 3D</b> Specialized Objects	51.9	48.1
<b>Overall (T2I)</b>	74.1	25.9
<b>Overall (T2V)</b>	64.5	35.5
<b>Overall (Text to 3D)</b>	55.3	44.7

improvement in handling more specialized or scientific descriptions.

The user study demonstrates that our method generally aligns better with textual prompts compared to standard, particularly in scenarios requiring detailed and specific image generation. These findings highlight the effectiveness of our approach in enhancing text-image alignment and provide a foundation for further refinement in handling a broader range of descriptive prompts.

### I.3.2. T2V

Our method was preferred over the standard model in the majority of cases, with preferences ranging from 53.85% to 66.35%. Notably, descriptions involving dynamic scenes, such as “A person is skydiving” and “A boat accelerating to gain speed,” showed higher preference percentages, indicating our model’s strength in capturing motion and activity.

However, descriptions involving static or less common scenes, like “A tranquil tableau of an apple,” received relatively lower preference scores. This suggests that while our method performs well with dynamic and action-oriented prompts, there is room for improvement in handling more static or less common scenarios.

The user study demonstrates that our method generally aligns better with textual prompts compared to standard models, particularly in scenarios requiring the depiction of motion and activity. These findings highlight the effectiveness of our approach in enhancing text-video alignment and provide a foundation for further refinement in handling a broader range of descriptive prompts.

### I.3.3. TEXT TO 3D

Our method was preferred over the standard model in most cases, with preferences ranging from 51.92% to 58.65%. Notably, descriptions of complex objects with detailed features, such as “A white cylindrical cup with blue stripes” and “A blue semi-truck with specific features,” showed higher preference percentages, indicating our model’s strength in handling detailed and intricate prompts.

However, descriptions involving highly specialized or less common objects, like “A vintage telephone with a rotary dial,” received relatively lower preference scores. This suggests that while our method performs well with standard and detailed prompts, there is room for improvement in handling more specialized or less common object descriptions.

The user study demonstrates that our method generally aligns better with textual prompts compared to standard models, particularly in scenarios requiring detailed and intricate object generation. These findings highlight the effectiveness of our approach in enhancing text-3D alignment and provide a foundation for further refinement in handling a broader range of descriptive prompts.

## J. Computational Overhead and Budget-Matched Comparison

Our method is *training-free* and introduces only a lightweight seed pre-processing stage before the standard sampler. Since diffusion/flow inference is overwhelmingly dominated by backbone forward evaluations, we quantify cost primarily by the

Table 12. Inference-time overhead comparison measured by backbone forward calls.  $S$  is the sampler step count,  $m$  is the number of backbone evaluations per step (e.g.,  $m=2$  under CFG), and  $K$  is the number of probing timesteps in TPW.

Method	Backbone calls	Extra training/params	Notes
Standard	$mS$	None	Official pipeline
Ours (NLN+TPW+Retract)	$m(S+K)$	None	$K=1$ in all main results

number of denoiser/velocity-network forward calls, while treating random sampling and vector arithmetic as negligible overhead.

**Forward-pass accounting.** Let  $S$  denote the number of sampling steps used by the standard pipeline, and let  $m$  be the number of backbone evaluations per step ( $m = 2$  for classifier-free guidance with conditional/unconditional calls;  $m = 1$  otherwise). The baseline inference cost is therefore

$$\text{Cost}_{\text{base}} \approx m S \cdot C_{\text{net}}, \tag{53}$$

where  $C_{\text{net}}$  is the average cost of a single network forward.

Our pipeline adds two extra components: (i) **NLN** draws  $n$  i.i.d. Gaussians and forms  $\bar{z}_T = \frac{1}{\sqrt{n}} \sum_i z^{(i)}$ , which is  $\mathcal{O}(nd)$  elementwise work and does not invoke the backbone; (ii) **TPW** probes the backbone at  $K$  selected timesteps to form the aggregated horizontal direction (Algorithm 1), incurring  $mK$  additional forward calls. Hence,

$$\text{Cost}_{\text{ours}} \approx m(S+K) \cdot C_{\text{net}} + \underbrace{\mathcal{O}(nd)}_{\text{NLN (no backbone)}}. \tag{54}$$

The relative overhead (ignoring the negligible NLN arithmetic) is

$$\frac{\text{Cost}_{\text{ours}}}{\text{Cost}_{\text{base}}} \approx 1 + \frac{K}{S}. \tag{55}$$

**Practical setting and fair comparison.** In all experiments we use a *single* probing timestep ( $K=1$ ) to keep the overhead bounded by roughly one sampling step (i.e.,  $\approx 1/S$  relative cost). To make comparisons compute-fair, we additionally report the standard pipeline with slightly increased steps so that its wall-clock time is comparable to ours (see Table 9). This eliminates the possibility that improvements stem from a larger inference budget rather than the proposed seed shaping.

**Memory and implementation overhead.** Our method stores only a constant number of latent-sized tensors (the aggregated prediction and a few temporaries), i.e.,  $\mathcal{O}(d)$  memory. No gradients, Jacobians, or auxiliary networks are required, and the method is a drop-in wrapper around existing samplers.

### K. Additional Ablation Study Results

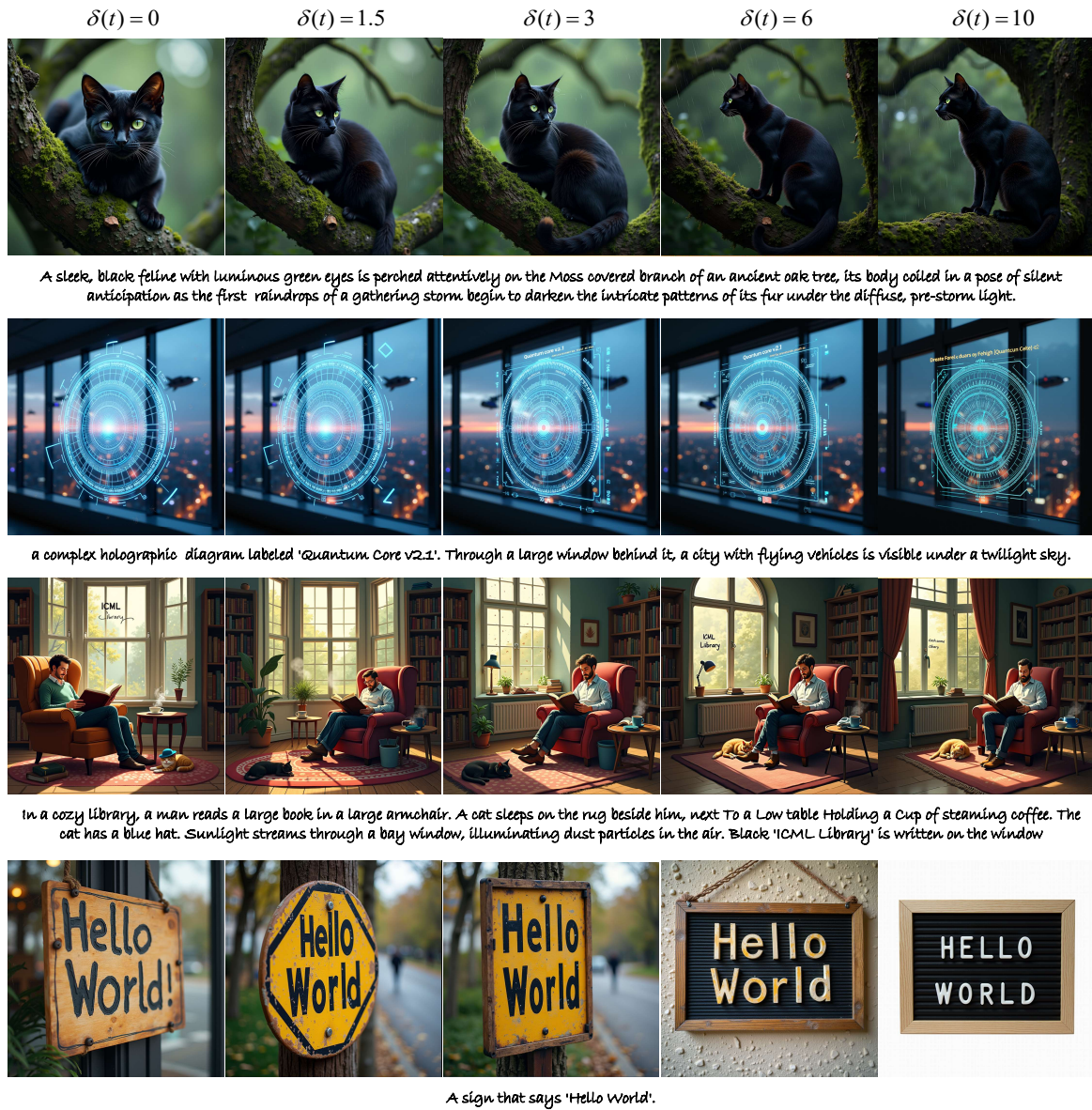


Figure 21. The impact of the value of  $\delta(t)$  on model generation (FLUX).

## L. Additional Main Experiment Results

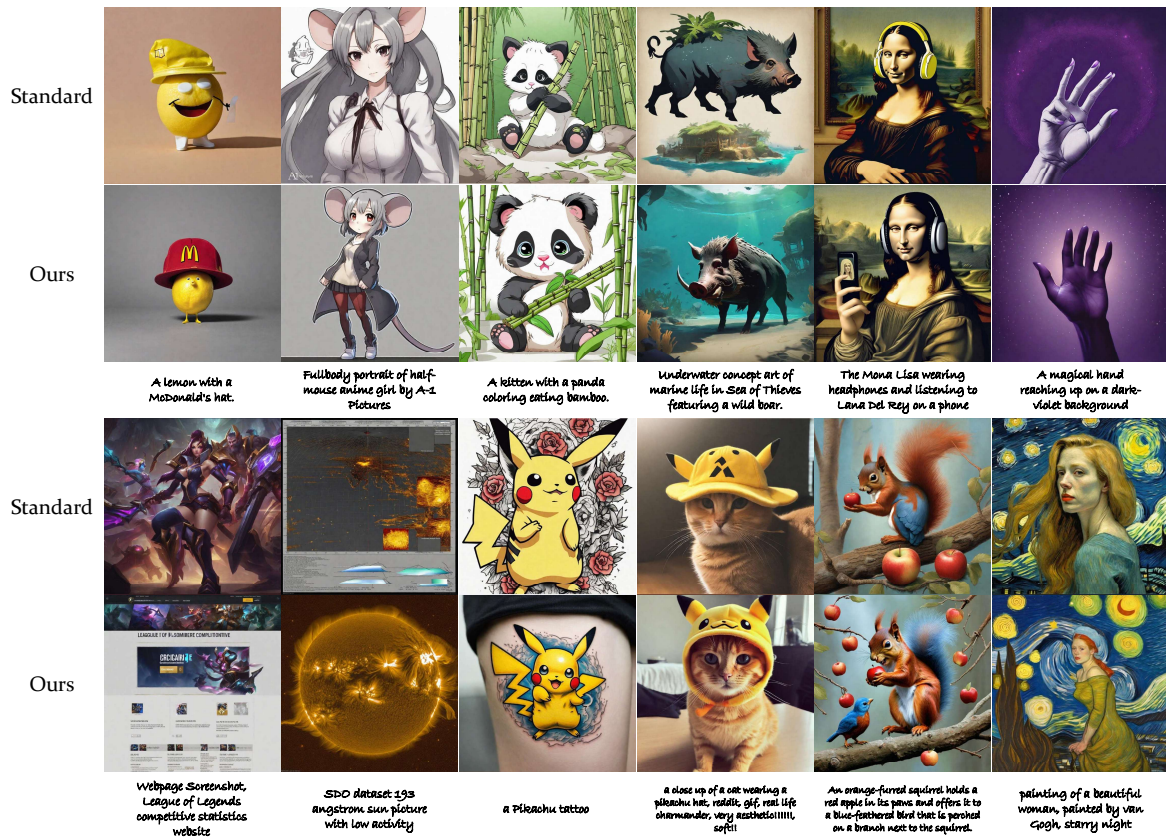


Figure 22. More Results of SDXL

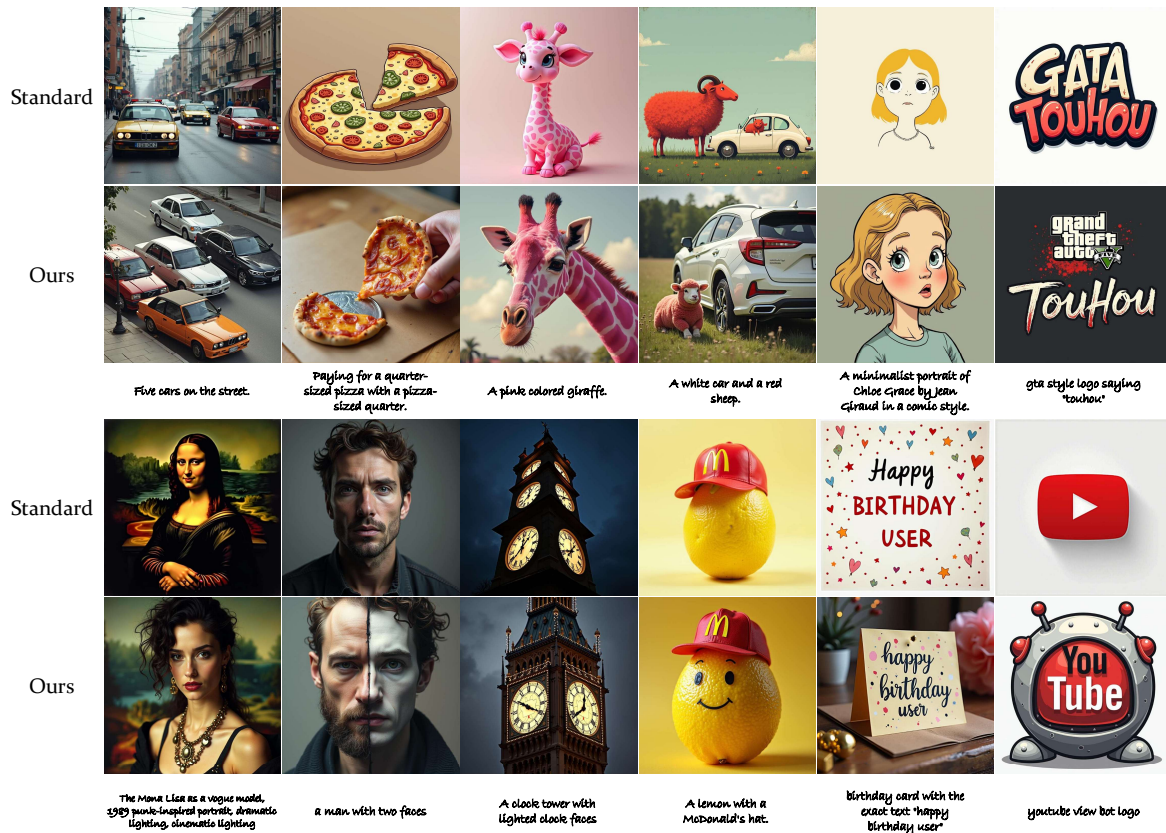


Figure 23. More Results of FLUX

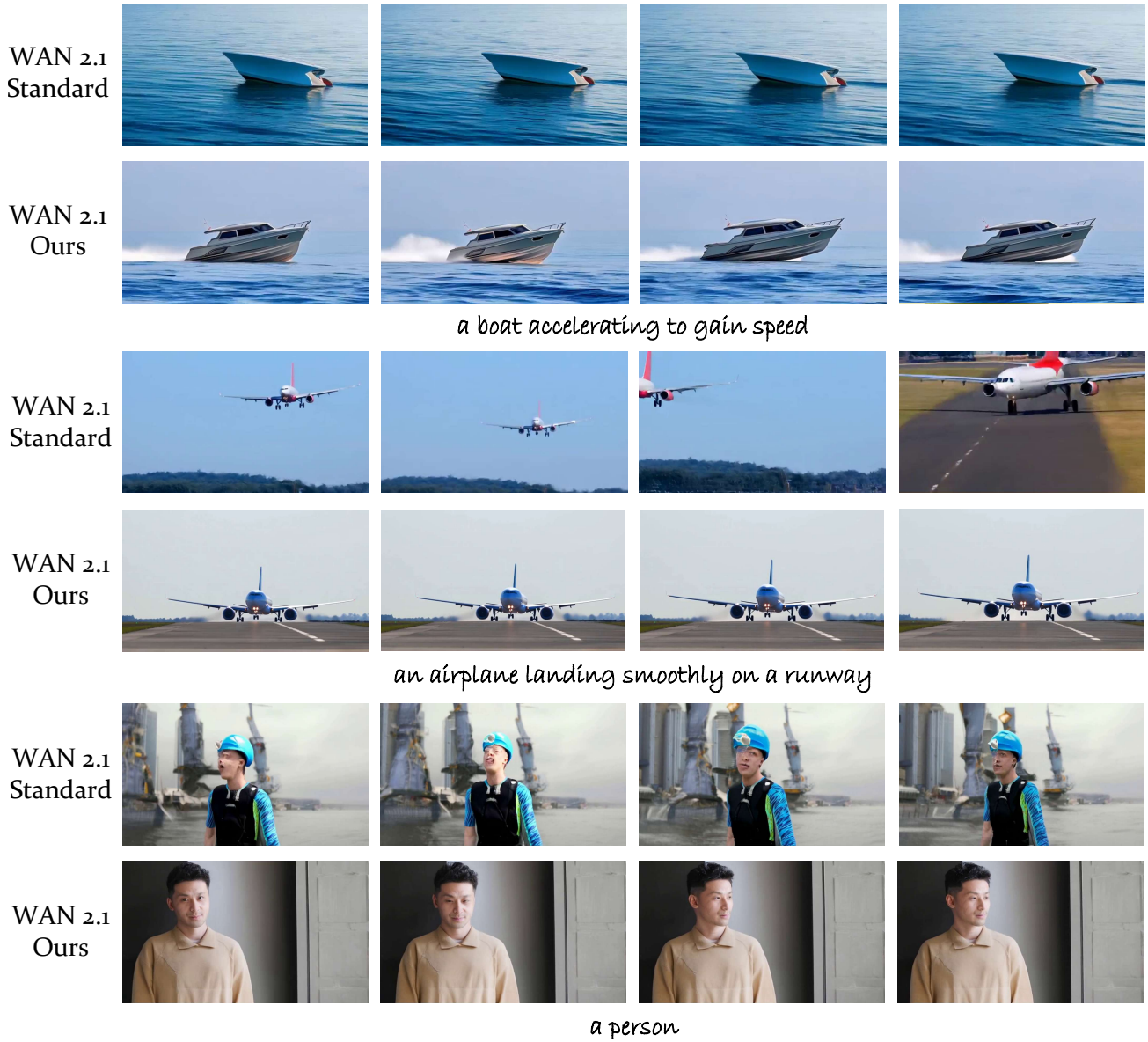


Figure 24. More Results of WAN 2.1 1.3B

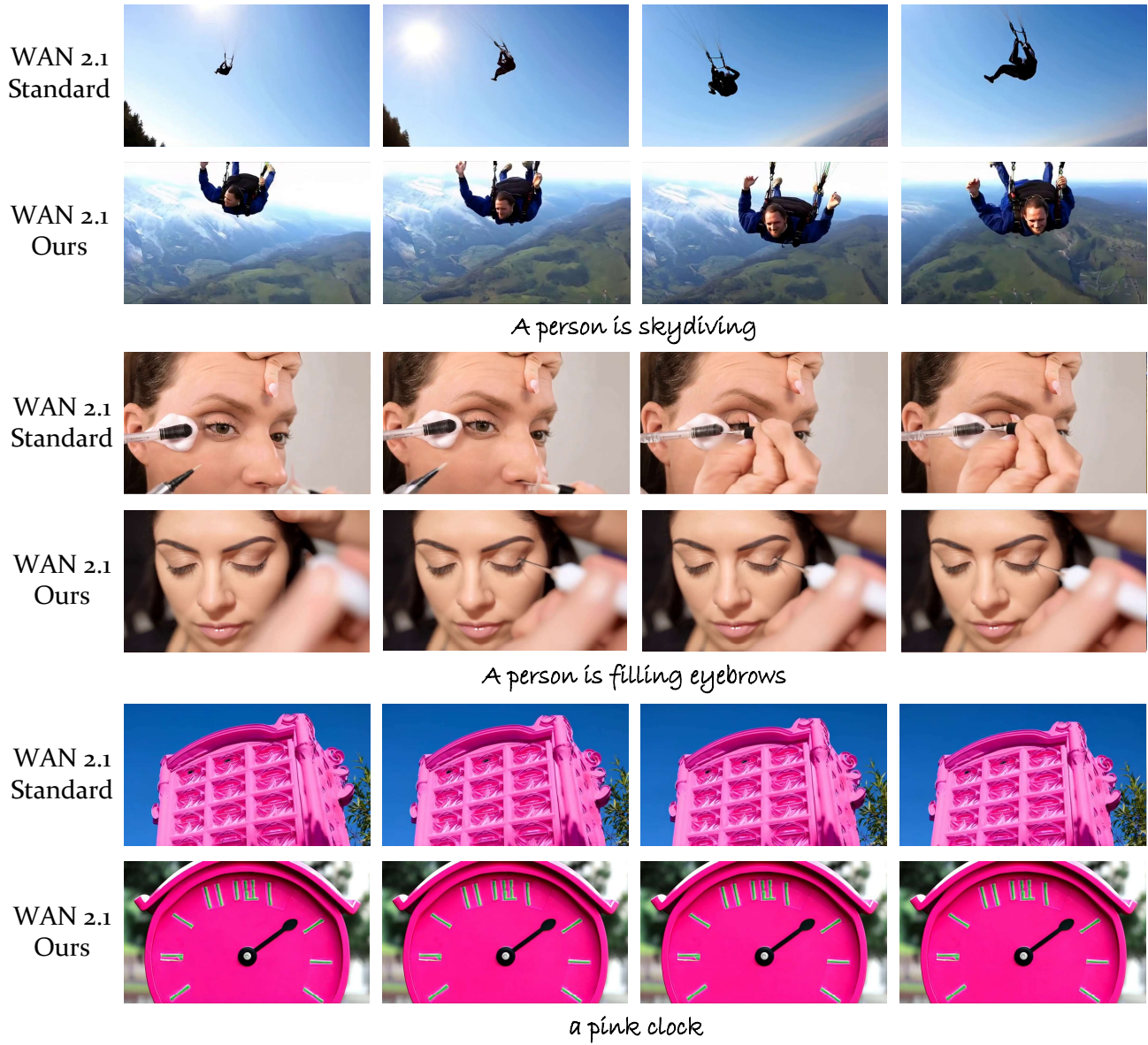


Figure 25. More Results of WAN 2.1 1.3B

TRELLIS  
Standard

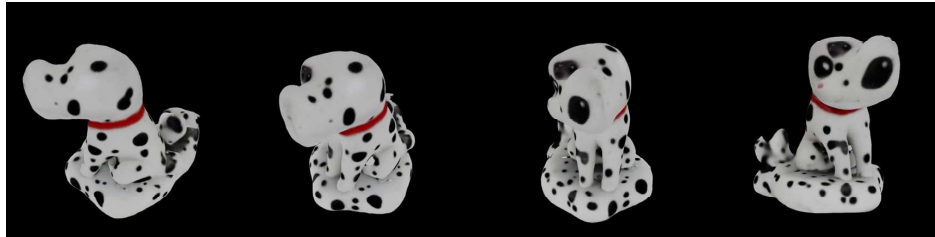


TRELLIS  
Ours

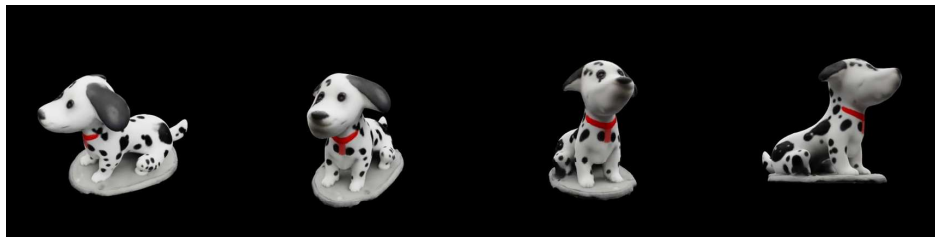


A 3D model of a violin with an amber body and darker front, white neck and scroll, black fingerboard, pegs, and tailpiece, metallic silver strings, a light beige bridge, and black f-holes.

TRELLIS  
Standard

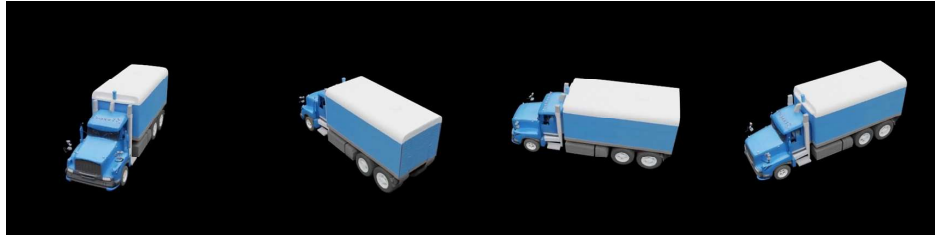


TRELLIS  
Ours

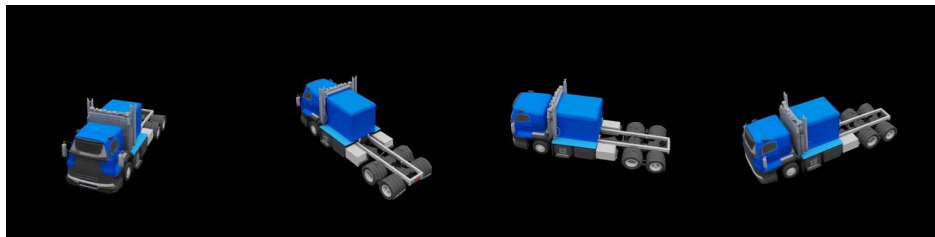


A small figurine of a seated Dalmatian dog with a predominantly white body, black spots, detailed black facial features, large floppy black ears, a black spot above the left eye, a black tail laid flat, and a red collar.

TRELLIS  
Standard



TRELLIS  
Ours



A blue semi-truck with a rectangular cabin, round edges, black grill, single front and dual rear wheels, grey chassis, white fuel tanks, black mudflaps, tall exhaust pipe on the driver's side, and roof lights and horns. \*Blue semi-truck, rectangular cabin, round edges, black grill, dual rear wheels, grey chassis, white fuel tanks.

Figure 26. More Results of TRELLIS Text Xlarge

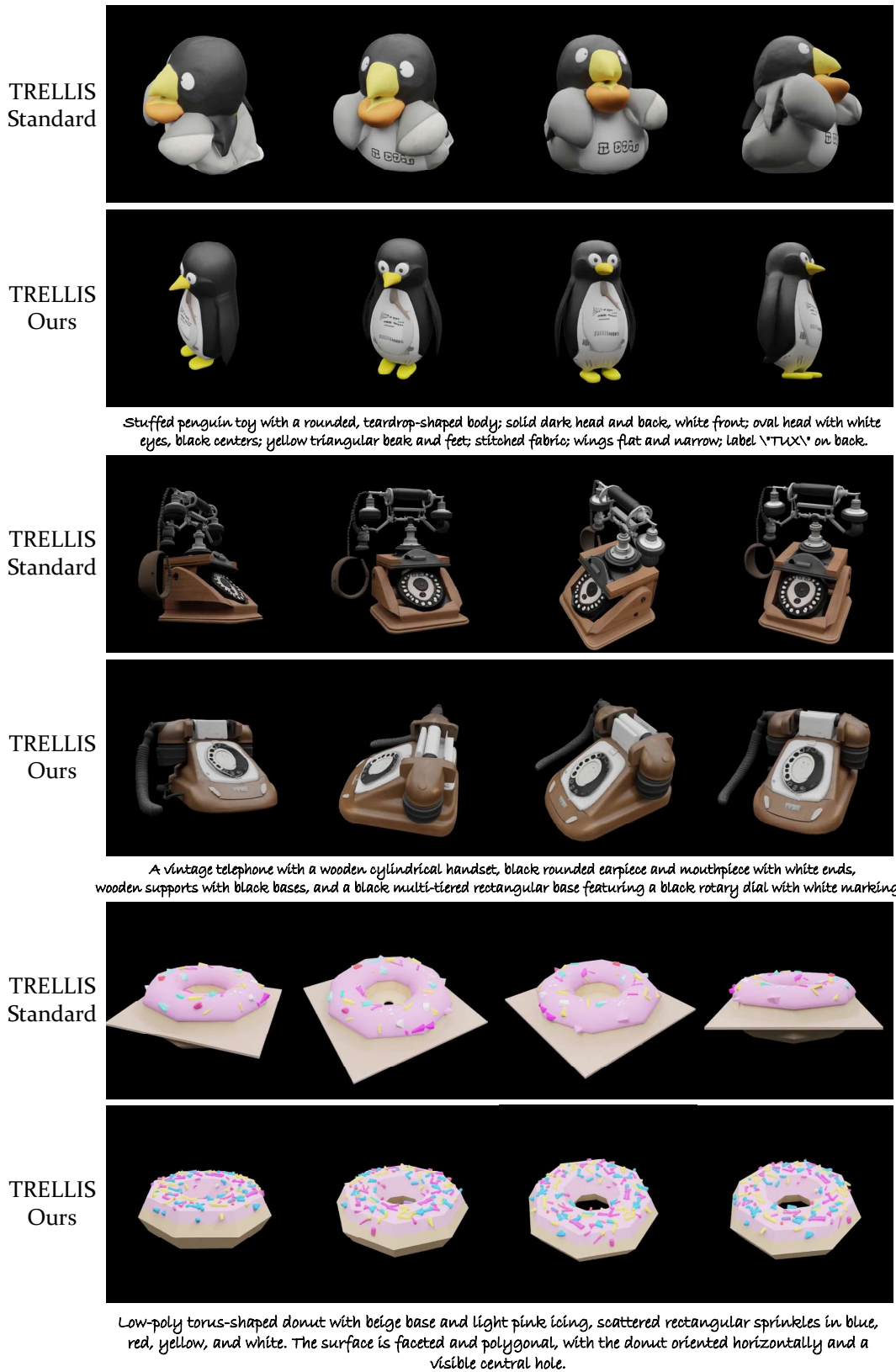


Figure 27. More Results of TRELLIS Text Xlarge